Politecnico di Milano

SCHOOL OF INDUSTRIAL AND INFORMATION ENGINEERING

Master of Science – Energy Engineering

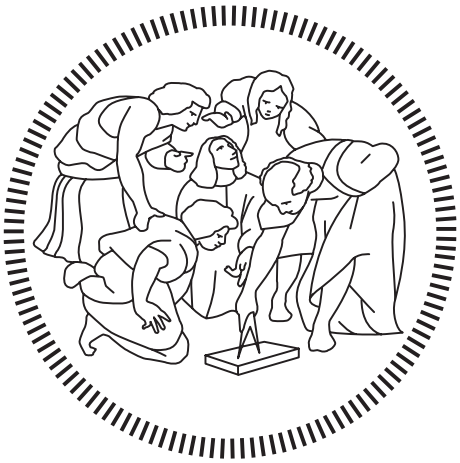

# Economic optimization of integrated $H_2$ and CCS chains for $CO_2$ emission mitigation: the case study of the Puglia region

Supervisor

**Dr. Paolo COLBERTALDO**

Co-Supervisors

**Dr. Federico d'AMORE**

**Prof. Matteo Carmelo ROMANO**

Candidate

**Simone RIZZI – 941237**

**Academic Year 2021 – 2022**

POLITECNICO
MILANO 1863

SCUOLA DI INGEGNERIA INDUSTRIALE
E DELL'INFORMAZIONE

EXECUTIVE SUMMARY OF THE THESIS

# Economic optimisation of integrated $H_2$ and CCS chains for $CO_2$ emission mitigation: the case study of the Puglia region

TESI MAGISTRALE IN ENERGY ENGINEERING – INGEGNERIA ENERGETICA

**AUTHOR: SIMONE RIZZI**

**ADVISOR: PAOLO COLBERTALDO**

**ACADEMIC YEAR: 2021-2022**

## 1. Introduction

During the last decades, the energy strategies introduced for industrial and electricity generation sectors have been strongly influenced by the issue of global warming, caused by the emission to the atmosphere of substantial amounts of anthropogenic greenhouse gases (i.e., GHGs), among which carbon dioxide ($CO_2$). Several technologies have been studied for mitigating $CO_2$ emissions from stationary sources, including carbon capture, transportation and storage (CCS), hydrogen and renewable energy sources (RES), differing among each other for what concerns costs, performances and application limits. This thesis discusses the design and economic optimisation of an infrastructure for the simultaneous application of such technologies, aiming at reducing the $CO_2$ emissions from the industrial and the energy generation sources in a region. Moreover, the study encompasses the hourly load of each plant, in order to satisfy the monthly demand constraints and the energy balance at each timestep, simulating the operation of the infrastructure along one year. The mathematical framework is tested in an exemplificative case study, focused on a geographical area corresponding to the Italian region of Puglia, chosen due to the high availability of wind and solar energy and for the presence of large-scale $CO_2$ emitting industries. A multi-period spatially explicit mixed integer linear programming (i.e., MILP) problem is solved in order to minimise the total cost of the infrastructure and, at the same time, limit the total $CO_2$ emitted to the atmosphere.

## 2. Literature review

A hydrogen supply chain (HSC) encompasses the production, distribution, storage and final use of hydrogen. This energy vector can be generated from a multitude of sources, of which this work focuses on blue and green hydrogen production, exploiting natural gas (with CCS) and renewable electricity as energy source, being characterised by a high $CO_2$ emission mitigation effect and energy sources availability. After the production, the designed infrastructure delivers hydrogen to final users via pipeline. For what concerns final uses, for this work the alternatives more compatible with the pre-existent systems are selected, therefore a portion of the natural gas demand is replaced with

hydrogen for natural gas combined cycles (NGCCs) and residential utilities. To easily adapt the natural gas-based systems to partially operate with $H_2$, a blending limit of 15%vol is introduced for the natural gas distribution system, due to the low stability of hydrogen [1]. The last components of the HSC are tanks, considered as the only storage option. Since the majority of $H_2$ is produced by SMRs, being the cheapest option [1], there is no need for storing high quantities in geological sites, that also require additional geological assessments for verifying the suitability for this application.
CCS network includes three phases: capture, transportation and storage. In this thesis, $CO_2$ is captured from industrial sources and thermoelectric power plants, with costs and performances depending on the type and size of the emission source. The captured $CO_2$ is then transported via pipeline or ship towards the $CO_2$ geological storage sites, being saline aquifers formations distributed along the Italian peninsula and exhaust oil reservoirs in the North Sea, whose huge storage potential [2] prevents the storage capacity from limiting the penetration of the CCS network in the infrastructure.

## 3. Grid nodes definition

The infrastructure is modelled with a graph, composed of nodes and lines. Each node is characterised by mass and energy inputs and outputs, contributing to the nodal and global mass and energy balances. Therefore, for developing the infrastructure it is crucial to define such nodes in terms of position, inputs and outputs.

### 3.1. Industries and power plants

The intense and heterogeneous industrial activity characterising Puglia region includes 10 large-sized industrial plants, each one emitting more than 300 $kt_{CO2}/y$ [3], being two cement industries (CE01, CE03), one fuel refinery (FR01), one steel industry (ST01), one chemical industry (CH01) and 5 thermoelectric power plants (PP01-PP05). To these emission sources is added another large-size cement industry (CE02), sited in the adjacent province of Matera, due to the proximity to the regional border. Such plants are modelled in the infrastructure as geographically-explicit nodes (Figure 1) [3].

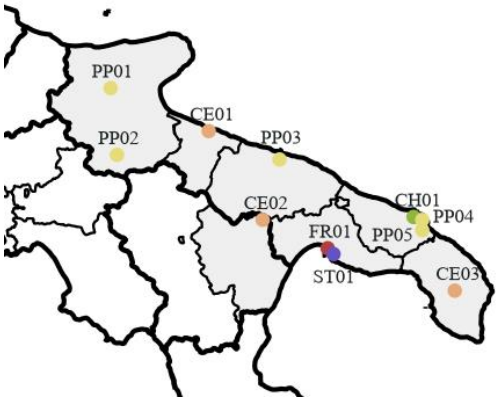


Figure 1. Geographical location of the industries and thermoelectric power plants sited in the studied region

Industrial nodes receive in input fuels and raw materials from external sources, while electricity is provided by the infrastructure. The output produced consists in $CO_2$, optionally captured and stored, and the final product. For what concerns the plant production, the infrastructure selects the hourly load without modifying the monthly demand of the site. For what concerns NGCC nodes, the cycles receive in input natural gas from external sources, and possibly hydrogen produced by the infrastructure. The main outputs determined by the production process consists in $CO_2$, that can be captured with the installation of a CCS plant, electricity, generated accordingly to the demand profile of the studied region, and hydrogen. In NGCC nodes, $H_2$ can be produced by integrating the combined cycle with a SMR, feeding the electricity generation process occurring in the node or the HSC designed by the infrastructure. Another approach is instead applied for the coal-power plant, whose hourly load is optimised by the model, with the only production limits being the nominal capacity and the electricity demand of the region.

### 3.2. $CO_2$ storage sites and port

In order to maximise the $CO_2$ avoided in such plants, $CO_2$ storage sites are added to the nodes set according to the work conducted by Donda et al. [4], providing the location and capacity of 14 potential storage sites (CS02-CS15), distributed along the Italian peninsula. In addition, the infrastructure includes another node corresponding to the North Sea (CS01), with an almost infinite storage potential. The more accessible sites in terms of geographical position

for the studied region are the ones sited in southern Italy, with an overall storage potential higher than 645 $Mt_{CO2}$, enough for potentially storing the whole $CO_2$ emitted in the region (more than 25 $Mt_{CO2}$/y) for 25 years.

## 3.3. Virtual nodes

Along with the nodes previously described, defined by the exact geographical location, the infrastructure includes virtual nodes, among which consumption (CN01-CN07), production (PN01-PN07), import (IN01) and export (EN01) nodes.

Consumption nodes account for the electricity and natural gas demand not included in the thermoelectric power plants and industrial nodes sets. Their geographical location corresponds to each of the seven provinces included in the studied region. The infrastructure must satisfy the electricity and natural gas demand of such nodes at each hour of the year. Although the electricity consumption is provided as a parameter, the natural gas demand can be partially substituted with hydrogen, constituting a degree of freedom for the optimisation algorithm, limited by the blending limit and the hourly thermal energy demand of each node. The export node is associated to an hourly electricity demand, representative of the electricity exported towards the other Italian region.

Production nodes account for the electricity generation from RES in each province, in detail wind power and solar PV. The geographical location of such nodes coincides with the consumption nodes, being both the node typologies representative of the same areas. The optimisation algorithm cannot control the hourly production from these sources, being not-dispatchable, although a degree of freedom is represented by the nominal capacity installed, that can be optionally incremented. Moreover, such nodes are suitable for green hydrogen production, thanks to the possibility to install an electrolyser exploiting renewable electricity as energy source.

The import node accounts, instead, for the electricity imported from other Italian regions, representing a dispatchable energy source not related to a $CO_2$ emission. In order to give priority to the energy generators located in the studied region, imported electricity is associated to a very high cost (1'000 €/$MWh_{EL}$).

# 4. Mathematical model

The installation and operation of the different components of the infrastructure is determined by solving a MILP problem, in which an objective function, being the total cost, is minimised alongside a set of constraints, accounting for physical limits and design choices.

## 4.1. Objective function

The total cost function is determined from the contributes of the CCS network, the HSC ($TC^{HSC}$), the additional RES capacity installed in the area, the cost related to the electricity imported from the other Italian regions and the fuel consumed by the infrastructure.

$$TC = TC^{CCS} + TC^{HSC} + TC^{RES} + TC^{ELC,IMP} + TC^{FUEL} \quad (4.1)$$

The total capture cost is defined as a linear function in the continuous variable $M_{t,n}^{CO2,CAPT}$ [$t_{CO2}$/h], expressing the $CO_2$ captured in node n at each time step t. This variable is associated to a cost of $CO_2$ avoided, composed of a fixed ($CCA_n^{FIX}$) and a variable ($CCA_n^{VAR}$) components. The parameter $CCA_n^{FIX}$ is subjected to scale economies, therefore its cost increases with the size of plant n.

$$TCC^{CCS} = \sum_n ((CCA_n^{FIX} + CCA_n^{VAR}) \cdot \cdot \sum_t M_{t,n}^{CO2,CAPT}) \quad (4.2)$$

After the capture section, $CO_2$ can be transported via pipeline, with a total cost defined with a unitary transportation cost ($UTC_{q,n,n'}^{PIPE}$, [€/km/$t_{CO2}$]) specific to the annual $CO_2$ exchanged between two nodes n and n' and to the distance covered by the pipe. Although the pipeline cost is subjected to scale economies, a unique value of $UTC_{q,n,n'}^{PIPE}$ is considered in this study, in order to reduce the computational burden of the problem. The unitary cost is increased by a parameter $\Omega_{n,n'}^{OFFSHORE}$, for the case of offshore transport.

$$\mathrm{TTC}^{\mathrm{CCS,PIPE}} = \sum_{n,n'} [\mathrm{LD}_{n,n'} \cdot \Omega_{n,n'}^{\mathrm{OFFSHORE}} \cdot \cdot \sum_q \left(\mathrm{UTC}_{q,n,n'}^{\mathrm{PIPE}} \cdot \mathrm{M}_{q,n,n'}^{\mathrm{CO2,PIPE,NOM}}\right)] \quad (4.3)$$

Analogously to the CCS network, the HSC cost structure is divided into three contributions, accounting for the $H_2$ production, transportation and storage.

$$TC^{HSC} = TPC^{HSC} + TTC^{HSC} + TSC^{HSC} \quad (4.4)$$

The total hydrogen production cost provides a linear dependence on the variable $M_n^{H2,PRD,NOM}$ [tH2/h], representing the nominal capacity of the plant, multiplied for the unitary production cost, comprehensive of CAPEX and OPEX, to which is then added, for the SMR, the additional cost related to the natural gas consumed, depending on the cumulated annual value of the variable $M_{t,n}^{H2,PROD,TOT}$, representing the $H_2$ produced in node n at the timestep t.

$$\begin{aligned} TPC^{HSC} = \sum_n [ & \left(UPC_n^{CAPEX} + UPC_n^{OPEX}\right) \cdot \\ & \cdot M_n^{H2,PRD,NOM} + UC^{NG} \cdot m_n^{NG,SMR,SP} \cdot \\ & \cdot \sum_t M_{t,n}^{H2,PROD,TOT} ] \end{aligned} \quad (4.5)$$

The installation and operation of hydrogen pipelines is associated to a total cost function linearly depending on of the variable $M_{n,n'}^{H2,EXC,NOM}$ [tH2/h], representing the maximum flow rate delivered between nodes n and n'. To the installation cost is then added an operating cost for each tonne of $H_2$ moved by the pipe ($M_{t,n,n'}^{H2,EXC}$, [tH2/h]). The binary variable $\lambda_{n,n'}^{H2,PPL}$ is defined with a big-M constraint, forcing the hydrogen exchanged to be equal to zero if $\lambda_{n,n'}^{H2,PPL}$=0.

$$\begin{aligned} TPC^{HSC} = \sum_{n,n'} [ & (\alpha^{H2,PPL} \cdot M_{n,n'}^{H2,EXC,NOM} + \\ & + \beta^{H2,PPL} \cdot \lambda_{n,n'}^{H2,PPL}) \cdot LD_{n,n'} + c^{H2,OP} \cdot \\ & \cdot \sum_t M_{t,n,n'}^{H2,EXC} ] \end{aligned} \quad (4.6)$$

$$M_{t,n,n'}^{H2,EXC} \leq M * \lambda_{n,n'}^{H2,PPL} \quad (4.7)$$

## 4.2. Constraints

The cost minimisation problem is constrained by a set of additional equations and inequalities, necessary for guaranteeing the energy and mass conservation in each node of the infrastructure.
The electricity balance is applied to the whole infrastructure at each hour t and includes the power generation and the demand requested by the consumers.

$$\sum_n \left( E_{t,n}^{GEN} - \frac{E_{t,n}^{CONS}}{\xi^{ELC}} \right) = 0 \quad (4.8)$$

The $CO_2$ mass balances is instead applied for each node $n$ at each timestep $t$, in which the total $CO_2$ captured has to be in equilibrium with the net $CO_2$ flow delivered to the other nodes, defined as the matrix product between the node-line incidence matrix $a^{N,L}$ and the $CO_2$ exchanged between nodes n and n', and the amount stored in the dedicated sites.

$$\begin{aligned} M_{t,n}^{CO2,CAPT} + a^{N,L} * M_{t,n',n}^{CO2,EXC,PPL} + M_{t,n}^{CO2,EXC,SHP} = \\ = M_{t,n}^{CO2,STOR} \end{aligned} \quad (4.9)$$

The captured $CO_2$ is provided as the sum of two contributions, determined by the CCS section installed on the $CO_2$-intensive plants and $CO_2$ sequestered in the SMR. The $CO_2$ captured from industrial sources depends on the $CO_2$ emission specific to one production unit, the performance parameters of the capture section and a binary variable $\lambda_n^{CCS}$, equal to 1 if CCS is installed in node n, or 0 otherwise (4.31).

$$\begin{aligned} M_{t,n}^{CO2,CAPT,CCS} = \lambda_n^{CCS} \cdot C_n^{MAX} \cdot m_n^{CO2,SP} \\ \cdot prod_{t,n} \cdot \rho_n^{CCS} \cdot \eta_n^{CAPT} \end{aligned} \quad (4.10)$$

Alongside the $CO_2$ mass balance, to each node and timestep is imposed a $H_2$ conservation balance, imposing the equilibrium among the hydrogen produced, the net $H_2$ exiting node n, resulting from a matrix product between $a^{N,L}$ and the hydrogen exchanged between two nodes n and n', the demand, and the quantity exchanged with the storage tanks.

$$\begin{aligned} M_{t,n}^{H2,PROD} + a^{N,L} \cdot M_{t,n,n'}^{H2,EXC} = \\ = M_{t,n}^{H2,CONS} + M_{t,n}^{H2,STR} \end{aligned} \quad (4.11)$$

For what concerns NGCCs, a set of constraints is introduced for describing the different $CO_2$ emission mitigation strategies applicable to such nodes. In detail, the combined cycle can exploit hydrogen delivered by the HSC or a $CO_2$ capture technology can be installed. Additional pathways occur instead if a SMR is integrated with the combined cycle. Due to the low flexibility of the integrated NGCC-SMR systems, at each timestep the node cannot simultaneously export $H_2$ to the HSC and generate electricity.

$$prod_{t,n} \leq M * (1 - \lambda_{n,t}^{EXC,SMR}) \quad (4.12)$$

$$M_{t,n}^{H2,PROD} \leq M * \lambda_{n,t}^{EXC,SMR} \quad (4.13)$$

The $H_2$ mass balance expressed in Eq.(4.43) closes with the hydrogen exchanged with the storage tank, represented by the continuous variables $M_{T,n}^{H2,STR}$, assuming a positive value if $H_2$ is delivered to the storage tank, or negative values if the energy vector is injected in the $H_2$ grid, and $M_{t,n}^{H2,STR,CUM}$, representing the $H_2$ contained in the tank at each timestep. The second variable is computed as a sum between the value of the previous timestep and $M_{T,n}^{H2,STR}$. At each timestep,

$M_{t,n}^{H2,STR,CUM}$ must be positive, for physical limits, and it is imposed equal to 0 at the first operating hour.

$$M_{t,n}^{H2,STR,CUM} = M_{t-1,n}^{H2,STR,CUM} + M_{T,n}^{H2,STR} \quad (4.14)$$

The constraint set is completed with the monthly demand constraint for each node, depending on the hourly load of the plant and the $CO_2$ emission constraint, forcing the amount of $CO_2$ emitted by the model at being lower than the quantity produced in the base case, minored with a $CO_2$ emission target.

$$\sum_n M_n^{CO2,EM,MODEL} \leq \alpha^{CO2} * M^{CO2,EM,BASE} \quad (4.15)$$

# 5. Results

Due to the high computational burden, the model is optimised on two reference weeks, representative of a summer and winter period.
A first application of the infrastructure consists in the definition of a base case, in which to all the decision variables associated to the application of the $CO_2$ emission mitigation strategies is assigned value 0. Such scenario provides the reference value of the CO2 emission, from which is defined the CO2 emission constraint expressed in Eq.(4.15).

## 5.1. Case 1A – unconstrained $H_2$

The Case 1A scenario is generated optimising the infrastructure for operating in the first week of June, with a $CO_2$ emission reduction target of 0.65 with respect to the base case. The optimal configuration results with a total annual cost of 3.2 G€/y, corresponding to a CCA of 91.4 €/$t_{CO2}$, determined almost entirely by fuel consumption (65%) and CCS (34%), with RES associated to the remaining minor contribution. Hydrogen is not exploited in this scenario, due to the relevant costs.

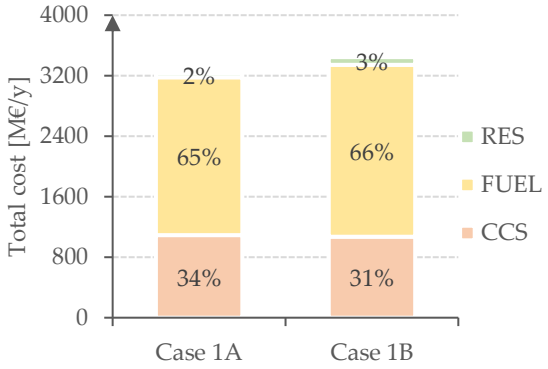


Figure 2. Total infrastructure cost in cases 1A and 1B, divided for the different components of the infrastructure

The optimal CCS infrastructure captures $CO_2$ from the nodes characterised by a lower CCA (being the cement and steel industries, PP01, PP02 and PP04), due to the high $CO_2$ partial pressure in the flue gases or to the large-size. The total amount of $CO_2$ captured within the studied is equal to 304 $kt_{CO2}$, resulting an average CCA of 57 €/$t_{CO2}$ for the capture sections.
The optimisation algorithm selects pipeline as the cheapest $CO_2$ transport modality, with a cost specific to the transported flow rate equal to 2.92 €/$t_{CO2}$, significantly higher than the value of 2 €/t reported in literature since scale economies are not modelled.
The captured $CO_2$ is delivered towards the two closest geological storage sites (CS12 and CS13), with enough storage capacity for allowing the infrastructure to operate for respectively 10 and 24 years.
For what concerns RES, the infrastructure saturates the maximum threshold imposed for the installation of solar PV capacity, increasing the pre-existent generation capacity of 20% by installing 572 MWEL of solar PV panels, with a total cost of 55.4 M€/y, having a higher availability with respect to wind power in the period analysed.

## 5.2. Case 2A – constrained $H_2$

The lack of an HSC in the optimal configuration resulting for Case 1A determined the need for developing an alternative scenario, in which the diffusion of hydrogen-based systems in the infrastructure is forced with the introduction of a minimum $H_2$ consumption constraint, referring to the whole $H_2$ demand of the infrastructure within the studied period.

The optimal configuration resulting from Case 2A is similar, in terms of total cost, to Case 1A, with a total installation and operating cost equal to 3.3 G€/y, half of it related to the fuel consumption, while the remaining contribution is determined by the CCS and HSC chains and, in a minor part, by the RES installation.

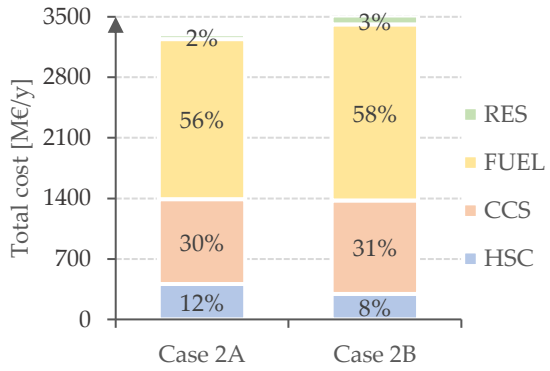


Figure 3. Total infrastructure cost in cases 2A and 2B, divided for the different components of the infrastructure

The only relevant difference between the CCS chains designed in Cases 1A and 2A is related to the SMRs installation, since among NGCCs a capture section is installed only in PP04, with a lower CCA, while the $CO_2$ emission mitigation in PP01 and PP03 occurs with the installation of SMRs. Although the mathematical model provides the possibility to export $H_2$ to the HSC, this option is not applied in the optimal configuration, with the SMRs producing an almost constant $H_2$ flow rate consumed directly in the NGCC. The total cost of the SMRs is mostly determined by the natural gas consumption, resulting a cost specific to the amount of hydrogen produced equal to 2.1 €/$kg_{H2}$. This parameter results lower for hydrogen production via electrolysis, equal to 0.93 €/$kg_{H2}$. This high value is related to lack of the electricity cost and the small size of the electrolysers installed in almost all the production nodes, being two orders of magnitude lower than the nominal size of SMR (between 1 and 21 $t_{H2}$/h), due to the presence of the maximum blending limit constraint for residential utilities, leading to capacity factors higher than 70%.

The HSC is then completed with a pipeline network, connecting production and consumption nodes, and storage tanks, contributing to a negligible part of the total cost of the supply chain.

## 6. Conclusions

The work has set the basis for the implementation of an infrastructure to economically optimise the installation and operation of a series of $CO_2$ emission mitigation strategies, being CCS, $H_2$ and RES. In order to obtain a solution in a reasonable computational time, the mathematical model is tested in four case studies, in which two different configurations are applied to a summer and a winter operating week. The resulting optimal infrastructure is characterised by a cost of $CO_2$ avoided of 91 €/$t_{CO2}$ for the two considered time periods, with a total cost of 3.2 G€/y required to reach a 65% $CO_2$ emission reduction target in the summer week, increasing to 3.4 G€/y to achieve the same target in the winter week. If not forced to be present, the HSC is not included in the optimal configuration of the infrastructure, due to the relevant installation and operational costs. When forced, the HSC favours the installation of steam methane reformers (SMRs) integrated with the NGCCs, along with a limited installation of renewable electricity-fed electrolysers, coupled with storage tanks and a pipeline transportation infrastructure, to satisfy the hydrogen demand from residential utilities. Further refinements may entail the optimisation of larger time samples , possibly implementing clustering methods to reduce the number of time steps simulated or two-step algorithms.

## 7. Bibliography

[1] International Energy Agency, "The Future of Hydrogen."

[2] International Energy Agency, "Regional opportunities–CCUS in Clean Energy Transitions." https://www.iea.org/reports/ccus-in-clean-energy-transitions/regional-opportunities#abstract (accessed Apr. 19, 2021).

[3] EEA, "Industrial Reporting Database v4 - March 2021."

[4] F. Donda, V. Volpi, S. Persoglia, and D. Parushev, "CO2 storage potential of deep saline aquifers: The case of Italy," *Int. J. Greenh. Gas Control*, vol. 5, no. 2, pp. 327–335, Mar. 2011, doi: 10.1016/j.ijggc.2010.08.009.

# Sommario

Questo lavoro discute l'ottimizzazione economica dell'installazione e del funzionamento di un'infrastruttura per la mitigazione delle emissioni di $CO_2$ da fonti industriali in una regione. Tale sistema include una rete di cattura, trasporto e stoccaggio della $CO_2$ (CCS), una catena di produzione e distribuzione dell'idrogeno (HSC) e fonti di energia rinnovabile (RES). Nel lavoro, viene definito un modello matematico per accoppiare efficacemente la progettazione e l'esercizio della suddetta infrastruttura con il carico orario delle industrie esistenti e la fornitura oraria di energia elettrica da centrali termoelettriche. Il modello matematico è testato in un caso studio esemplificativo, focalizzato su un'area geografica corrispondente alla regione italiana della Puglia, scelta per l'elevata disponibilità di energia eolica e solare e per la presenza di grandi industrie emettitrici di $CO_2$. Un problema di programmazione lineare a variabili intere e continue (MILP) viene risolto al fine di minimizzare il costo totale dell'infrastruttura e, allo stesso tempo, limitare la $CO_2$ totale emessa in atmosfera. A causa del grande carico computazionale del modello matematico, l'ottimizzazione viene effettuata per un arco temporale di una settimana, tenendo conto di due casi, rappresentativi di un riferimento estivo e uno invernale. L'infrastruttura ottimale comporta un costo della $CO_2$ evitata di 91 €/$t_{CO2}$ per entrambi i periodi di tempo considerati, con un costo totale di 3.2 G€/anno necessario per raggiungere un target di riduzione delle emissioni di $CO_2$ del 65% nella settimana estiva, che aumenta a 3.4 G€/anno per raggiungere lo stesso obiettivo nella settimana invernale. Se non forzata ad essere presente, l'HSC non è inclusa nella configurazione ottimale dell'infrastruttura, a causa dei relativi costi di installazione e di esercizio; quando forzata, l'installazione dell'HSC favorisce la produzione di idrogeno da steam methane reformers (SMRs) con cattura della $CO_2$, integrati nei cicli combinati a gas naturale (NGCC) preesistenti. A tale filiera viene affiancata l'installazione di elettrolizzatori alimentati a energia elettrica rinnovabile, serbatoi di stoccaggio e una rete di tubature, per soddisfare la bassa domanda di idrogeno da parte delle utenze residenziali, limitata da un vincolo di blend $H_2$-GN del 15% su base volumetrica.

**Parole chiave:** emissioni di CO2 da fonti stazionarie, cattura e stoccaggio della CO2, rete di produzione e distribuzione di idrogeno, programmazione lineare misto-intera, ottimizzazione economica, energie rinnovabili.

# Abstract

This work discusses the economic optimisation of the installation and operation of an infrastructure for the mitigation of $CO_2$ emission from industrial sources on a regional scale. Such system includes a carbon capture, transport and storage (CCS) network, a hydrogen supply chain (HSC), and renewable energy sources (RES). A mathematical model is defined to effectively couple the design and operation of the aforementioned infrastructure with the hourly load of existing industries and the hourly electricity supply from thermoelectric power plants. A multi-period spatially explicit mixed integer linear programming (i.e., MILP) problem is solved in order to minimise the total cost of the infrastructure and, at the same time, limit the total $CO_2$ emitted to the atmosphere. The mathematical framework is tested in an exemplificative case study, focused on a geographical area corresponding to the Italian region of Puglia, chosen due to the high availability of wind and solar energy and for the presence of large-scale $CO_2$-emitting industries. Due to the large computational burden of the mathematical model, the optimisation is carried out for a time span of one week, taking into account two cases, which would be representative of a summer and a winter reference. The resulting optimal infrastructure is characterised by a cost of $CO_2$ avoided of 91 €/$t_{CO2}$ for the two considered time periods, with a total cost of 3.2 G€/y required to reach a 65% $CO_2$ emission reduction target in the summer week, increasing to 3.4 G€/y to achieve the same target in the winter week. If not forced to be present, the HSC is not included in the optimal configuration of the infrastructure, due to the relevant installation and operational costs and a constrained $H_2$-NG blending limit of 15%vol. When forced, the HSC installation favours steam methane reformers (SMRs) with $CO_2$ capture integrated with natural gas combined cycles (NGCCs), along with a limited installation of renewable electricity-fed electrolysers, coupled with storage tanks and a pipeline transportation infrastructure, to satisfy the hydrogen demand from residential utilities.

**Keywords**: $CO_2$ emissions from stationary sources, carbon capture and storage, hydrogen supply chain, mixed integer linear programming, economic optimisation, renewable energy sources.

# Table of Contents

# List of Figures

# List of Tables

# Chapter 1
# Introduction

## 1.1 Greenhouse gases emissions and global warming

During the last decades, the energy strategies introduced for industrial and electricity generation sectors have been strongly influenced by the issue of global warming, caused by the emission to the atmosphere of substantial amounts of anthropogenic greenhouse gases (i.e., GHGs), among which carbon dioxide ($CO_2$). According to the Intergovernmental Panel on Climate Change (IPCC), the extent of global warming can be evaluated as the increase in the global air and sea temperatures, averaged over a 30-years period, with respect to the pre-industrial level, approximated to the period 1850–1900 [1]. The assessment of the impact of human activity on the extension of this phenomena has been conducted with two different models, simulating the global temperature increase with and without the human activity contribution (Figure 1.1) [2]. A comparison between the modelled temperature profiles with the empirical data highlights human's marked influence on the global warming extension. The human impact on the earth's climate is linked to the greenhouse effect, in which the thermal radiation emitted by the planet surface is absorbed by the GHGs dispersed in the atmosphere [3]. Although this natural phenomenon is vital for guaranteeing the thermal equilibrium of the planet, the atmospheric GHGs concentration increase due to human activities obstacles the heat exchange between Earth and the external environment, determining the increase in the global temperature.

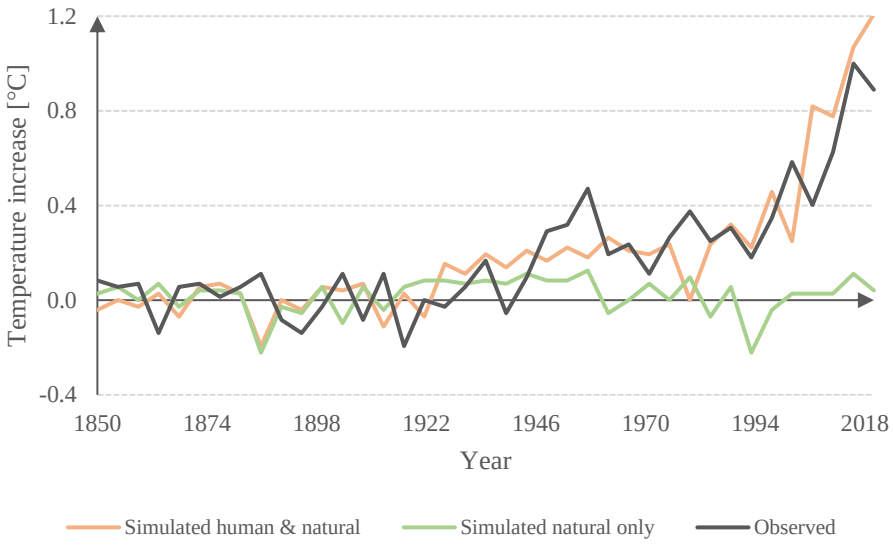


Figure 1.1. Global temperature increase profile in the period 1850-2018 [2]. The temperature increase is referred to the 1850 level.

The global response to the climate change issue occurred with the introduction of a series of policies. In 2015, the state members of the United Nations signed the Paris Agreement, setting long-terms goals for guiding the behaviour of these countries in the next decades to prevent the global temperature increasing above 2°C within this century, while pursuing efforts for limiting the temperature increase below 1,5°C [4]. A global temperature increase exceeding these thresholds is predicted to determine a substantial increase in the intensity and frequency of environmental anomalies, like shifting rainfall patterns, rising sea levels and increasing ocean acidification, and local extreme events, including floods, droughts, and heat waves [2]. Among the GHGs reduction required for reaching the goal set in the Paris Agreement, a particular effort must be focused on carbon dioxide ($CO_2$). Despite the relatively low global warming potential (i.e., GWP), representing the time period in which a GHG remains active in the atmosphere [5], $CO_2$ determines the major contribute to the greenhouse effect amplification due to the huge amount emitted from human activities (Figure 1.2) [6].

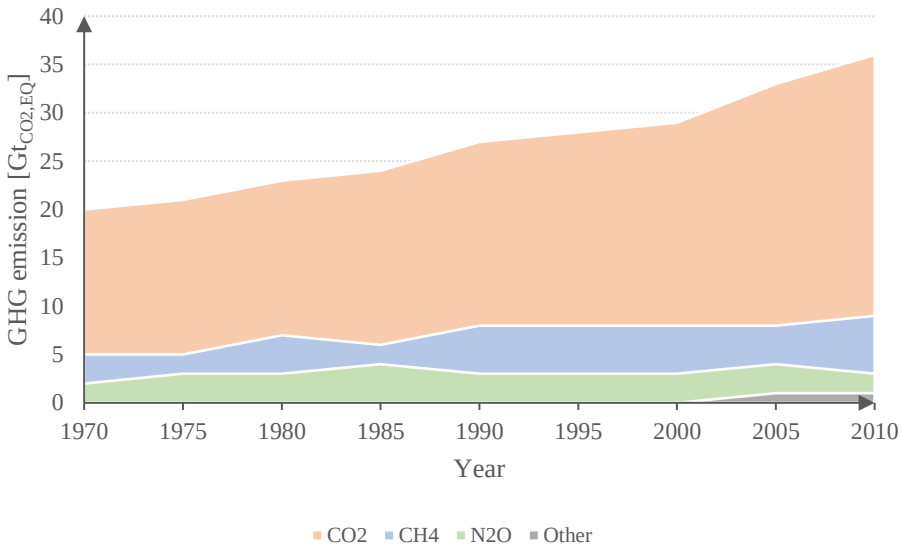


Figure 1.2. Annual GHGs emissions, divided by chemical specie [6]. The amount of GHGs emitted is expressed in $CO_2$ equivalent, defined as the equivalent amount of carbon dioxide with the same GWP [5].

Currently, the main anthropogenic $CO_2$ source is related to the energy use, including all the thermal and electricity consumptions related to human activities, accounting for 73% of the total global $CO_2$ emission. The remaining $CO_2$ intensive processes are classified into three categories, in detail agriculture, forestry and land use (18%), non-energy-related industry (5%) and waste (3%) (Figure 1.3a) [7]. Among the energy-related $CO_2$ emission (Figure 1.3b), the major source consists in stationary sources, including the contributions of electricity and heat generation (42%) and industry (23%). Another major $CO_2$ source is represented by transport sector (25%), followed by residential (6%) and other minor sources (4%) [8]. The importance of stationary sources is also confirmed by the trend of the global $CO_2$ emission in the period 1990-2018 (Figure 1.3c) [8], characterised by a continuous growth in the stationary source shares, especially the energy generation contribution. For these reasons, a substantial reduction in the $CO_2$ emission from these sources can play a key role for reaching the goals set in the Paris Agreement.

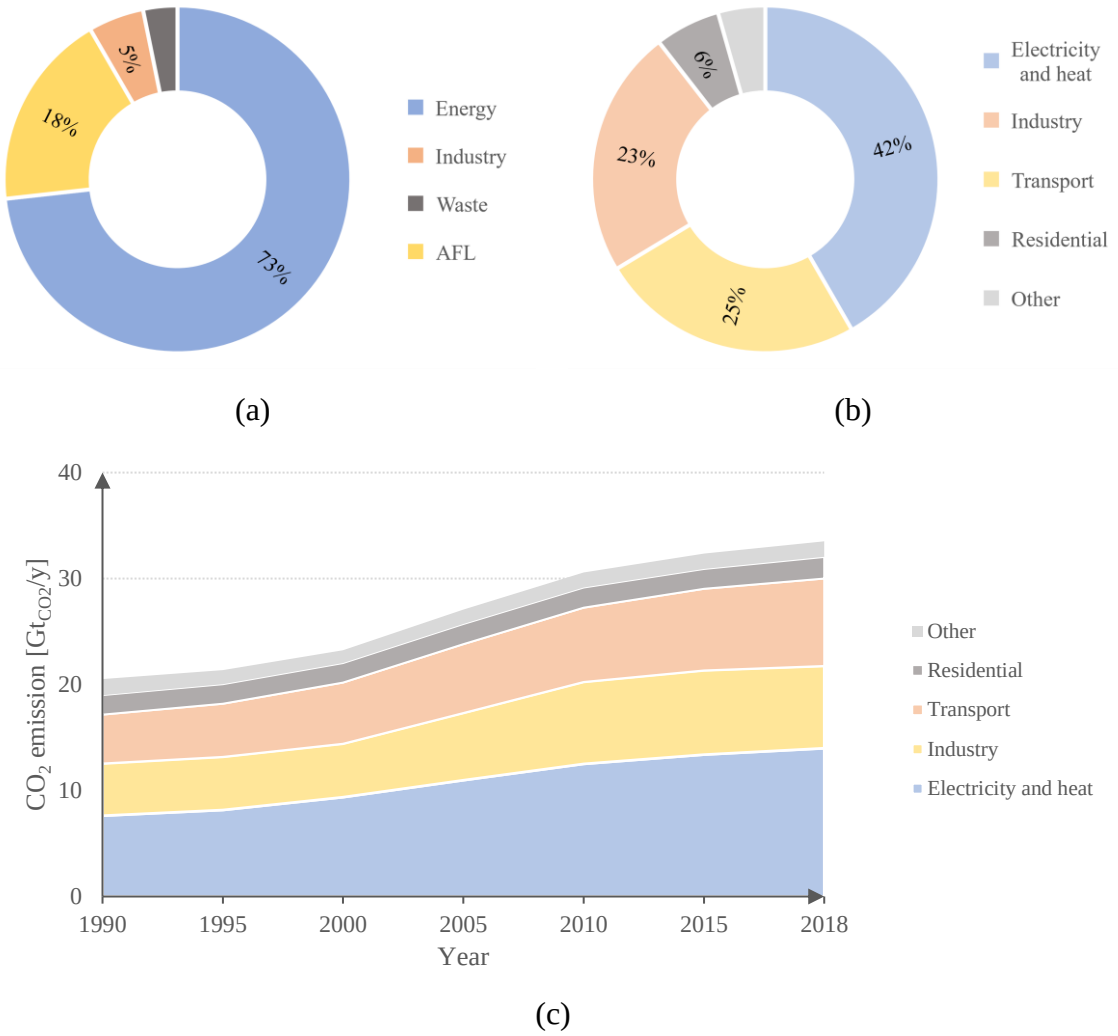


Figure 1.3. (a) Global $CO_2$ emission shares in 2018, divided by source [7]; (b) global energy-related $CO_2$ emission shares in 2018, divided by sector [8]; and (c) global annual energy-related $CO_2$ emission trend, for the period 1990-2018 [8].

The energy-related $CO_2$ emissions maintain similar shares also for Europe (Figure 1.4a) [9]. Stationary sources still determine the majority of the total $CO_2$ produced, however electricity and heat, and industry sector shares reduce, respectively, to 35% and 19%. This results in an increase in the transport (28%), residential (11%) and other sources (7%) shares. The European $CO_2$ emission trend in the period 1990-2018 (Figure 1.4b) [9], instead, provides a marked difference with respect to the global trend, being characterised by a reducing amount of $CO_2$ emitted each year. This trend is coherent with the emission reduction targets set by a succession of climate policies in the last decades, focused mainly on the stationary sources, whose contribution reduced from 3.3 $Gt_{CO2}$ in 1990 to 2.2 $Gt_{CO2}$ in 2018, and less effective for the transportation sector, characterised by a slight increase in the $CO_2$ emission along the period analysed.

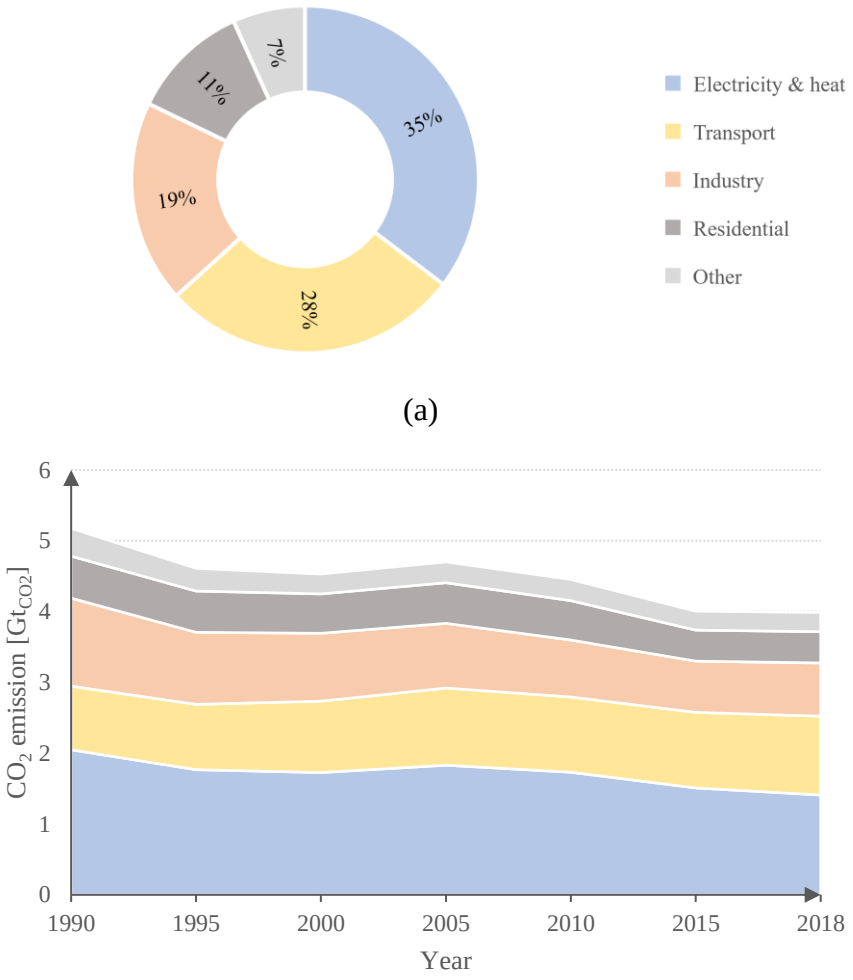


Figure 1.4. (a) European energy-related $CO_2$ emission, divided by sector: (a) shares in 2018 [9]; and (b) annual trend, for the period 1990-2018 [9].

## 1.2 Greenhouse gases emissions in Italy

In Italy the $CO_2$ emission shares are in line with the charts reported in Figure 1.4a, with the electricity and heat generation providing the major contribution (32%), together with the transportation sector, followed by the industrial and residential shares, both equal to 14% (Figure 1.5a) [10]. For what concerns the industrial $CO_2$ sources, fuel refinery and cement and steel industries are responsible for the 82% of the overall emission from this sector (Figure 1.5b) [11].

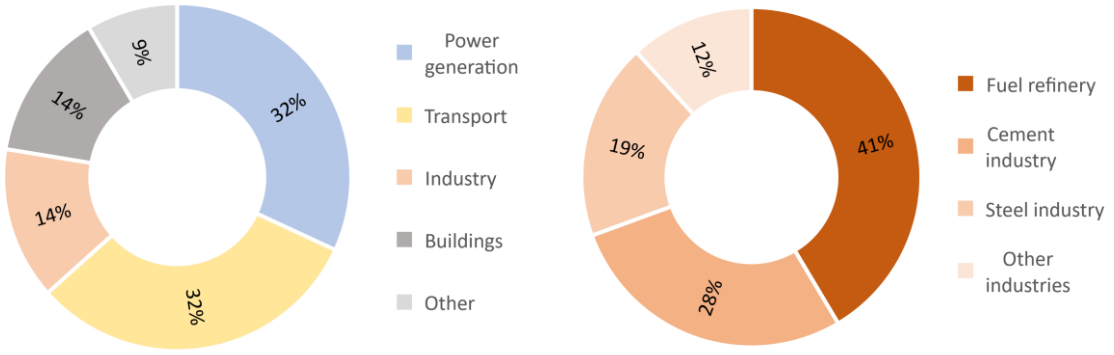


(a) (b)

Figure 1.5. Italian energy-related $CO_2$ emissions shares in 2018: (a) among sectors [10]; and (b) related to the industrial sector [11]

The trend of the energy-related $CO_2$ emission (Figure 1.6) [10] highlights the effort made by the country for mitigating the GHGs release into the environment from the industrial and energy sectors: in 2018, the amount of $CO_2$ produced from these sources reduced of around 50% for industries and more than 30% for thermoelectric power plants, with respect to the 2005 values. For what concerns the Italian energy mix, the evolution in the last three decades reported in shows the progressive reduction in the fossil fuel share, especially oil and coal, favouring the wide spreading of solar photovoltaic (i.e., PV), wind turbines and other renewable sources (i.e., RES), including geothermal, biomass and waste (Figure 1.7) [10].

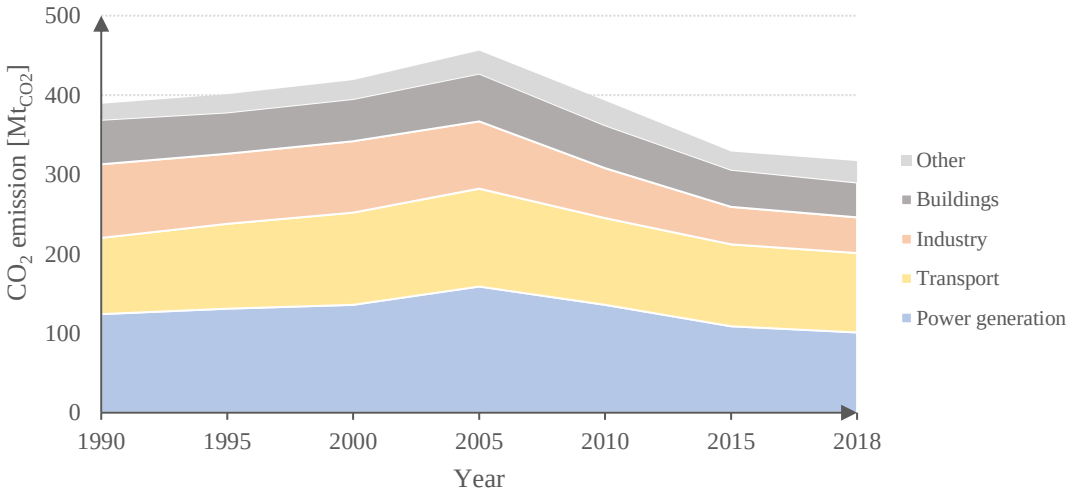


Figure 1.6. Trend of the energy-related $CO_2$ emissions for each sector in the period 1990-2018 [10]

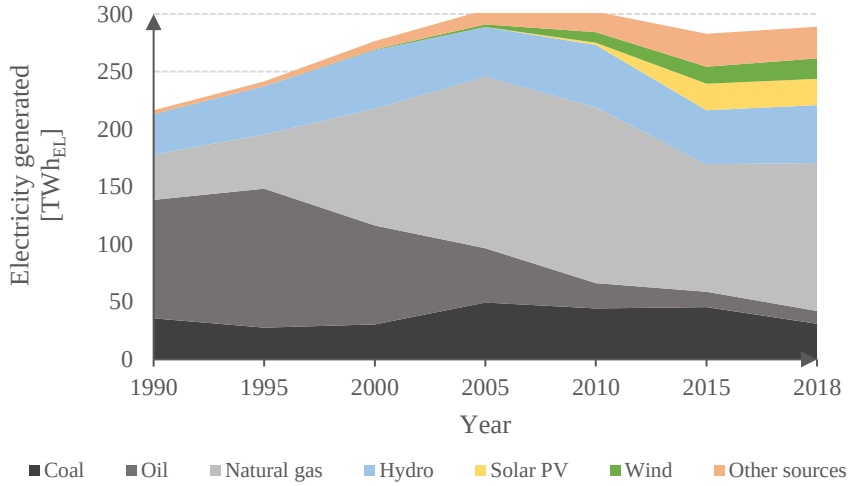


Figure 1.7. Trend of the energy generation for each source in the period 1990-2018 [10]. The voice "other sources" includes the contributes of geothermal, biomass, waste, and other renewable energy sources.

The majority of the renewable capacity installed on the national territory is sited in Southern Italy, accounting for the 86% and 33% of the national electricity generation from wind and solar PV [12]. Among the region located in this area, the role played by Puglia (Figure 1.8) stands out, resulting the first Italian region in terms of renewable energy generation, producing around 4.59 $TWh_{EL}$ and 3.44 $TWh_{EL}$ from wind and solar PV in 2018 [12].

Despite this RES availability, the region emits a consistent amount of $CO_2$ every year, due to the presence of 11 active facilities producing more than 300 $kt_{CO2}$/y each, including fuel refineries, coal-fuelled power plants, natural gas combined cycles (i.e., NGCCs), cement, steel, and chemical industries [11]. Among these facilities, the steel industry sited in Taranto stands out as one of the most $CO_2$-intensive in Europe within this sector, with a CO2 emission of more than 10 $Mt_{CO2}$ in 2018 [11], equal to almost half of the regional value.


Figure 1.8. Geographical location of Puglia region (in yellow).

## 1.3 Thesis objectives and structure

The presence in the Puglia region of an intense industrial activity and the availability of renewable electricity makes this area suitable for the topic of this thesis, aiming at reducing the $CO_2$ emissions of a region by designing an infrastructure to coordinate the application of different mitigation strategies. In order to maximise the amount of $CO_2$ avoided, the infrastructure encompasses the installation and operation of a three main technologies, being:

- a hydrogen supply chain (i.e., HSC), in which hydrogen is generated from low $CO_2$-emitting processes and then transported to the final consumers,
- a carbon capture and storage (i.e., CCS) network, removing $CO_2$ from the industrial sources for then storing it into underground storage sites,
- additional wind and solar PV power capacities.

Alongside the installation and operation of these $CO_2$ emission mitigation strategies, the infrastructure controls the hourly load of industries and power plants in order to satisfy the monthly demand for each industrial product and the electricity demand at each timestep. The coordination of all the elements composing the infrastructure requires the introduction of a mathematical model, expressed as a Mixed Integer Linear Programming (MILP) problem for the minimisation of the total cost of the systems, with a set of linear constraints, including, for instances, the mass and energy balances, the monthly demand satisfaction and the $CO_2$ emission reduction target. The solution of the MILP problem provides the optimal configuration of the infrastructure, determining the optimal interaction between the different $CO_2$ emission mitigation strategies. Moreover, the results

can be interpreted to compare the economic and technological readiness levels among these systems, basing on their level of penetration in the optimised infrastructure.

The design and optimisation of the infrastructure is discussed in the thesis through a series of chapters, organised as follows. Chapter 2 is focused on the literature review, examining the state of the art of the components of the infrastructure and reviewing the previous works published on similar topics. Then, the study proceeds with Chapter 3, providing a more detailed overview of the area analysed, in terms of energy consumption, generation and emissions, along with the definition of the nodes composing the infrastructure. A mathematical model is then introduced in Chapter 4 for describing the interaction between the different elements, followed by Chapter 5, presenting and discussing the results, and Chapter 6, dedicated to the conclusions and final remarks on the model analysed.

# Chapter 2
# Literature review

This chapter provides the state of the art of HSCs and CCS networks, presented through a description of the technological options considered in this work, along with their current and future roles in the energy generation and industrial sectors and a review of the studies published on the design of such infrastructures.

## 1.1 Hydrogen Supply Chain

A Hydrogen Supply Chain encompasses all the phases required for providing $H_2$ to the final users, from the production of this energy vector (e.g., from other fuels or electricity), to the assessment of a transportation infrastructure to final use.

### 1.1.1 Hydrogen production

One of hydrogen main advantages is the possibility of being produced from a multitude of energy sources and technologies. This section only deepens two echelons, consisting in the production from natural gas via steam methane reforming and CCS (i.e., blue hydrogen) and the generation from water and renewable electricity via electrolysis (i.e., green hydrogen). The other production technology currently applied is the gasifier, exploiting coal, biomass or other heavy fuels as feedstock, however only blue and green hydrogen echelons have been included in this thesis, due to the low environmental impact, in terms of $CO_2$ emissions, and to the availability of the energy sources in the region analysed.

Natural gas is currently the most common energy source for hydrogen production, satisfying the majority of the $H_2$ demand requested, nowadays, by ammonia and methanol industries, and fuel refineries [13]. This occurs through the steam methane reforming reaction (2.1), in which natural gas, represented by a generical hydrocarbon $C_nH_m$, is combined with water producing a syngas, composed by carbon monoxide (i.e., CO) and hydrogen.

$$C_nH_m + nH_2O \rightarrow nCO + \frac{m}{2} * H_2 \quad (2.1)$$

The current widespread technologies for generating this reaction are the Steam Methane Reformer (i.e., SMR) and the Auto Thermal Reformer (i.e., ATR), in which the heat required for feeding the steam reforming reaction is provided, respectively, through an external or internal natural gas combustion [14]. This component is then followed by another reactor, in which the water gas shift reaction (i.e., WGS), provided in Eq.(2.2), occurs.

$$CO + H_20 \rightarrow CO_2 + H_2 \quad (2.2)$$

The exothermicity of the reaction requires to limit the temperature increase, detrimental for the conversion efficiency. This purpose is achieved through a heat exchanger, producing superheated steam that is then expanded in a turbine, generating electricity. By exploiting fossil fuels, both as heat source and feedstock, hydrogen production from this echelon still determines a non-negligible $CO_2$ emission, unless a pre-combustion CCS section is introduced (Figure 2.1).

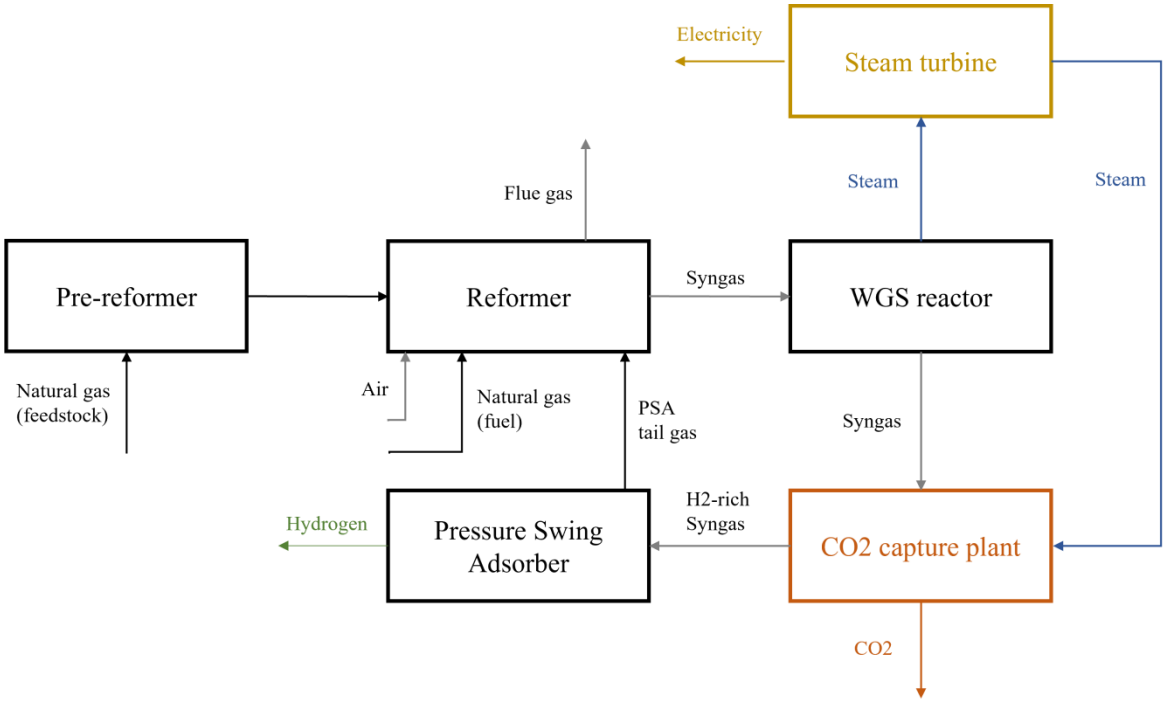


Figure 2.1. Simplified scheme of a SMR-CCS plant [14]. Along with the components discussed in the main text, the scheme includes a pre-reformer for a first breakage of the hydrocarbon chains, and a pressure swing absorber for hydrogen purification.

The $CO_2$ capture plant allows to reduce the $CO_2$ emission up to 60% [14], although this process requires a huge thermal input, provided as superheated steam withdrawn from the steam turbine, and therefore reduces the electricity generated as a co-product [14]. This

feature reduces the potential economic income linked to the electricity injection in the grid, increasing the total cost of the plant. Several SMR-CCS plants are operative worldwide nowadays, with a total annual production of around 0.5 $Mt_{H2}/y$ [13]. Although ATR is currently used for hydrogen production, the most widespread technology at large scale is SMR. Moreover, due to the lower costs and the large number of active plants, SMR is forecasted to maintain this central role in the near future [13], therefore this study only considers this type of steam methane reforming reactor, coupled with a carbon capture section.

The other energy source considered for hydrogen production is renewable electricity, exploited for splitting water into hydrogen and oxygen through an electrolysis reaction. This option is rarely applied nowadays, counting for less than 0.1% of the $H_2$ global production [13], mostly due to its disadvantageous economics with respect to a SMR. However, in the near future hydrogen production via electrolysis is predicted to acquire more importance, as an alternative to batteries for storing renewable electricity. This prediction is also based on the absence of direct $CO_2$ emission from such plants and the progressive cost reduction of the energy source exploited. This forecast is confirmed by the energy policies recently introduced by several countries. The Green Deal signed in 2020 by the State members of the European Union provides a hydrogen strategy, in which this energy vector is considered a key for increasing the RES fraction in the energy mix, through the installation of at least 6 GW of renewable hydrogen electrolysers by 2024, and 40 GW by 2030 [15].

The electrolysis reaction occurs in an electrolyser, composed by two electrodes, cathode and anode, between which is applied an electrical potential. These elements are connected by an electrolyte, a substance capable of conducting ions, generated at the anode, or cathode, by the interaction between water and electricity. This ions, then, migrate towards the opposite electrode, where their electric charge is removed, producing hydrogen (Figure 2.2) [16]. Currently, the electrolysers technological options commercially available are alkaline electrolysers and proton exchange membrane (i.e., PEM) electrolysers, with the same operative principle but differing mainly for the type of electrolyte used. For future applications, solid oxide electrolysers (i.e., SOEC) and proton-conducting ceramic electrolysers (i.e., PCEC) are forecasted to become competitive with the current technologies due to the higher conversion efficiency (Table 2.1), however the actual technological and economic limits make this solution unfeasible for being commercially applied [17] [18]. Currently, PEM electrolyser is pointed as the most suitable for power conversion into hydrogen (i.e., P2H), being relatively small and offering good-fast response and partial load-capabilities [16], therefore this technology is selected for being applied in this thesis.

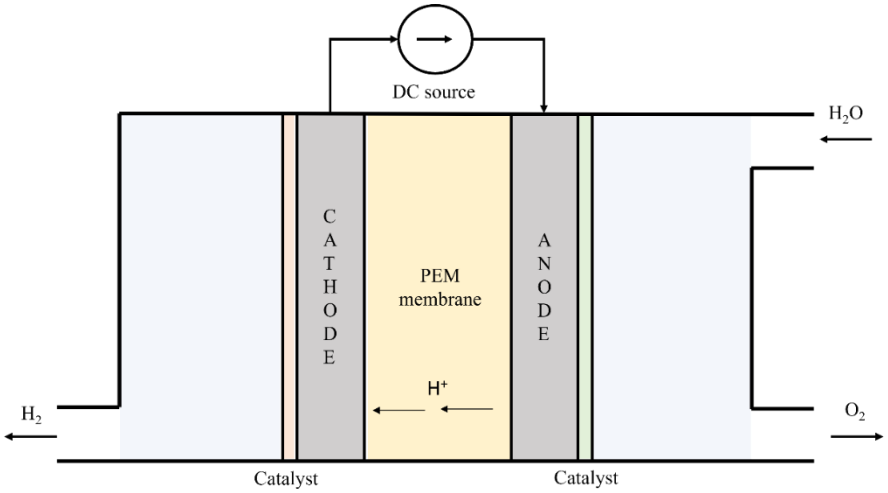


Figure 2.2. Simplified scheme of a PEM electrolyser [16]

Table 2.1. Comparison of different water electrolysis technologies [17] [18]

| | Alkaline water electrolysers | PEM | SOEC | PCEC |
|---|---|---|---|---|
| Technology status | Commercial | Commercial | R&D | R&D |
| Temperature [°C] | <120 | <80 | 700-1'000 | 700-900 |
| Pressure [bar] | 1-30 | 1-30 | 1-5 | <10 |
| Capacity [$Nm^3/h$] | 1-700 | 1-100 | 1-10 | 0.6 |
| Electric Efficiency [%] | 62-82 | 67-82 | <110 | <110 |
| Cost [€/$kW_{EL}$] | 1'250 | 2'000 | >2'100 | >2'500 |

### 1.1.2 Hydrogen transportation and storage

Currently, the most diffused transportation mode is compressed gas trailer truck, suitable for the small-scaled hydrogen systems operative nowadays. However, for a long-term local distribution application, pipelines results as the most cost-effective solution, especially for covering distances ranging from 300 to 1500 km [13]. Hydrogen transportation provides nowadays one of the major contributes for the high total cost of the supply chain, depending on the spatial scale. It is estimated that for long distances, the costs of transmission and distribution could be three times as large as the cost of hydrogen production [13]. Although the region analysed has a limited spatial extension, this thesis only considers pipeline as transportation mode, allowing the infrastructure to satisfy a potentially high hydrogen demand.

HSCs often include a storage system, important for decoupling hydrogen consumption from the production, particularly useful if the generation source is renewable electricity.

The currently available storage options for gaseous $H_2$ are geological storage into depleted natural gas or oil reservoirs, aquifers and tanks [13]. Other alternative storage modes are liquid hydrogen, with a higher energy density with respect to gaseous H2 [19], and liquid organic hydrogen carries (i.e., LOHC), liquid organic compounds that store hydrogen by means of repeated, catalytic hydrogenation and dehydrogenation cycles [19]. The last two storage options are not deepened in this section, since they have not reached a good level of economic and technological maturity yet. The application of geological storage and hydrogen tanks mostly depends on the spatial and temporal scale of the HSC: the former is suitable for large-scale systems and seasonal storage, while tanks are more applied for short term and small-scale storage [13]. This work only considers the second option, being it more adapt to the temporal and spatial scale of the problem. Moreover, geological storage would require a further analysis of the region's soil, for determining the areas suitable for this application, nonetheless safety considerations.

### 1.1.3 Hydrogen consumption

Besides the application in chemical industries and fuel refineries, hydrogen can be exploited in almost any energy-intensive sector. The main factors limiting the diffusion of this energy vector is the economical or technological unreadiness of hydrogen-based systems, like fuel cells, and the high costs required for adapting the existing industrial facilities to exploit hydrogen. The only final use included in this thesis regards the substitution of a portion of the natural gas demand from buildings and thermoelectric power plants, being easily adaptable to hydrogen exploitation as fuel.

Hydrogen can be exploited in the residential sector by injecting $H_2$ into the natural gas distribution system [13]. This solution is beneficial for the economy of the HSC, since it avoids the construction of a brand-new pipeline infrastructure, however it is limited by the different thermodynamic properties of the two fuels. In detail, the lower $H_2$ energy density reduces the one of the mixture, increasing the volumetric flow rate required for obtaining the same thermal energy output. Besides, the higher flame speed and lower flammability points make the combustion of hydrogen more difficult to control, limiting the $H_2$ fraction tolerated by the natural gas-fuelled devices. The entity of this constraint is determined by the less-tolerant system, therefore it is usually no more than some percentage points. In buildings, blending ratios are generally tolerated between 5 and 20% on a volumetric base, with a limited $CO_2$ emission reduction, unless coupled with additional efficiency measures. Nowadays, hydrogen is seldom applied in this sector, but its potentialities are being tested with 37 demonstration projects worldwide [13].

The role played by hydrogen in the power sector is nowadays negligible, accounting for less than 0.2% of the worldwide electricity generation [13]. Despite the different thermodynamic properties, most existing natural gas turbines can tolerate a hydrogen share

of 3-5 % on volumetric base, in some cases this limit can increase to more than 30%, and projected to be able to operate with 100% $H_2$ in the near future [13]. In the recent years different demonstration processes have been launched, regarding $H_2$-natural gas fed combined cycles. In Europe, a 1.32 GW plant in The Netherlands is being converted to partially operate with hydrogen [20], and another project in France exploits the hydrogen produced via electrolysis into a 12 MWe co-generation plant, obtaining a full power-to-hydrogen-to-power cycle (Figure 2.3) [21].

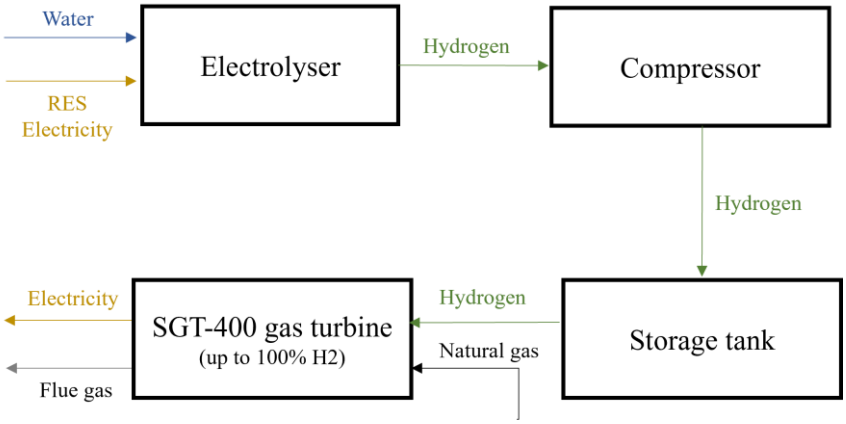


Figure 2.3. Simplified plant scheme of the 12 MWe P2H2P plant project [21]

### 1.1.4 HSC design and optimisation

During recent decades, several studies have been conducted on the optimal design of an HSC, highlighting the main challenges concerning this research field. This topic has been studied in a variety of works (Table 2.2), differing for the design choices regarding energy sources, hydrogen final uses, spatial scales and mathematical models. Particularly relevant for the topic of this thesis are blue hydrogen supply chains, in which the design procedure is integrated with a CCS network optimisation. Among them, Agnolucci et al. [22] provided a mathematical model, constituting the basis for several following works on this topic. Moreno-Benito et al. [23] and Sunny et al. [24] applied and improved this model for developing a sustainable infrastructure in the United Kingdom (UK) supporting the decarbonisation, respectively, of the transportation [23] and heat production [24] sectors. The latter, in particular, distinguishes from the majority of the HSC design studies, usually providing hydrogen to fuel cell electric vehicles (i.e., FCEVs) refuelling stations. Another work deepening hydrogen exploitation in a different sector has been conducted by Colbertaldo et al. [25], assessing the role played in a high-RES electric grid by gas turbine-based combined cycles, partially fuelled with green hydrogen.

A classification of the HSC design strategies can be applied on the spatial scale of the infrastructure. All the aforementioned works ([22], [23], [24] and [25]) , have been conducted through case studies, applying the model to an explicit geographical area, while

other researchers, including Reuß et al. [19], applied partially implicit models focused mainly on the economic assessment of the different design choices, providing a deep analysis on the different hydrogen transportation and storage modes, and relating their application limits to the temporal and spatial scale of the infrastructure.

The majority of the reviewed studies ([22], [23], [24], [25] and [19]) applied a common optimisation approach, consisting in a MILP problem with a total cost minimisation as objective function, and the $CO_2$ emission reduction target provided as inequality constraint. A different approach was developed by Li et al. [26], on an HSC design in China, with a multi-objective optimisation problem, including both the cost and $CO_2$ emission minimisation as objective functions. The results provided a set of optimal solutions, corresponding to the choice of different trade-off points between the two objective functions. Ochoa-Bique et al. [27] considered instead a mono-objective mathematical model, enriched with an additional inequality constraint, limiting the societal risk of the HSC, related to the population density in the areas surrounding a grid node and to the safety of the hydrogen-based system installed.

Another contribution on this research field is provided by Agnolucci and McDowall [28], publishing a paper in 2013 reviewing the previous works conducted on this topic. Among the variety of design choices applied for the design of an HSC, this paper highlights how only few works analysed the dependence of hydrogen price on the distance from the production plant. In 2019, another paper, published by Li et al. [29], updated the work conducted by Agnolucci et al. [21]. For multi-period optimisation problems, this paper suggests considering the evolution of the HSC by introducing the concept of capacity expansion, allowing the infrastructure to easily adapt to an increase in the demand.

Table 2.2. Main results of the literature review regarding an HSC design.

| Author | Year | Spatial scale | CCS network integration | Objective function |
|---|---|---|---|---|
| Li et al. [26] | 2008 | China | No | Total cost, $CO_2$ emission |
| Agnolucci et al. [22] | 2013 | UK | Yes | Total cost |
| Agnolucci et al. [21] | 2013 | - | - | - |
| Moreno-Benito et al. [23] | 2016 | UK | Yes | Total cost |
| Reuß et al. [19] | 2017 | - | No | Total cost |
| Ochoa-Bique et al. [27] | 2019 | Germany | No | Total cost |
| Li et al. [29] | 2019 | - | - | - |
| Sunny et al. [24] | 2020 | UK | Yes | Total cost |
| Colbertaldo et al. [25] | 2020 | Italy | No | Total cost |

## 1.2 CCS Network

CCS is an end-of-pipe $CO_2$ emission mitigation strategy, hence, it does not reduce the production of this substance, as occurs with RES or efficiency measures, but it prevents its release in the atmosphere. This goal is achieved in three phases, consisting in carbon capture from the $CO_2$-intensive process, transportation and storage. After a brief analysis of such processes, this section provides a review on the current and future projects exploiting CCS worldwide, along with the research papers discussing the design and optimisation of a CCS network.

### 2.1.1 $CO_2$ capture

$CO_2$ capture occurs with different techniques, applied accordingly to the type and size of the $CO_2$-intensive plant on technical characteristics of the plant to which it is installed. The majority of the capture technologies available nowadays can be classified into three types (post-combustion, oxy-fuel combustion, and pre-combustion), presented in the following paragraphs:

- Post-combustion carbon capture is applied on the flue gases produced in biomass or fossil fuel-based activities [30]. Before emitting these gases to the atmosphere, $CO_2$ can be separated with different techniques, among which the most frequently applied is chemical absorption. This technique involves the use of a solvent, usually an amine, removing $CO_2$ from cooled flue gases in an absorption column (Figure 2.4). After this section, the $CO_2$-rich solvent is pumped into a stripping column, in which the regeneration process occurs. This process requires a reboiler, exploiting a thermal input for generating steam, in order to strip $CO_2$ from the solvent, that is sent back to the absorption column. Steam is then removed with a condenser, obtaining cool water, then sprayed into the stripping column, and an almost pure $CO_2$ flow. The main advantage of this capture technique relies on the few modifications required for the pre-existing industrial process, since $CO_2$ is removed in the flue gases treatment section. However, the diffusion of this system is hampered by the huge thermal input required for the solvent regeneration.
- Oxy-fuel combustion occurs by burning a fuel in an environment consisting of almost pure oxygen, obtaining a mixture of mainly $CO_2$ and $H_2O$ as flue gas, from which $CO_2$ is easily removed with a condenser [30]. Oxygen is generated from air with a cryogenic air separation unit (i.e., ASU); the lack of an inert gas in the combustion chamber determines an excessively high flame temperature, which has to be limited with a partial flue gases recirculation in the combustor. For what concerns coal-based systems (Figure 2.5), oxy-fuel combustion is not affected by particularly relevant technological limits, although the presence of an ASU makes this system economically feasible only for large-scale plants. In NGCCs, however, the flue gases recirculation modifies the thermodynamic properties of the gas flow rate passing through the compressor, whose adaptation to the new operative condition requires huge investment costs.
- The last capture technology is pre-combustion capture [30], in which $CO_2$ is removed by pre-treating the fuel injected in the combustion chamber. In detail, the fuel is converted into a syngas with different modalities: for coal-based systems, this process occurs via gasification, while for natural gas it is obtained via steam methane reforming. The syngas is then turned into blue hydrogen by introducing a WGS reactor and a chemical-absorption $CO_2$ capture section (Figure 2.1), and then burned into the combustion chamber. Pre-combustion capture requires few plant modifications, and then favourable economics, only if the plant to which this system is applied already disposes of a gasifier or a SMR, otherwise its application would require huge investment costs.

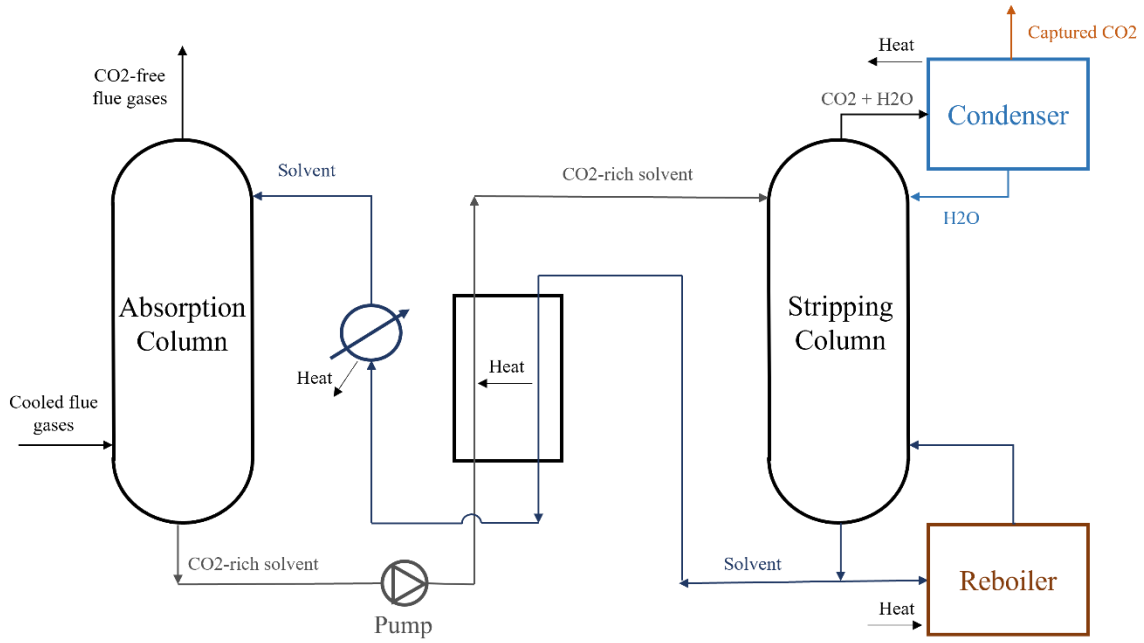


Figure 2.4. Simplified scheme of a post-combustion capture section with chemical absorption [30].

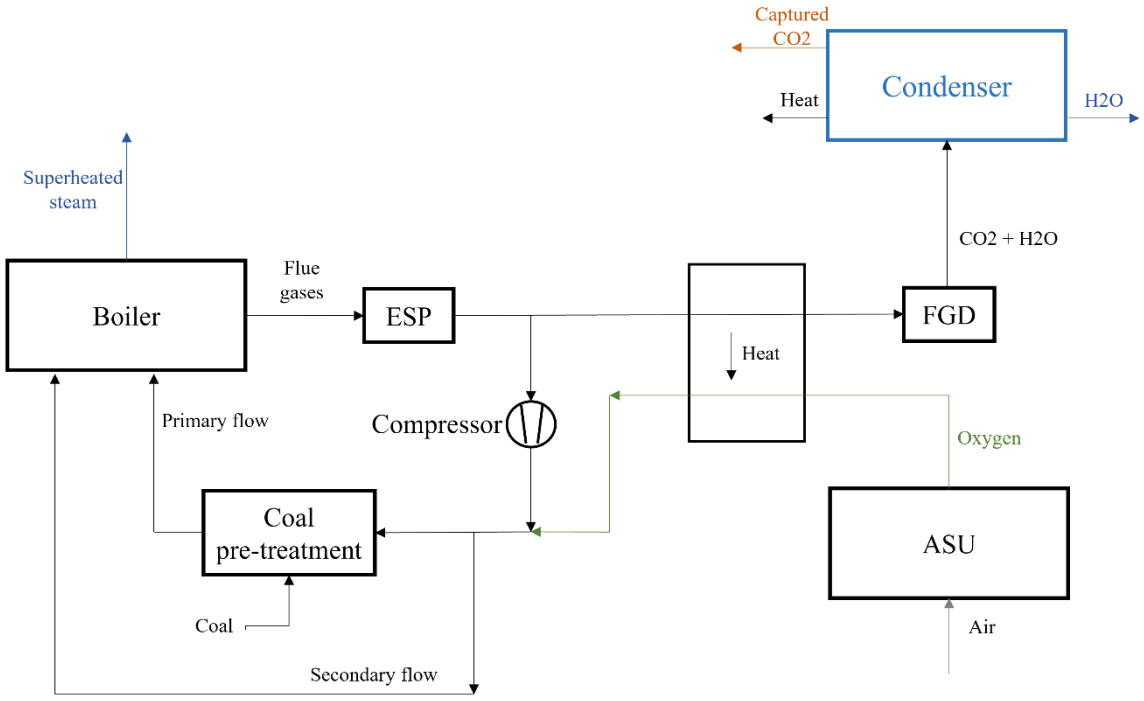


Figure 2.5. Simplified scheme of a coal-fuelled boiler with oxyfuel combustion carbon capture [30]. The recirculated flue gases are taken between the particular filter (ESP) and the sulphur oxide removal section (FGD), however a "cold recirculation" variant of this process involves a recirculation with gases taken after the FGD.

The carbon capture systems modelled in this thesis are based on the analysis of the CCS application on the main $CO_2$ emitting sectors, including power plants, cement and steel industries and fuel refineries, provided by d'Amore et al. [31]. According to that analysis, for both coal and natural gas-fed power plants, a post combustion capture results the best

solution in terms of cost, efficiency and current use in the market, while in cements plants, the cheapest solution consists in oxy-fuel combustion. Iron and steel industries include different $CO_2$ sources, for which a chemical post-combustion capture represents the best alternative in terms of cost and efficiency. Also fuel refineries present different $CO_2$ sources, whose emission can be reduced with a pre-combustion capture for the methane reformer, and a post-combustion capture for the power unit and the remaining sources.

### 1.2.5 $CO_2$ transportation

The deployment of a CCS infrastructure requires to safely and reliably transport the $CO_2$ captured from the industrial processes to the storage sites. On a medium-to-large scale, two options are available nowadays, consisting of transport via pipeline and ship, providing the two transportation modes applied in the CCS network modelled in this thesis. Other alternatives, like trucks or rail, are rarely considered being these suitable only for small scale applications, due to the higher cost required for moving each tonne of $CO_2$ [32], therefore they are not considered in this work.

The cheapest solution for large onshore distances is pipeline, also suitable for offshore applications for distances up to around 1’000 km [30]. Transport by pipeline is already deployed on large scale systems, especially in North America, with a network covering more than 8’000 km, of which more than 2’500 km are sited in the United States, transporting more than 40 $Mt_{CO2}/y$ [30].

For any spatial scale, $CO_2$ transportation via ship is a valid alternative to pipeline due to the higher flexibility, particularly useful in presence of more than one available offshore $CO_2$ storage site [32]. This feature can make ship transportation the most convenient choice in the initial development of a CCS network, for then shifting to a pipeline system when the moved $CO_2$ volumes start growing. Ship transport is currently seldom applied, mostly due to the limited demand, however its economic feasibility has already been proved, thanks to the similarity with the liquified petroleum gas (i.e., LPG) shipment [30]. For small $CO_2$ flow rate transported, ship results as the cheapest offshore solution [33].

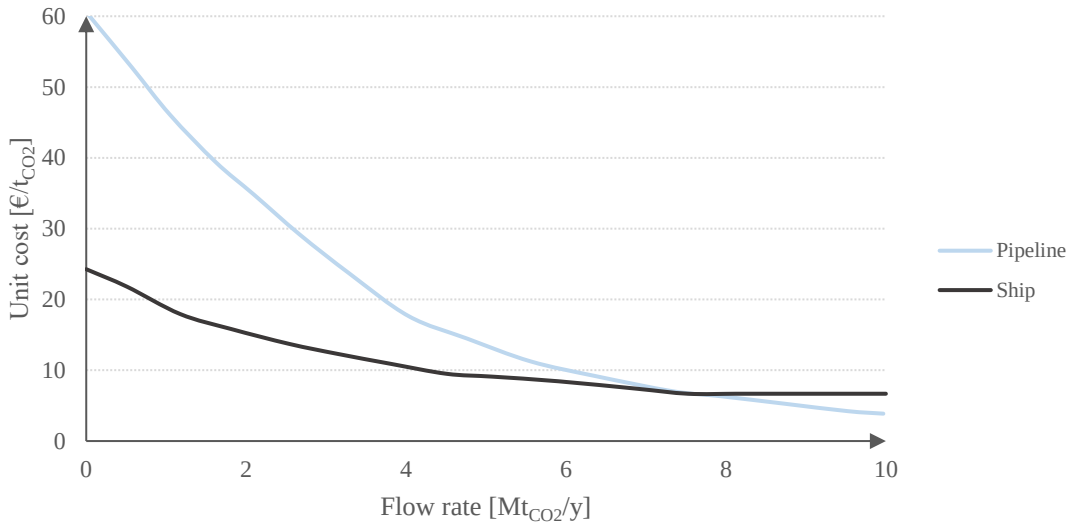


Figure 2.6. Comparison between ship and pipeline unit transportation cost for covering a 400 km distance [33]

### 1.2.6 $CO_2$ storage

The last phase of a CCS infrastructure is the injection of the captured $CO_2$ into geological reservoirs. These systems can be classified in several types, although deep saline aquifers and depleted fossil fuel reservoirs account for the majority of the available capacity [32].

Saline aquifers are composed by porous rocks overlayed by a layer of impermeable rocks, frequently available on the Earth surface in offshore or onshore sedimentary basins. A similar structure characterises depleted fossil fuel reservoirs, in which crude oil or natural gas have been trapped for millions of years before being extracted. Once a potential reservoir is detected, a geological assessment is required for determining whether or not the system is suitable for $CO_2$ storage. In detail, the external impermeable layer must have a low porosity degree to prevent $CO_2$ from leaking into the atmosphere [32]. Moreover, the pressure increase caused by the $CO_2$ injection into the porous layer can generate micro-seismic events [34], therefore an assessment of the impact of these phenomena on the seismic risk of the area is mandatory for the operation of the geological storage site. Nowadays, the cumulated capacity of the potential sites suitable for $CO_2$ storage is estimated being at least 220 $Gt_{CO2}$, far exceeding the requirement predicted in the IEA Sustainable Development Scenario [35]. Among this capacity, around 16 $Gt_{CO2}$ are estimated being available in the hydrocarbon field sited in the North Sea, constituting the largest geological reservoir in Europe [36]. The CSS network designed in this thesis relies on this storage site, along with the deep saline aquifers available in Italy [37].

### 1.2.7 CCS network design

A CCS network includes all the phases required for the $CO_2$ removal from the emission sources. Around 20 projects worldwide are operative nowadays, more than half in North America [32], and other two CCS chains are being developed in Europe. The Drax Power Limited project [38] started operating in the United Kingdom in 2019, with two pilot bioenergy plants integrated with a CCS facility, planning to commercially operate in 2027. The goal of this project is the creation, by 2040, of the world's first net zero-emitting industrial cluster, capturing $CO_2$ from power and hydrogen plants, and industrial processes, then storing it into the North Sea storage site. The same hub has a central role in the Northern Lights project in Europe [38], planned for starting to operate in 2024 and concerning the construction of the first ever cross-border, open-source $CO_2$ transport and storage network. This projects aims to offer industries from all Europe the opportunity to store their $CO_2$ in the North Sea geological reservoir through a pipeline connection between this site with onshore terminals placed on the Norwegian coast.

The development of other CCS networks in the near future can have a key role in the global $CO_2$ emission reduction, therefore it is necessary to study the current technological and economic factors influencing the design of such infrastructures. Many CCS networks have been designed in literature (Table 2.3), the majority of them modelling and solving a geographically explicit MILP problem, consisting in a cost minimisation aimed to determine the optimal location of the capture and storage sites, and to design the transport infrastructure connecting these nodes. D'Amore et al. [31] [39] applied this approach on the European scale, designing a CCS network capturing $CO_2$ from power plants, cement and steel industries, and fuel refineries, for them transporting $CO_2$ toward the storage sites with a pipeline system [31], or combining pipeline and ship transportation [39]. Similar CCS chains have also been proposed for Europe, in detail Nie et al. in UK [40], Klokk et al. in Norway [41], and Kalyanarengan Ravi et al. in Netherlands [42], all of them relying on the North Sea storage site. On the other hand, some researchers applied a spatially implicit approach, focussed specifically on the $CO_2$ transport infrastructure, rather than investigating the whole CCS network (e.g., Chen et al [43]; Jensen et al. [44]; Morbee et al. [45]). Likewise, the optimisation model proposed by Wu et al. [46] simplified the spatial representation four theoretical regions. Other projects instead considered the possibility to re-use $CO_2$ as an alternative to geological storage. Hasan et al. [47] modelled a CCUS network in the United States, injecting $CO_2$ in active oil reservoirs for Enhanced Oil Recovery (i.e., EOR), exploiting the reduction in the energy consumption required for the extraction of the fossil fuel, obtained when $CO_2$ is dissolved in crude oil.

Table 2.3. Main results of the literature review regarding an CCS network design

| Author | Year | Spatial scale | CC(U)S | Transportation mode |
|---|---|---|---|---|
| Chen et al [43] | 2010 | China, Hubei province | CCS | Pipeline |
| Morbee et al. [45] | 2012 | Europe | CCS | Pipeline |
| Jensen et al. [44] | 2013 | Canada | CCUS | Pipeline |
| Wu et al. [46] | 2015 | Regional (implicit) | CCS | Pipeline, tanker, ship |
| Hasan et al. [47] | 2015 | US | CCUS | Pipeline |
| Nie et al. [40] | 2017 | UK | CCS | Pipeline |
| Kalyanarengan Ravi et al. [42] | 2017 | Nederland | CCS | Pipeline |
| Klokk et al. [41] | 2018 | Norway | CCS | Pipeline |
| d'Amore et al. [31] | 2021 | Europe | CCS | Pipeline |
| d'Amore et al. [39] | 2021 | Europe | CCS | Pipeline, ship |

# Chapter 3
# Grid nodes definition

The spatial scale of the studied infrastructure is defined with a graph, in which a set of nodes is interconnected, exchanging electricity, $CO_2$ and $H_2$. Such nodes represent the basis for the mass and energy balances necessary for implementing the mitigation strategies analysed in the previous chapter, being hydrogen, CCS and RES, therefore the selection of the grid nodes determines the ability of the infrastructure to reduce the $CO_2$ emitted in the studied region. This chapter discusses the spatial characterisation of the infrastructure, starting with an analysis of the industrial activity occurring in the geographical area selected as case study for this thesis, providing the location of the main $CO_2$ emission sources, then included in the nodes set. The study proceeds by including additional nodes, including RES generation nodes, other energy consumption nodes, $CO_2$ storage sites and ports. After the nodes set is complete, an input/output nodal analysis is applied, assessing the mass and energy consumption and production of each element, along with other information useful for the implementation of the $CO_2$ emission mitigation strategies.

## 3.1 Region description

The geographical location selected for this work is the Puglia region, located in Southern Italy, characterised by a high availability of RES and the presence of an intense and heterogeneous industrial activity. The regional territory is organised in six provinces, being Foggia (FG), Bari (BA), Barletta-Andria-Trani (BT), Taranto (TA), Brindisi (BR) and Lecce (LE). For the purpose of this work, this area is then extended including the adjacent province of Matera (MT), in Basilicata region, for limiting the $CO_2$ emitted by a large-size cement industry close to the regional border (Figure 3.1a). This facility adds to the 10 main stationary $CO_2$ sources located in Puglia region, in detail two cement industry, one fuel refinery, one steel industry, one chemical industry and 5 thermoelectric power plants (Figure 3.1b) [11].

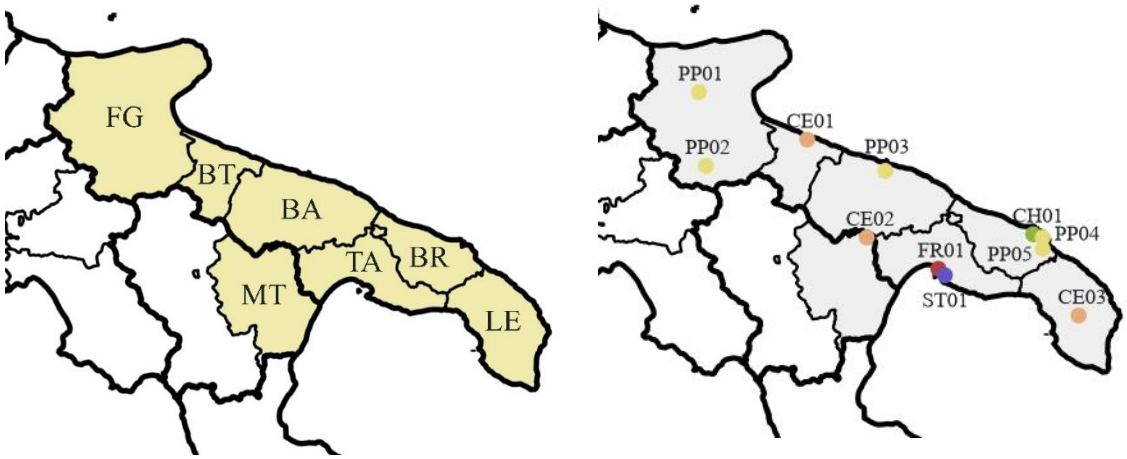


(a) (b)

Figure 3.1. Geographical location of (a) the seven provinces considered in this study and (b) the industries and thermoelectric power plants sited in the studied region.

Despite the low number of active facilities, steel industry represents the main $CO_2$ source in the region, with an annual $CO_2$ emission of 10.8 $Mt_{CO2}/y$ in 2018. The other major contribution is provided by thermoelectric power plants (9.39 $Mt_{CO2}/y$), followed by fuel refineries (1.11 $Mt_{CO2}/y$), cement industries (1.24 $Mt_{CO2}/y$) and chemical industries (0.46 $Mt_{CO2}/y$) [11]. An additional $CO_2$ emission is provided by other sources, including residential utilities and minor industries, accounting for 2.17 $Mt_{CO2}/y$ [48] (Figure 3.2a). Despite the multitude of facilities operating in the region, the 65% of the total $CO_2$ emission is determined by only two sources, being the steel industry and the coal power plant. The geographical position of these facilities strongly influences the $CO_2$ emission distribution among the provinces, characterised by a marked difference between Brindisi and Taranto provinces, in which the coal-fuelled power plant and the steel industry are located, and the rest of the region (Figure 3.2b). The same trend characterises the total fuel consumption of the area[1], with the two coal-intensive plants contributing for almost half of the overall value (Figure 3.2c).

[1] The values introduced without specifying the reference result from the input/output analysis, based on a multitude of references cited in the dedicated subsection.

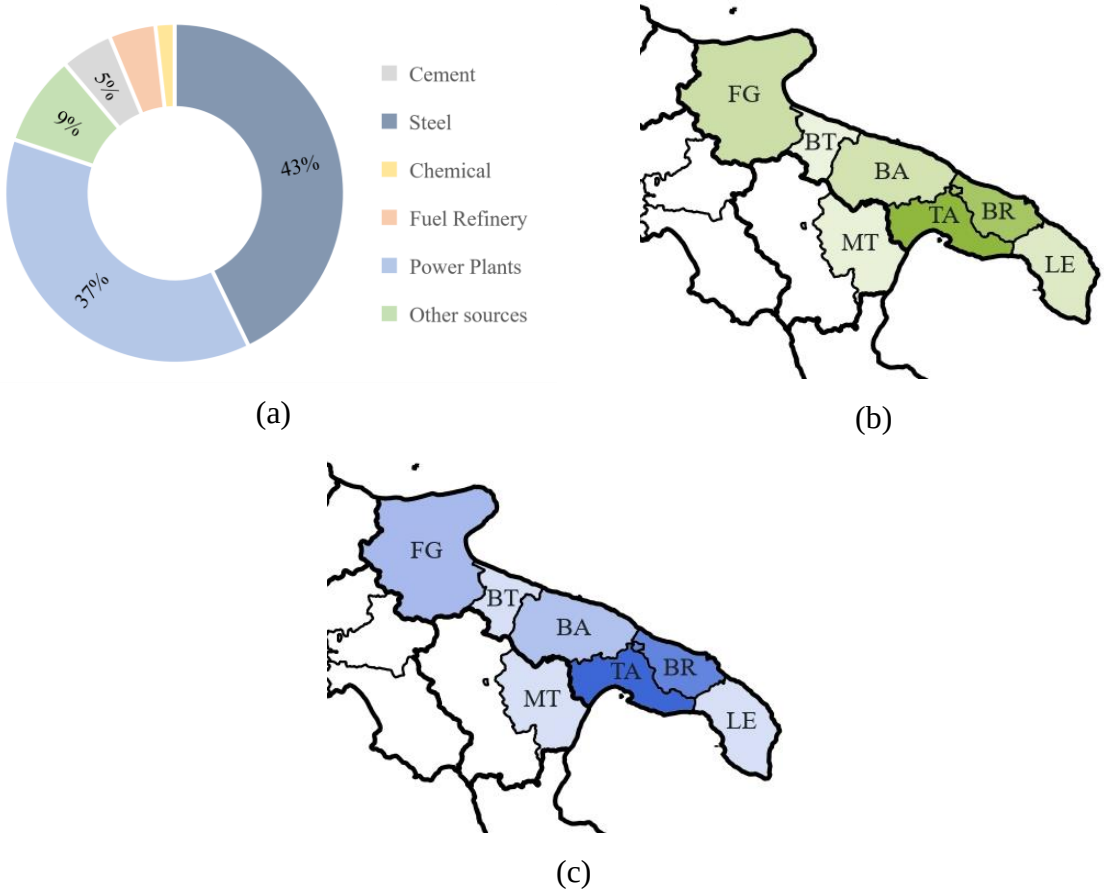


Figure 3.2. (a) $CO_2$ emission shares by sector [11]; (b) $CO_2$ emission distribution among the seven provinces analysed; and (c) total fuel consumption, including coal, dry petcoke and natural gas, distribution among the provinces.

Despite the high number of NGCCs available, their cumulated fuel consumption is slightly lower than the coal-fed power plant. This parameter, however, is not reflected in the electricity generation mix (Figure 3.3a) [49], since the main contribution is provided by NGCCs (38%), followed by the coal-fed power plant (18%). The low electrical efficiency and the high amount of $CO_2$ emitted by the coal-based facility determined a decrease, in the recent years, in the activity of the plant. In the period 2015-2018, the net capacity factor (NCF), defined as the ratio between the net annual generation and the nominal one, decreased from 63% to 25% [50], and in January 2021 one out of four generation module has been dismissed, planning to replace the whole plant with a 1'680 MW NGCC within 2025 [51]. The progressive fade out of coal in the energy sector is balanced by an inverse trend of the RES generation, especially solar PV and wind power (Figure 3.3b) [49]. The high availability of these energy sources in the area analysed determined a surge in the capacity installed in the recent years: in Puglia region, the electricity generation from wind turbines increased, in the period 2000-2018, from 150 $GWh_{EL}/y$ to almost 5'000 $GWh_{EL}/y$, while the generation from solar PV, negligible until 2008, accounts in 2018 for around 3'500 $GWh_{EL}/y$. This growth in the RES capacity determines, in the 2018 energy

generation mix of the area analysed, solar PV and wind power shares of, respectively, 12% and 17%.

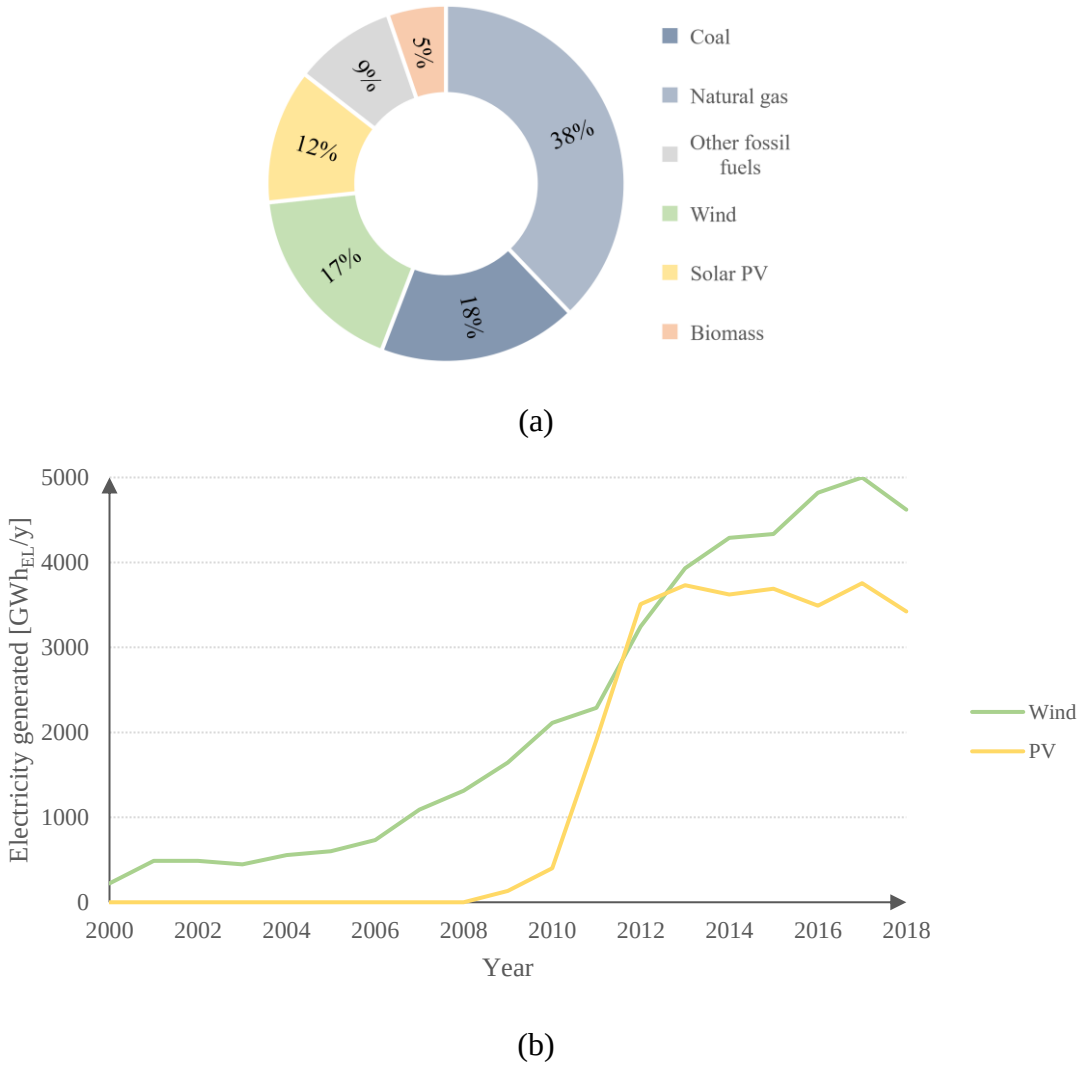


Figure 3.3. (a) Electricity generation mix in 2018 for the studied region [49]; and (b) electricity generation trend from wind power and solar PV in the period 2000-2018 [49].

The total electricity generation is distributed heterogeneously among the different provinces (Figure 3.4a), with Brindisi accounting for half of the total value of the area, due to the presence of two large-sized thermoelectric power plants. The remaining electricity is generated mostly in the provinces of Foggia, with a high availability of wind energy, and Taranto, whose contribution is strongly dependent on the thermoelectric power plant integrated in the steel industry. The presence of the large-sized steel industry also makes the province of Taranto the main electricity consumer in the area, with more than 5'000 GWh$_{EL}$/y, followed by Bari (Figure 3.4b). Although none of the $CO_2$-intensive industries is located in the second province, it still determines a major contribution in the total

electricity demand due to its wide geographical extension, in which the numerous small-sized industries and residential utilities account for a cumulated electricity consumption of more than 4'000 $GWh_{EL}/y$.

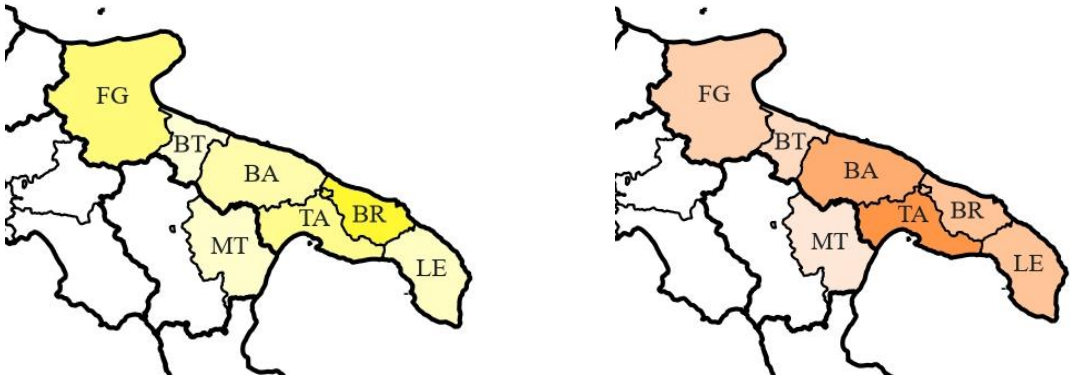


(a) (b)

Figure 3.4. Electricity generation (a) and consumption (b) distribution among the studied provinces, referred to the year 2018 [49].

The analysis of the energy and industrial sectors point Puglia region as a perfect candidate for the purpose of this thesis. This interest in such region is also shared by several private and public companies, as reflected by a series of pilot projects launched in the area for the assessment of the economic and performance assessment of $CO_2$ emission mitigation strategies, among which hydrogen and CCS. In 2011, a cooperation between ENEL and Eni provided the first CCS pilot project in Italy, regarding the "Federico II" coal-fuelled power plant sited in Brindisi [52]. Such plant operated for three years with a post-combustion carbon capture section, in which $CO_2$ is removed from flue gases and then transported towards the storage site, being a deep saline aquifer owned by Eni and sited in Northern Italy. Another project consists in the Puglia Green Hydrogen Valley, announced in September 2021 as a cooperation among Edison, Snam, Saipem and Alboran Hydrogen [53]. The goal is to install three green hydrogen plants exploiting solar PV as energy source, with an overall capacity of 220 MW, for then blending $H_2$ into the pre-existent natural gas pipeline network. Despite the limited spatial scale of the two pilot projects, with respect to the infrastructure implemented in this thesis, they show that the two $CO_2$ emission mitigation strategies could be applied in the near future.

## 3.2 Definition of nodes

The analysis of the energy and industry sectors of the area analysed provides the location of the main $CO_2$ emission sources, included in the grid nodes set. In order to maximise the $CO_2$ avoided in such plants, additional nodes are needed for the design of a CCS network, including $CO_2$ storage sites and ports, exploitable for ship transportation towards offshore

storage sites. The nodes set include also virtual elements, among which consumption and production nodes account, respectively, for the energy demand and generation not related to the industrial or thermoelectric power plant sectors. These two contributions are accounted with as many virtual nodes subsets, coincident in the geographic definition, each one composed of seven elements representing the provinces included in the studied region. A similar definition occurs for two other nodes, representing the electricity imported and exported to the other Italian regions. Although in 2018 the studied region determined a net electricity export towards the adjacent regions, the model also includes the electricity import node for allowing the infrastructure to satisfy the electricity balance constraint at each hour of the year. The nodes set is then completed with a transit node, added for facilitating the mass and energy exchanges among the infrastructure, and an offshore node, useful for determining whether a connection occurs onshore or offshore.

Each node is represented in this thesis with a unique code, composed of two letters, accounting for the node typology, and two numbers, sorting the elements of the same typology in a decreasing order with respect to the nodes latitude (Table 3.1, Table 3.2).

Table 3.1. Spatial and topological definition of the nodes composing the infrastructure (continues in Table 3.2)

| Code | Type | Latitude [rad] | Longitude [rad] | Real/Virtual |
|---|---|---|---|---|
| CE01 | Cement industry | 0.7211 | 0.2844 | Real |
| CE02 | Cement industry | 0.7099 | 0.2907 | Real |
| CE03 | Cement industry | 0.7011 | 0.3177 | Real |
| ST01 | Steel industry | 0.7069 | 0.3002 | Real |
| FR01 | Fuel refinery | 0.7068 | 0.3002 | Real |
| CH01 | Chemical industry | 0.7094 | 0.3140 | Real |
| PP01 | Power plant | 0.7266 | 0.2692 | Real |
| PP02 | Power plant | 0.7191 | 0.2701 | Real |
| PP03 | Power plant | 0.7173 | 0.2926 | Real |
| PP04 | Power plant | 0.7091 | 0.3142 | Real |
| PP05 | Power plant | 0.7080 | 0.3147 | Real |
| CN01 | Consumption node | 0.7256 | 0.2715 | Virtual |
| CN02 | Consumption node | 0.7187 | 0.2828 | Virtual |
| CN03 | Consumption node | 0.7149 | 0.2913 | Virtual |
| CN04 | Consumption node | 0.7072 | 0.2880 | Virtual |
| CN05 | Consumption node | 0.7081 | 0.3097 | Virtual |

Table 3.2. Spatial and topological definition of the nodes composing the infrastructure (continues from Table 3.1)

| Code | Type | Latitude [rad] | Longitude [rad] | Real/Virtual |
|---|---|---|---|---|
| CN06 | Consumption node | 0.7079 | 0.3012 | Virtual |
| CN07 | Consumption node | 0.7021 | 0.3175 | Virtual |
| EN01 | Electricity export node | 0.7165 | 0.2692 | Virtual |
| PN01 | Production node | 0.7256 | 0.2715 | Virtual |
| PN02 | Production node | 0.7187 | 0.2828 | Virtual |
| PN03 | Production node | 0.7149 | 0.2913 | Virtual |
| PN04 | Production node | 0.7081 | 0.3097 | Virtual |
| PN05 | Production node | 0.7079 | 0.3012 | Virtual |
| PN06 | Production node | 0.7072 | 0.2880 | Virtual |
| PN07 | Production node | 0.7021 | 0.3175 | Virtual |
| IN01 | Electricity import node | 0.7024 | 0.2851 | Virtual |
| CS01 | $CO_2$ storage site | 1.0139 | 0.0651 | Real |
| CS02 | $CO_2$ storage site | 0.7898 | 0.1575 | Real |
| CS03 | $CO_2$ storage site | 0.7896 | 0.1859 | Real |
| CS04 | $CO_2$ storage site | 0.7811 | 0.1994 | Real |
| CS05 | $CO_2$ storage site | 0.7703 | 0.2220 | Real |
| CS06 | $CO_2$ storage site | 0.7594 | 0.2356 | Real |
| CS07 | $CO_2$ storage site | 0.7457 | 0.2443 | Real |
| CS08 | $CO_2$ storage site | 0.7450 | 0.2552 | Real |
| CS09 | $CO_2$ storage site | 0.7391 | 0.2504 | Real |
| CS10 | $CO_2$ storage site | 0.7346 | 0.2570 | Real |
| CS11 | $CO_2$ storage site | 0.7319 | 0.2626 | Real |
| CS12 | $CO_2$ storage site | 0.7302 | 0.2626 | Real |
| CS13 | $CO_2$ storage site | 0.7064 | 0.2910 | Real |
| CS14 | $CO_2$ storage site | 0.6836 | 0.2997 | Real |
| CS15 | $CO_2$ storage site | 0.6619 | 0.2210 | Real |
| PO01 | Port | 0.7082 | 0.3009 | Real |
| TN01 | Transit node | 0.6666 | 0.2728 | Virtual |
| ON01 | Offshore node | 0.6944 | 0.3018 | Virtual |

## 3.3 Data collection

This section discusses the characterisation of the nodes previously defined, occurring with a description of the main processes occurring in each node, along with the monthly an annual production, size (defined as the nominal hourly production capacity), $CO_2$ emission, energy consumption and generation, and $CO_2$ storage capacity. These parameters define the role of each node in the mass and energy balances, provided in Chapter 4. Different temporal scales are considered in this section. For all the grid nodes, the input/output analysis is conducted on an annual scale, considering 2018 as the reference year, and the temporal discretisation is furtherly restricted to the monthly and hourly scales, respectively for industrial and province nodes.

The input/output analysis often requires the application of the chemical and thermodynamic properties of the chemical species analysed, due to the heterogeneity in the units of measurement of the data provided in literature, but also for relating the $CO_2$ emission to the fuel consumption with a stoichiometric balance. These thermodynamic and chemical properties are reported, for coal, dry petcoke, natural gas, $CO_2$ and $H_2$, in Table 3.3. In detail, the properties of coal are obtained considering a reference fuel with a 60% carbon content, while for natural gas the chemical and thermodynamic properties are reported by Snam, the Italian transmission system operator (TSO) of the natural gas pipeline [54].

Table 3.3. Molar mass, lower and higher heating value, and specific $CO_2$ emission of the chemical species considered in this study

| Specie | Molar mass [kg/kmol] | LHV [$MJ_{TH}$/kg] | HHV [$MJ_{TH}$/kg] | $CO_2$ emission [$t_{CO2}/t_{FUEL}$] |
|---|---|---|---|---|
| Coal | - | 26.0 | - | 2.2 |
| Dry petcoke | - | 35.0 | - | - |
| Natural gas | 17.5 | 46.4 | 51.6 | 2.5 |
| $H_2$ | 2.0 | 120.0 | 141.9 | 0 |
| $CO_2$ | 44.0 | 0 | 0 | 1.0 |

### 3.3.1 Industries

Industries represent, along with thermoelectric power plants, the main concentrated $CO_2$ sources of the studied region, therefore the $CO_2$ emission mitigation of such plants represents the main goal of the infrastructure. The industrial sector is characterised by a quite heterogeneous production for the spatial scale of the area analysed, hosting 11 large-sized facilities, being 3 cement industries, one fuel refinery, one steel industry and one chemical industry.

The interaction between the industrial nodes and the infrastructure is assessed through an input/output analysis. In detail, these nodes receive in input fuels and raw materials from external sources, while electricity is provided by the infrastructure. The output produced consists in $CO_2$, optionally captured and stored, and the final product. For what concerns the production of the plant, the infrastructure cannot modify the monthly and annual demand of the site, although it has the possibility to choose the tonnes produced at each hour, without exceeding the maximum capacity of the facility.

The main results of the input/output analysis, discussed in the following paragraphs, is reported in Table 3.4, distinguishing between the data directly available in literature and the ones determined through the introduction of some approximation (marked with an asterisk). The available information regarding the majority of the nodes is not enough for fully characterising the operation of the plants, therefore the missing parameters are estimated considering, as reference, other similar facilities, with operational parameters available in literature. All the parameters discussed in this chapter are referred to the year 2018, unless specified, being the most recent one for which the operational data of the majority of the nodes analysed can be collected.

Table 3.4. $CO_2$ emission, fuel consumption, electricity generation and consumption, annual production and nominal capacity of the industries analysed. For CE03, the coal consumption value also includes dry petcoke.

| Parameter | | CE01 | CE02 | CE03 | ST01 | FR01 | CH01 |
|---|---|---|---|---|---|---|---|
| $CO_2$ emission | [$kt_{CO2}$/y] | 306 | 520 | 420 | 10’763 | 1’114 | 463 |
| Natural gas | [$kt_{NG}$/y] | 0 | 0 | 0 | 290 | 32 | 0 |
| Coal | [$kt_{COAL}$/y] | 56* | 75* | 52 | 2’759* | 0 | 0 |
| Electricity generated | [$GWh_{EL}$/y] | 0 | 0 | 0 | 3’275 | 300 | 449* |
| Electricity consumed | [$GWh_{EL}$/y] | 51* | 72* | 67 | 3’190 | 327 | 945* |
| Product | [$kt_{PROD}$/y] | 522 | 738 | 670* | 4’335* | 4’571 | 1’560 |
| Nominal capacity | [$t_{PROD}$/h] | 127 | 103 | 129 | 529* | 574 | 262 |

Cement production is the main industrial activity in the region, in terms of number of facility installed, with five production plants sited in Barletta (BT), Matera (MT), Galatina (LE) and Taranto (TA). The main production process occurs in three phases [55], the first one consisting in mixing clay and limestone ($CaCO_3$), that are then crushed into powder form. The second phase provides a pyro-processing unit, in which the limestone

decomposes, generating lime (CaO) and $CO_2$. This reaction determines the majority of the $CO_2$ emission of the plant, along with the fuel consumed, usually coal, for providing the high temperature requested by the processes occurring in the pyro-processing unit. The third and last phase consists in the grinding of clinker, being the main output of the previous phase, into powder form, that is then mixed with additives, producing cement. Among the cement plants located in the area, the two industries sited in Taranto have been converted, before 2015, in grinding workshops [56], processing the clinker received from other plants. Since this process is responsible only of a minor fraction of the $CO_2$ emitted from a cement plant, this thesis only considers the facilities sited in the provinces of Barletta (CE01), Matera (CE02) and Lecce (CE03).

The first cement plant analysed is sited in Barletta and owned by Buzzi Unicem. The information on the operative parameters of such plant available in literature regard the nominal production capacity of 1 $Mt_{CEMENT}$/year [57], the monthly distribution of the operative hours [58], with an annual cumulated value of 4'157 h/y, and the annual $CO_2$ emission. For what concerns the annual $CO_2$ produced by the plant, the reference considered in this study is the database provided by the European Environmental Agency (EEA) [11], reporting the $CO_2$ emission of the major carbon-intensive industries sited in Europe, including all the facilities considered in this study. The remaining values reported in Table 3.4 are not available in literature, therefore their computation occurs with the introduction of some assumptions. The first hypothesis regards the $CO_2$ emitted by the plant, caused for around 60% by the limestone decomposition reaction, while the remaining part is mainly related to the fuel consumption [55]. Since the plant is almost entirely fed with coal [59], from the $CO_2$ emitted in the fuel combustion process it is possible to estimate the fuel requirement of the facility. Another assumption introduced in this analysis regards the operation of the plant, assumed producing at the nominal capacity for all the operative hours, allowing to compute an estimation of the annual production of the facility. The third and last hypothesis is introduced for computing the annual electricity consumption, assuming a reference value, specific to the annual production, of 0.097 $MWh_{EL}/t_{CEMENT}$ reported by Voldsund et. al [60]. Comparing the extensive electricity consumption value, resulting around 51 $MWh_{EL}$/y, with the electricity demand of the cement-lime-gypsum production sector in the Province of Barletta, reported by Terna [61] as equal to 58 $MWh_{EL}$/y, the approximation introduced is quite accurate, since the CE01 facility contributes for almost the entire electricity consumption of the sectoral activity in the province.

The cement production plant CE02 is sited in Matera (MT), characterised by an annual nominal capacity of 0.9 $Mt_{CEMENT}$/y [62] and owned by Italcementi. The only information on the operation of the plant in 2018 regards the annual $CO_2$ emission [11], and the monthly distribution of the operative hours along the year [63], with a cumulated value of 7'180 h/y, therefore the introduction of a series of assumptions is required for computing

the missing parameters. In detail, a first hypothesis introduces a coal consumption specific to the annual production of 2'331 $MJ_{TH}/t_{CEMENT}$, value reported by Italcementi as the average among of the cement industries owned by the company [64]. Other assumptions are then introduced for the estimation of the annual production and electricity consumption, occurring analogously to the CE01 plant.

The last cement industry analysed, CE03, is sited in Galatina (LE) and owned by Colacem S.p.A., with an estimated nominal annual capacity of 1.1 $Mt_{CEMENT}/y$. The majority of the data regarding this plant is provided privately by the company [65], although the annual production and the nominal capacity are not available in literature. The computation of these parameters, then, requires the introduction of some hypothesis, being the constant nominal load assumed for the plant at each operative hour, and the specific $CO_2$ emission. The last value is chosen, accordingly to the study conducted by Voldsund et al. [60], as equal to 0.626 $t_{CO2}/t_{CEMENT}$ for cements with a clinker-on-concrete ratio of 0.737. Once the annual production is computed, the assessment of the accuracy of the estimation occurs with a comparison of the specific $CO_2$ emission and energy consumption among the three cement plants analysed, resulting similar values for all the facilities (Table 3.5).

Table 3.5. Comparison of the $CO_2$ emission, fuel and electricity consumption specific to the annual production among the three cement plants considered in this study.

| Plant | $CO_2$ emission [$kt_{CO2}/t_{CEMENT}$] | Total fuel consumption [$TJ_{FUEL}/ t_{CEMENT}$] | Electricity consumption [$MWh_{EL}/ t_{CEMENT}$] |
|---|---|---|---|
| CE01 | 0.585 | 2.768 | 0.097 |
| CE02 | 0.622 | 2.631 | 0.097 |
| CE03 | 0.626 | 2.728 | 0.100 |

A comparative analysis can also be applied to the monthly distribution of the operative hours among the three cement industries analysed (Table 3.6) resulting a strongly case-specific behaviour, with the only common feature being the interruption, or a substantial reduction, of the cement production for at least one month per year. The annual operative hours are higher for CE02 with respect to the other facilities, making this plant the first cement producer in the studied region, despite the lower nominal capacity.

Table 3.6. Monthly distribution of the operative hours and annual cumulated value for the cement plants nodes CE01, CE02 and CE03.

| Plant | Jan | Feb | Mar | Apr | May | Jun | Jul | Aug | Sep | Oct | Nov | Dec | Total |
|---|---|---|---|---|---|---|---|---|---|---|---|---|---|
| CE01 | 199 | 657 | 248 | 0 | 688 | 682 | 182 | 71 | 719 | 308 | 404 | 0 | 4’157 |
| CE02 | 14 | 616 | 699 | 719 | 722 | 530 | 730 | 658 | 680 | 359 | 710 | 744 | 7’180 |
| CE03 | 0 | 60 | 713 | 716 | 731 | 471 | 741 | 421 | 0 | 500 | 716 | 108 | 5’177 |

The only steel industry considered in this study is sited in Taranto (TA) and owned by Acciaierie d’Italia S.p.A., with an estimated nominal capacity of around 4.6 $Mt_{STEEL}/y$, making this plant one of the largest steel industry in Europe [66]. The main production process occurring in the facility receives in input iron ore, limestone, steel scrap and energy [67]. The raw materials are used to provide the metallic charge, that is then melted and chemically reduced by using a fuel, typically coal. Steel represents the main output of the process, while other secondary gaseous flows are generated as by-products. These steel gases are then exploited, along with natural gas, in the thermoelectric power plants integrated in the site, consisting of a 480 MW Rankine cycle and a 564 MW gas-turbine cogeneration cycle [68], providing steam and electricity to the industrial process. The operation of the thermoelectric power plants is exhaustively described in literature [68], reporting, along with the electricity generated, a $CO_2$ production of 4.7 $Mt_{CO2}/y$ and an overall electrical efficiency of 35.9%. On the other hand, few information is available for what concerns the steel industry, for which are provided the electricity consumption [61], the $CO_2$ emission [11], equal to 6.1 $Mt_{CO2}/y$, and the operative hours [69] (8’200 h/y). The remaining parameters are estimated through the introduction of some assumptions, based on the average operation of the worldwide steel industry sector. In detail, IEA [67] provides the direct $CO_2$ emission specific to one tonne of steel produced (around 1.4 $t_{CO2}/t_{STEEL}$), from which the annual production of the facility can be estimated, resulting close to the 4,5 $Mt_{STEEL}/y$ value cited in literature [70]. Moreover, the coal consumption related to the production process can be estimated from the direct emissions through a stoichiometric analysis. The last assessment required for the input/output analysis applied on such node regards the interaction between the steel industry and the electricity grid. In 2018, the node exported 85.8 $GWh_{EL}$ to the external grid, only the 2.6% of the overall electricity generated by the integrated power plants, therefore it is required to analyse the trend of this electricity exportation in the recent years. In the period 2016-2018, for which the electricity generation data are available in literature, results a non-constant trend [61] [68] (

Table 3.7), with a tendency in the last two years to export electricity to the grid, due to a reduction in the energy consumption, with respect to the generation. This decrease in the activity of the steel plant, mostly due to the huge environmental impact [71], is likely to persist in the near future, therefore this node can be considered as an electricity exporter.

Table 3.7. Electricity generated and consumed by the steel industry node ST01 in the period 2016-2018 [61].

| Year | Electricity generated [$GWh_{EL}$/y] | Electricity consumed [$GWh_{EL}$/y] | Electricity exported [$GWh_{EL}$/y] |
|---|---|---|---|
| 2016 | 3’560 | 3’729 | -168.70 |
| 2017 | 3’378 | 3’338 | 40.85 |
| 2018 | 3’275 | 3’190 | 85.80 |

The node FR01 represents the only fuel refinery in the studied region, located in the same industrial area of the steel industry ST01, in Taranto, and owned by ENI power. A multitude of chemical processes occur in this facility, turning the crude oil received in input into refined fuels. A portion of the final product is then fed to the integrated gas turbine combined cycle, with a nominal power of 307 $MW_{EL}$ [72], covering almost the entire energy demand of the refinery. The operation of the facility is fully described in literature [73], providing a nominal annual capacity of 6.5 $Mt_{FUELS}$/y, a value of annual operative hours of 7,968 h/y, and all the other data reported in Table 3.4. For what concerns the $CO_2$ emitted by the facility [11], a major contribution is provided by the thermoelectric power plant, determining an annual emission of 0.82 $Mt_{CO2}$/y, against the 0.30 $Mt_{CO2}$/y produced directly by the chemical processes occurring in the fuel refinery. Differently from the steel industry, the FR01 node acted in 2018 as an electricity consumer, and this behaviour is also confirmed with the analysis of the interaction between the node and the electricity grid in the period 2016-2018 [61] [73] (Table 3.8), with the fuel refinery always importing electricity from the external grid.

Table 3.8. Electricity generated and consumed by the fuel refinery node FR01 in the period 2016-2018 [61] [73].

| Year | Electricity generated [$GWh_{EL}$/y] | Electricity consumed [$GWh_{EL}$/y] | Electricity exported [$GWh_{EL}$/y] |
|---|---|---|---|
| 2016 | 323 | 372 | -49 |
| 2017 | 358 | 330 | -72 |
| 2018 | 300 | 327 | -27 |

The industrial nodes set is completed with the CH01 facility, representing the only chemical industry included in this study. The main process occurring in the plant determines a raw fuel consumption, mainly virgin naphtha and LPG [74], for the production of a multitude of chemical final products, among which ethylene, polyethylene and butadiene [75]. This production process also generates superheated steam, that is then expanded in the thermoelectric power plant PP04 [76], sited in the same industrial area, generating electricity. Although the generation occurs in the NGCC plant, the contribution of the steam generated in the chemical industry is considered as an output of the node CH01, since the production is strictly related to the activity of the chemical plant. The nominal annual production capacity is reported as 2.3 $Mt_{PROD}/y$ [77], and all the other operative parameters shown in Table 3.4 are available in literature, except for the electricity consumption, that is assumed as equal to the value reported for the overall chemical sector in the Province of Brindisi [61]. The electricity generated in synergy with the thermoelectric power plant PP04 is estimated from the thermodynamic properties of the steam produced, reported as 1.24 $Mt_{H2O}/y$ at 130 bar and 520°C, and assuming a condenser temperature of 36°C [76]. The related enthalpic difference is computed by applying the IAPWS correlations, assuming a steam turbine efficiency of 0.85.

The monthly distribution of the nodes ST01, FR01 and CH01 production is not available in literature, therefore the operative hours are distributed along the months proportionally to the number of days, considering a constant production load for each plant.

### 3.3.2 Thermoelectric power plants

Fossil fuels are the main energy sources applied for energy generation in studied area, accounting for four NGCCs, being PP01, PP02, PP03 and PP04, and one coal-fuelled thermoelectric power plant PP05. The marked difference in the number of active facilities between the two plant typologies is strongly reduced for what concerns the nominal capacity installed, with the four NGCCs accounting for a cumulated value of 2'884 $MW_{EL}$ and the coal-fed plant characterised by a nominal capacity of 2'620 $MW_{EL}$. The proposed infrastructure interacts differently with the natural gas-based plants and the coal-fed one. For what concerns NGCC nodes, the cycle receives in input natural gas from external sources, and eventually hydrogen produced by the infrastructure. The main outputs determined by the production process consists in $CO_2$, eventually sequestered with the introduction of a post-combustion capture section, electricity, generated accordingly to the demand profile of the studied region, and hydrogen. In NGCC nodes, $H_2$ can be produced by integrating the combined cycle with a SMR, feeding the electricity generation process occurring in the node or the HSC designed by the infrastructure. Another approach is instead applied for the coal-power plant, difficultly adaptable for partially operating with hydrogen. This node is considered analogously to the industrial facilities, with a production

rate determined by the optimisation algorithm, that can eventually install a carbon capture section. Differently from the industrial nodes, the operation of the coal-fed power plant is not limited by a monthly demand constraint, therefore the production of such plant is determined by the electricity demand of the studied area.

The results of the input/output analysis applied to the thermoelectric power plants are provided in Table 3.9, with the same hypothesis and structure introduced for Table 3.4. Although for the majority of the plants a portion of the thermal input is obtained from the combustion of diesel or fuel gas, these parameters are not explicated in the table, since their contribution is negligible with respect to coal or natural gas ones.

Table 3.9. $CO_2$ emission, fuel consumption, nominal capacity, electricity generated and electrical efficiency of the power plants considered in this study.

| Parameter | | PP01 | PP02 | PP03 | PP04 | PP05 |
|---|---|---|---|---|---|---|
| $CO_2$ emission | [$kt_{CO2}$/y] | 637 | 521 | 320 | 2’433 | 5’477 |
| Natural gas | [$kt_{NG}$/y] | 222 | 189 | 110 | 876* | 0 |
| Coal | [$kt_{COAL}$/y] | 0 | 0 | 0 | 0 | 2’442* |
| Nominal capacity | [$MW_{EL}$] | 403 | 360 | 800 | 1’321 | 2’620 |
| Electricity generated | [$GWh_{EL}$/y] | 1’656 | 1’244 | 796 | 5’877 | 5’368 |
| Electrical efficiency | [%] | 58.0 | 51.2 | 56.4 | 49.3 | 29.9 |

The natural gas-fed thermoelectric power plants are distributed in the studied area as follows. Two NGCCs, PP01 and PP02, are located in the Province of Foggia, respectively in San Severo and Candela. The remaining capacity is installed in Modugno (BA) and Brindisi (BR), corresponding to the nodes PP03 and PP04. The majority of the information regarding the operation of the four power plants is provided by the environmental assessment report published by the owners, being Alpiq Energia for PP01 [78], Edison for PP02 [79], Sorgenia for PP03 [80] and Enipower for PP04 [76]. However, an additional analysis is required for the PP04 node since the operative parameters available in literature only refer to the year 2019, except for the net electricity and steam generated, also provided for the year 2018. The assessment of the 2018 values occurs neglecting the time dependency of the $CO_2$ emission and fuel consumption specific to the steam and electricity generated, maintained constant in the period 2018-2019, resulting a $CO_2$ emission very close to the value of 2’428 $Mt_{CO2}$/y reported in the EEA database [11]. The data obtained from this analysis refer to the total electricity output of the plant, including the electricity

generated from the steam received from the chemical industry, therefore the values are updated by removing this contribute, resulting an electrical efficiency reduction from 53.0% to 49.5%. The completeness of the input/output analysis applied to the NGCCs is assessed with a comparison between the resulting overall natural gas consumption (1.3 $Mt_{NG}/y$) to the value reported by the Italian Ministry of Economic Development (MiSE) [48] (1.5 $Mt_{NG}/y$). The relatively small difference between the two values can be due to the small-scale natural gas-fuelled plants, not included in this study, and to the conversion among the different units of measurement used in the references available in literature.

The only coal-fuelled thermoelectric power plant still active in the studied region is the "Federico II" plant, sited in Brindisi (BR) and owned by ENEL. Electricity is generated through a sub-critical water Ranking cycle [50] in four different modules, each one with a nominal power of 605 $MW_{EL}$, fed with coal and, in a minor part, with diesel. The low conversion efficiency, around 29.9%, and the high amount of $CO_2$ produced in the coal combustion process determined a decrease in the exploitation of the power plant, that in 2018 mainly operated with no more than two out of four modules [50]. The data directly provided by ENEL on the plant operation regard the efficiency and electricity generation in 2018 and 2019 [50], and the fuel consumption in 2019 [81]. Additional information is provided by the EEA database [11], reporting the total $CO_2$ emitted by the plant in 2018 and the operative hours for the same year, accounting for 4'269 h/y. The only missing parameter consists in the coal consumption of the node PP05, computed considering, along the period 2018-2019, a constant value of fuel consumption specific to the electricity generated, analogously to PP04. The same parameter can be computed from the $CO_2$ emission, resulting a coal consumption of 2.49 $Mt_{CO2}/y$, close to the value reported in Table 3.9.

### 3.3.3 Consumption and export nodes

Consumption and export nodes account for the energy demand of the studied area not related to large-size $CO_2$ emission sources, mostly related to residential utilities and small-scale industries and thermoelectric power plants. This energy requirement is modelled by distinguishing the contribution of each province, in terms of natural gas and electricity demand, and the other Italian region importing electricity from the studied area. Each consumption node is located approximately in the central point of the corresponding province, being Foggia for CN01, Barletta for CN02, Bari for CN03, Matera for CN04, Brindisi for CN05, Taranto for CN06 and Lecce for CN07. The only export node EN01, instead, is located outside the studied region border, representing the overall electricity exported to the other Italian regions. Since in 2018 the majority of the electricity exported by the Southern Italy bidding zone, comprehensive of Puglia, Basilicata, Molise and

Calabria regions (Figure 3.5), was delivered to the Centre-South zone [82], the export node is located in Campania region, close to the Puglia region border.

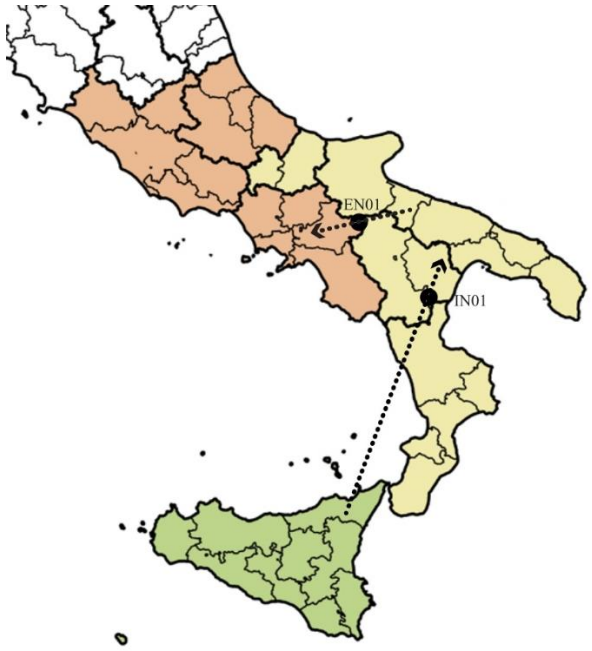


Figure 3.5. Geographical representation of the Italian electricity market bidding zones of Southern Italy, Centre-Southern Italy and Sicily, along with the position of the electricity import and export nodes and the direction of the electricity flows exchanged among the three bidding zones considered

The infrastructure must satisfy the electricity demand of such nodes at each hour of the year, therefore the input/output analysis is applied for assessing the hourly profile of the annual electricity consumption of each province. Moreover, to these nodes is associated a natural gas demand, that can be partially substituted with hydrogen. The amount of $H_2$ delivered to the consumption nodes represents a degree of freedom for the optimisation algorithm, limited by the thermal input required for each node at each timestep. Another goal of the input/output analysis, then, is the assessment of the annual natural gas consumption of each province, along with the hourly distribution. The export node is modelled in the infrastructure as an electricity consumer, operating at each hour of the year analogously to the consumption nodes.

The main results of the input/output analysis applied to consumption and export nodes are reported, for what concerns the annual $CO_2$ emission and energy demand, in Table 3.10, along with the electricity (Figure 3.6) and natural gas consumption (Figure 3.7) hourly distribution.

Table 3.10. $CO_2$ emission, natural gas and energy demand for each consumption and electricity export node.

| Node | Area represented | $CO_2$ emission [$kt_{CO2}/y$] | Electricity demand [$GWh_{EL}/y$] | Natural gas demand [$kt_{NG}/y$] |
|---|---|---|---|---|
| CN01 | Province of Foggia | 314 | 1'841 | 124 |
| CN02 | Province of Barletta | 199 | 965 | 79 |
| CN03 | Province of Bari | 635 | 4'097 | 252 |
| CN04 | Province of Matera | 126 | 599 | 50 |
| CN05 | Province of Brindisi | 199 | 1'195 | 79 |
| CN06 | Province of Taranto | 292 | 1'664 | 116 |
| CN07 | Province of Lecce | 404 | 2'167 | 161 |
| EN01 | Rest of Italy | - | 11'201 | - |

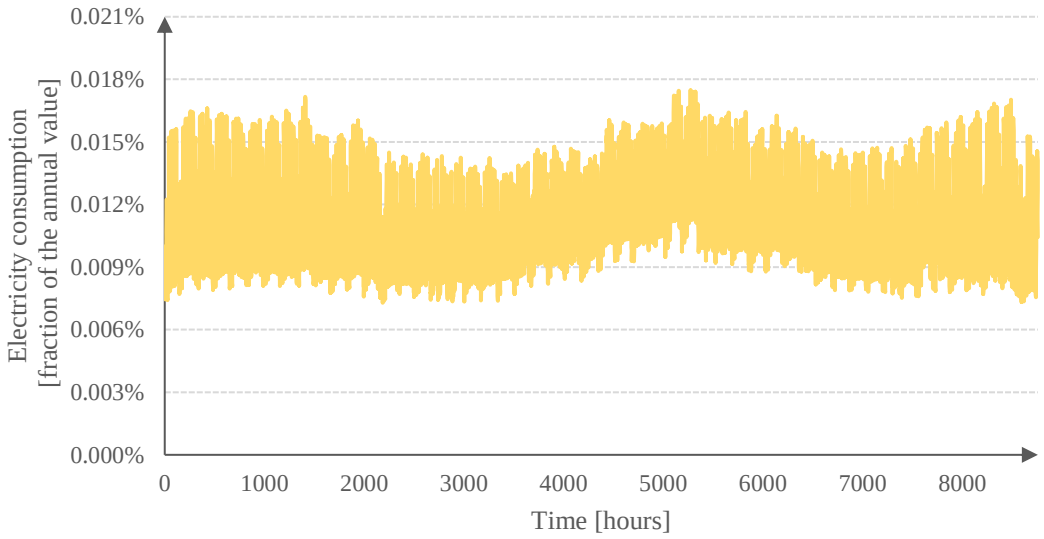


Figure 3.6. Electricity consumption in the year 2018, expressed as the fraction of the annual value consumed at each hour of the year.

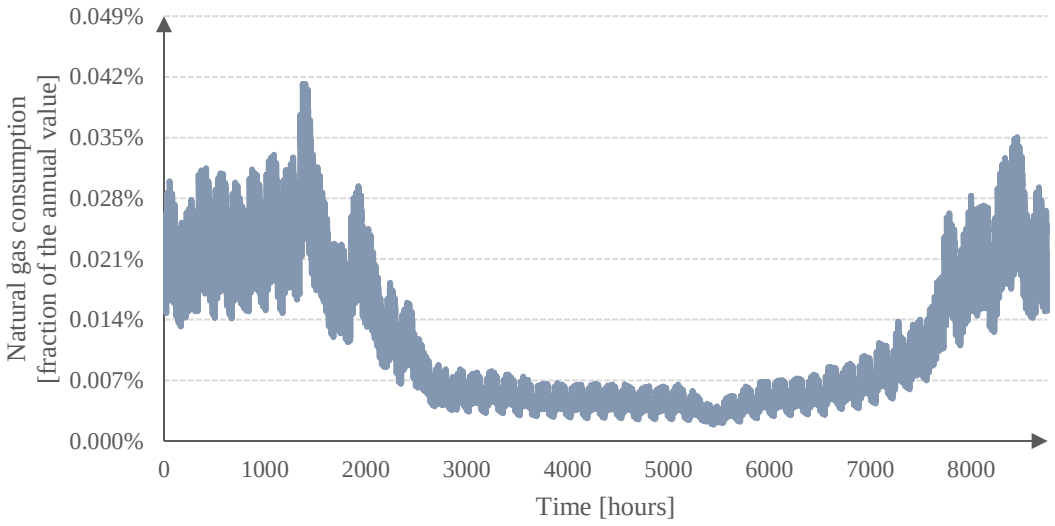


Figure 3.7. Natural gas consumption in the year 2018, expressed as the fraction of the annual value consumed at each hour of the year.

The annual electricity consumption is provided for each province by Terna, the Italian TSO for the electricity grid [61] [83]. From these values is then removed the contribution of the energy-intensive industries already included in the nodes set, obtaining the results provided in Table 3.10. The electricity exported towards the other Italian regions is instead computed as the difference between the electricity generated in the studied area, including the RES contribution, discussed in the next subsection, and the total electricity consumption. For what concerns the hourly distribution of the annual energy demand, the values specific to each province are not available in literature, therefore a common distribution for all the consumption and export nodes is introduced. Such values are computed from the hourly electricity consumption of the Southern Italy bidding zone, provided by the Italian energy market administrator (GME) [84]. The annual electricity consumption for such area, computed as the sum of the hourly value, is close to the one reported by Terna, obtaining an error of 7.6%. The distribution of the annual electricity consumption (Figure 3.6) is than computed for each hour as the ratio between the correspondent electricity consumption and the annual cumulated value.

The natural gas demand of each consumption node is estimated starting from the value reported by MiSE [48], referred to the fuel delivered by the transportation grid, excluding the contribution of large industries and power plants, for Puglia (1'135 $MSm^3/y$) and Basilicata (199 $MSm^3/y$) regions. From these values are then computed the natural gas consumed in each province and the hourly distribution of the annual data, although for both the estimation it is necessary to assume the natural gas demand as requested only by the residential utilities, therefore neglecting the contribution of small-sized industries and thermoelectric power plants. Provided this simplification, the regional fuel consumptions are allocated to each province proportionally to the population at the 1$^{st}$ January 2019 [85],

resulting the values provided in Table 3.10. Due to the lack of information regarding the hourly natural gas consumption profile in each province of the region analysed, this parameter is assumed as equal to the national one. The values related to the Italian natural gas consumption are provided by Snam [86], under the voice "Deliveries to distribution systems and other national TSOs interconnections", providing the total demand not related to large industries and power plants directly connected to the transmission grid. However, the sum of the values reported in the database is one order of magnitude higher than the actual demand of this sector, provided by MiSE [48]. This huge difference is probably due to a misinterpretation of the data provided by Snam: the values reported do not represent the hourly natural gas consumption, since they lack a marked difference between daily and night hours, instead they probably correspond to the estimation for each hour of the daily demand for the fuel. Hence, in order to extract from the data available a reliable hourly distribution of the natural gas consumption, the correlation provided in Eq.(3.1) is proposed. The parameter $Q_{h,d}^{NG}$ [$t_{NG}$/h] represents the natural gas consumption at the hour *h* of the day *d*, proportional to the average of the values reported by Snam for day *d* ($Q_h^{NG,AV}$, [$t_{NG}$/d]) and to the fraction of the daily fuel consumption at the hour *h* ($distr_{h,d}^{NG}$).

$$Q_{h,d}^{NG} = Q_h^{NG,AV} \cdot distr_{h,d}^{NG} \tag{3.1}$$

The parameter $distr_{h,d}^{NG}$ is introduced according to a study conducted as master's degree thesis at Politecnico di Torino [87], providing an average daily distribution of the natural gas consumption for Turin, sited in Northern Italy (Figure 3.8).

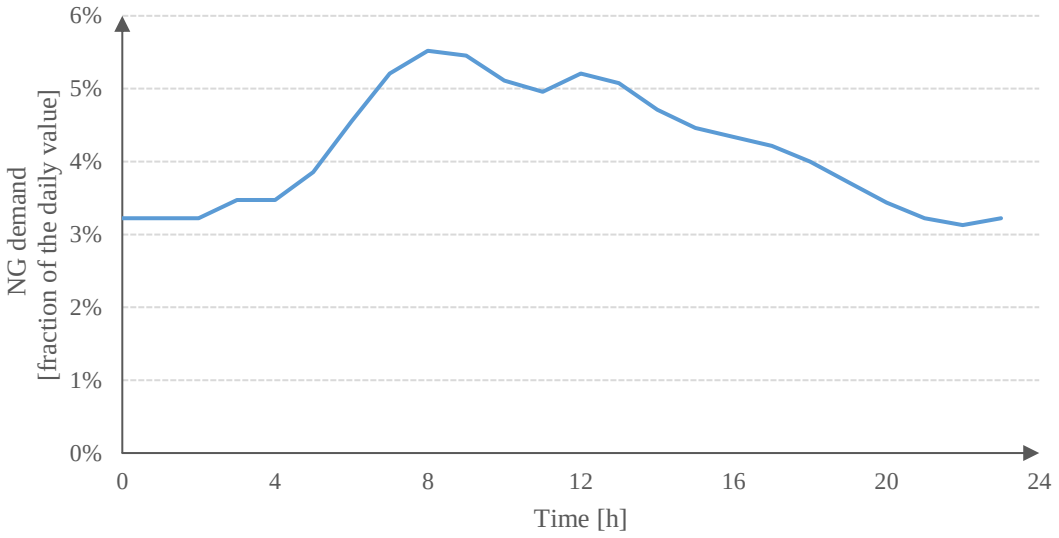


Figure 3.8. Average hourly distribution of the daily natural gas consumption from residential utilities in Turin [87]

The introduction of this model, however, leads to several approximations, regarding the temporal and spatial scale and the sector to which the model is applied. In particular, the natural gas distribution in Turin for a non-specified day is here considered as valid for the

whole country at each day of the year. Moreover, it has to be taken into account that the distribution system delivers gas not only to residential utilities, but a non-negligible fraction is sent to small-sized industries and power plants. Despite all these assumptions, the result obtained with this model (Figure 3.9) is close to the profile proposed in the work conducted by Colbertaldo et al. [25], referred to the Italian natural gas consumption for non-power uses in 2018. Moreover, the cumulated annual demand obtained is close to the one provided by MiSE, with an error equal to 5.9%.

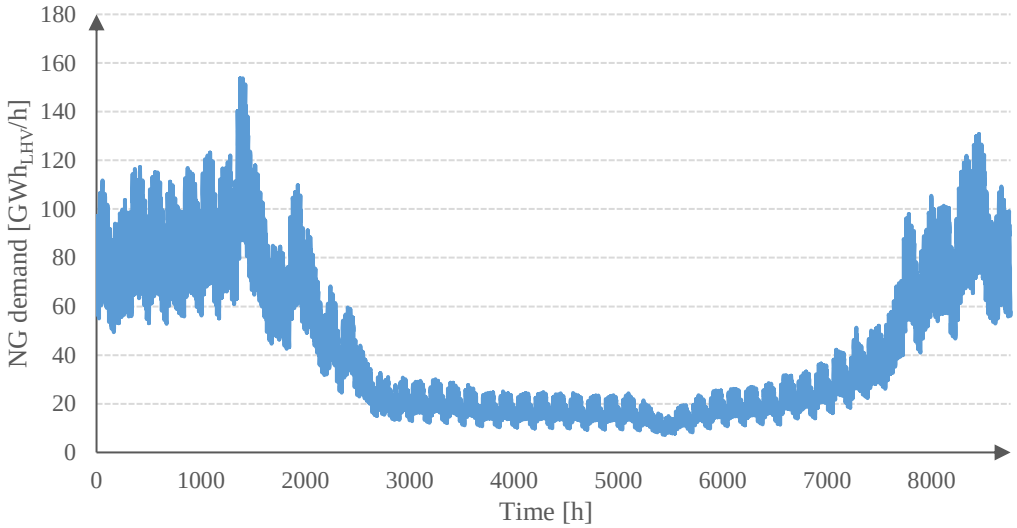


Figure 3.9. Hourly distribution of the natural gas delivered from the distribution grid proposed in this model

### 3.3.4 Production and import nodes

Production nodes are introduced accounting for the electricity generation from RES in each province, in detail wind power and solar PV. The geographical location of such nodes coincides with the consumption nodes ones, being both the node typologies representative of the same areas. Due to the electricity generation from RES, production nodes are included in the infrastructure as electricity providers to the grid. The optimisation algorithm cannot control the hourly production from these sources, being not-dispatchable, although a degree of freedom is represented by the nominal capacity installed, that can be optionally incremented. Moreover, such nodes are suitable for green hydrogen production, thanks to the possibility to install an electrolyser exploiting renewable electricity as energy source. The import node accounts, instead, for the electricity imported from other Italian regions. Analogously to the export node, the electricity import point is located according to the electricity flow averagely exchanged by the Southern Italy bidding zone. In detail, in 2018 such area imported electricity only from Sicily, therefore the import node is placed outside the studied area border, along the direction of the imported electricity flow [82]. Although in 2018 the studied region globally exported electricity towards the rest of Italy,

the introduction of the export node is necessary for allowing the infrastructure to always satisfy the electricity demand of the area, exploiting the imported electricity as a dispatchable energy source. The main results of the input/output analysis applied to the production nodes is provided in Table 3.11, reporting for each region the nominal power installed and the annual electricity generated by wind power and solar PV. The hourly distribution of the two sources availability is also provided (Figure 3.10 and Figure 3.11).

Table 3.11. Capacity installed and annual electricity generation from solar PV and wind power for each province considered in this study.

| | | Solar PV | | Wind power | |
|---|---|---|---|---|---|
| Node | Province | Capacity installed [$MW_{EL}$] | Electricity generation [$GWh_{EL}/y$] | Capacity installed [$MW_{EL}$] | Electricity generation [$GWh_{EL}/y$] |
| PN01 | Foggia | 423 | 541 | 2064 | 3686 |
| PN02 | Barletta | 181 | 217 | 113 | 179 |
| PN03 | Bari | 483 | 604 | 72 | 139 |
| PN04 | Matera | 181 | 220 | 288 | 599 |
| PN05 | Brindisi | 503 | 663 | 62 | 99 |
| PN06 | Taranto | 383 | 468 | 124 | 282 |
| PN07 | Lecce | 704 | 875 | 93 | 165 |

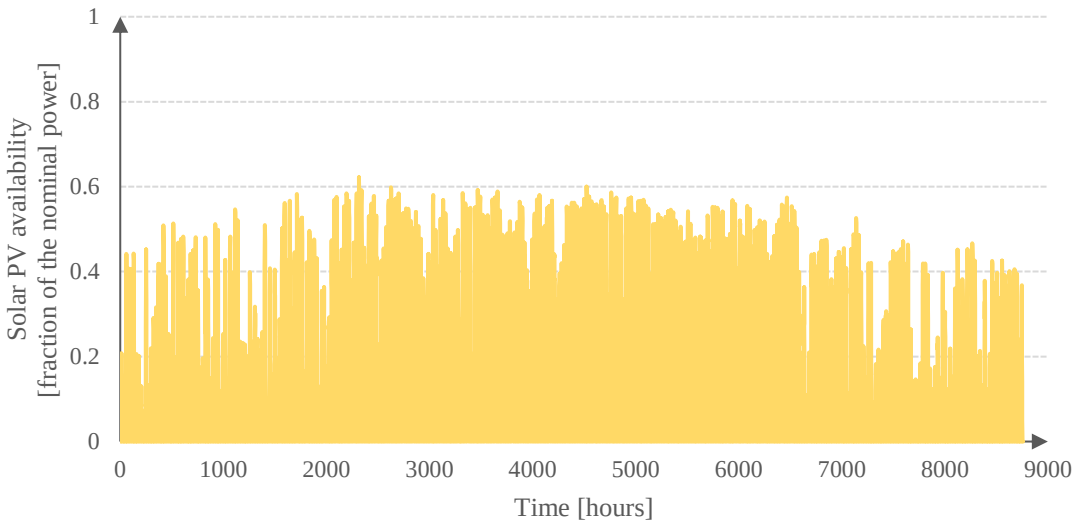


Figure 3.10. Solar PV hourly availability, expressed as the ratio between the electricity generated at each hour and the nominal capacity installed.

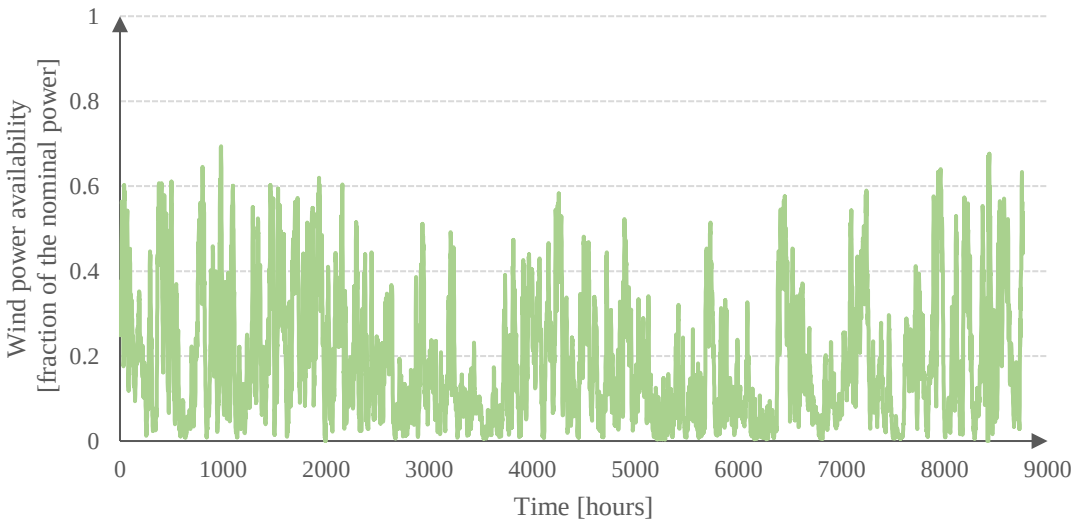


Figure 3.11. Wind power hourly availability, expressed as the ratio between the electricity generated at each hour and the nominal capacity installed.

The RES capacity installed in each province is provided by the Italian energy services administrator (GSE) [88] [89], while the electricity generation values are reported by Terna [49]. Since the only available information on the energy generation in each province is referred to the gross value, while the net electricity output is only provided on a regional scale, the net electricity generation is computed, for each province, by scaling the gross values in order to obtain the net regional energy generation reported in literature. Analogously with the electricity consumption, the hourly generation from solar PV and wind power in each province is not provided in literature, therefore a common distribution is introduced, basing on the values referred to the Southern Italy bidding zone available in literature [90]. The accuracy of such values is computed with a comparison between the cumulated value of the generation profiles and the annual electricity generation reported, for each energy source, by Terna [49], obtain errors of 8% and 13% for, respectively, wind power and solar PV.

Once defined all the energy sources considered in this study, the completeness of the data collected is confirmed by comparing the modelled annual electricity generated in Puglia region with the value reported in literature (28,5 $TWh_{EL}/y$) [49], obtaining an error of 3%.

Production nodes are suitable for green hydrogen production, that is then delivered to consumption nodes or NGCCs. Since PNs and CNs are geographically coincident, the hydrogen exchange among such nodes requires the introduction of an equivalent diameter of the province (3.2), depending on the province diameter $p$ and surface $S$ [91] (Table 3.12), accounting for the $H_2$ distribution along the region.

$$d_{EQ} = 4 \cdot \frac{p}{S} \tag{3.2}$$

Table 3.12. Land perimeter, land surface and equivalent diameter of each province considered in this study

| Province | Perimeter [km] | Surface [$km^2$] | Equivalent diameter [km] |
|---|---|---|---|
| Foggia | 545 | 7'007 | 51 |
| Barletta | 276 | 1'543 | 22 |
| Bari | 470 | 3'863 | 33 |
| Matera | 402 | 3'479 | 35 |
| Brindisi | 323 | 1'861 | 23 |
| Taranto | 419 | 2'467 | 24 |
| Lecce | 361 | 2'799 | 31 |

### 3.3.5 $CO_2$ storage sites

In order to reduce the $CO_2$ emission determined by the industry and thermoelectric power plant nodes, the infrastructure relies, along with the other mitigation strategies, on CCS technologies, for which is required to assess the $CO_2$ storage potential available in proximity to the studied area. In detail, this analysis refers to the work conducted by Donda et al. [37], providing the location (Figure 3.12) and performance analysis (Table 3.13) of 14 deep saline aquifers, distributed along all the Italian peninsula, potentially suitable for $CO_2$ storage. In addition, the infrastructure includes another node corresponding to the North Sea, whose huge storage potential [32] prevents the storage availability from limiting the CCS penetration in the infrastructure.

Table 3.13. Land surface, maximum and minimum $CO_2$ storage capacity of each $CO_2$ storage site included in this study.

| Node | Site | Land surface [$km^2$] | Minimum capacity [$Mt_{CO2}$] | Maximum capacity [$Mt_{CO2}$] |
|---|---|---|---|---|
| CS01 | North Sea | - | 16'000 | 16'000 |
| CS02 | Lombardia 1 | 740 | 38 | 76 |
| CS03 | Lombardia 2 | 615 | 178 | 356 |
| CS04 | Emilia 1 | 560 | 246 | 492 |
| CS05 | Emilia mare | 715 | 657 | 1'314 |
| CS06 | Marche 1 | 615 | 358 | 716 |
| CS07 | Abruzzo 1 | 175 | 23 | 46 |
| CS08 | Abruzzo mare | 1800 | 650 | 1'300 |
| CS09 | Abruzzo 2 | 340 | 40 | 80 |
| CS10 | Abruzzo 3 | 64 | 15 | 30 |
| CS11 | Molise 1 | 45 | 16 | 32 |
| CS12 | Molise 2 | 155 | 70 | 140 |
| CS13 | Brandanica | 520 | 344 | 688 |
| CS14 | Calabria ionica | 320 | 210 | 420 |
| CS15 | Sicilia 1 | 465 | 103 | 206 |


Figure 3.12. Location of the $CO_2$ storage sites included in this study. The North Sea storage site CS01 is not represented with the actual geographical position, due to the distance between this node and the studied region.

The more accessible sites in terms of geographical position for the studied region are the ones sited in southern Italy and on the Adriatic coast, while the economic feasibility of the exploitation of the other sites will be assessed in the optimisation phase. Donda et al. [37] evaluated the amount of $CO_2$ storable in the saline aquifers by assuming two values, of 1% and 4%, for the storage efficiency factor, defined as the fraction of the total pore volume of the rock that can be filled by the fluid. The minimum capacity reported in Table 3.13 are obtained with the 1% value, while the maximum capacity is computed considering a storage efficiency factor of 2%, since the 4% value considered in the reference leads to a too optimistic result in terms of storage potential.

### 3.3.6 Ports

The distance between the studied region and the CS01 node make ship transportation the more economic advantageous modality for this connection, therefore it is required to identify the ports sited in the region suitable for this route. Puglia region provides three main ports [92] in Bari, Brindisi and Taranto, although only the last one is included in the

nodes set, being the largest one in terms of transport capacity (17,6 $Mt_{CO2}/y$) [92] and currently connected with the port of Rotterdam, sited on the North Sea coast [93], with a route length of 2'954 nautical miles, corresponding to 5'471 km [94]. The importance of this connection relies on the central role of the Port of Rotterdam in the CCS diffusion in Europe, as provided by a project proposed by the European Union [95], aiming at developing within 2'024 a $CO_2$ transportation infrastructure connecting this port with the geological $CO_2$ storage sites located in the North Sea.

### 3.3.7 Transit and offshore nodes

Transit and offshore nodes are introduced in the infrastructure for facilitating the mass exchanges between the other nodes. Their contribution in the mass balances only consists in delivering the same flow rate received in input, without being associated to any source or sink term. Only one transit node TN01 is included in the infrastructure, for connecting the $CO_2$ storage sites CS14 and CS15: without TN01, such connection would occur with an offshore pipe, therefore with a higher unitary transportation cost. Because of the introduction of TN01 and the limit distance constraint for direct nodal connections, the only offshore area in which a pipeline could be installed is the Gulf of Taranto, in the Ionian Sea. Such area is represented with an offshore node ON01, contributing to the mass balance analogously to TN01. To all the $CO_2$ transportation pipelines connected to ON01 is associated a higher installation cost, as discussed in Chapter 4.

# Chapter 4
# Mathematical model

The installation and operation of the infrastructure is optimised with a mathematical model, presented as a mixed integer linear programming (MILP) problem. The platform chosen for the algorithm implementation is MATLAB, relying on the Yalmip libraries for the definition of the variables and the constraints, and on Gurobi for the problem optimisation. The formulation of the mathematical model is based on the definition of a set of continuous or integer decision variables, through which the optimisation algorithm controls the installation and operation of the infrastructure alongside the mitigation strategies considered in this study (CCS, HSC and RES). The value of such variables is computed according to an objective function, consisting in the total infrastructure cost minimisation. The degrees of freedom available for the algorithm are limited with a set of constraints, related to physical limits, such as mass and energy balances, or to the design choices applied to the infrastructure, for instance the satisfaction of the monthly and annual demand for each industrial node.

## 4.1 Temporal and spatial sets

The basis of the optimisation algorithm consists in the definition of the temporal and spatial dimension of the infrastructure, provided with a series of sets and subsets. The time set is composed by 8’760 hours composing the year. This element is then divided into 12 subsets representing the months (Table 4.1).

Table 4.1. Time subsets, representing the hours of the year composing each month

| Month | Subset | Range [hours] |
|---|---|---|
| January | M01 | 1 – 744 |
| February | M02 | 745 – 1’416 |
| March | M03 | 1’417 – 2’160 |
| April | M04 | 2’161 – 2’880 |
| May | M05 | 2’881 – 3’624 |
| June | M06 | 3’625 – 4’344 |
| July | M07 | 4’345 – 5’088 |
| August | M08 | 5’089 – 5’832 |
| September | M09 | 5’833 – 6’522 |
| October | M10 | 6’533 – 7’296 |
| November | M11 | 7’297 – 8’016 |
| December | M12 | 8’017 – 8’760 |

For what concerns the spatial scale, to each node is assigned a number, that is then included in the nodes set. Similarly to the previous case, the main set is divided into different subsets (Table 4.2) representing the different types of nodes, in turn classified into sub-subsets, distinguishing elements of the same subset interacting differently with the infrastructure.

Table 4.2. Space subsets and sub-subsets, representing the different nodes typologies considered in this study. For what concerns $CO_2$ storage sites, the sub-subsets are introduced for distinguishing the nodes connected via ship (CS_S) and via pipe (CS_P)

| Node type | Subset | Sub-subset | Range |
|---|---|---|---|
| Industry | IND | - | 1 – 6 |
| NGCC | PP | NGCC | 7 – 10 |
| Coal power plant | PP | CPP | 11 |
| Consumption node | CN | - | 12 – 18 |
| Export node | EN | - | 19 |
| Production node | PN | - | 20 - 26 |
| Import node | IN | - | 27 |
| North Sea site | CS | CS_S | 28 |
| Other $CO_2$ storage sites | CS | CS_P | 29 - 42 |
| Port | PO | - | 43 |
| Transit node | TN | - | 44 |
| Offshore node | ON | - | 45 |

Once defined the nodes included in the infrastructure, it is crucial to describe the geographical disposition of such elements. Starting from the latitude and longitude values, previously obtained from Google Maps [96], it is possible to determine the linear distances between the nodes by applying the spherical law of cosines (4.1) [97], in which $n$ and $n_p$ are two generic nodes, $r_{EARTH}$ = 6'373 km is the Earth radius, and *lat* [rad] and *long* [rad] are respectively the latitude and longitude of the nodes.

$$LD_{n,n'}=r_{EARTH}\cdot acos\,[\,sin\,(lat_n)\cdot sin\,(lat_{n'})+cos\,(lat_n)\cdot cos\,(lat_{n'})\cdot cos(long_n-long_{n'})] \quad (4.1)$$

Comparing the values obtained with this method to the linear distances provided by Google Maps for a sample of nodes combination (Table 4.3) results a high accuracy of the model.

Table 4.3. Comparison between the nodal linear distance computed with the proposed model and with Google Maps

| n | n' | Model [km] | Google Maps [km] |
|---|---|---|---|
| 2 | 4 | 49.92 | 50.00 |
| 6 | 7 | 241.47 | 243.00 |
| 4 | 6 | 68.65 | 72.78 |
| 4 | 9 | 75.71 | 75.68 |
| 5 | 12 | 182.88 | 181.00 |

The topology of the infrastructure is represented with a node-line incidence matrix ($a^{N,L}$), composed of N rows, with N being the number of nodes, and NxN columns, corresponding to the number of lines. The elements included in such matrix assume value 1 if the line enters the node, -1 if exiting, and 0 if the line is not connected to the node. In the mass and energy balances, described in 4.3, the product between the incidence matrix and the variable representing the flow exchanged between the nodes provides the net flow entering a node. The construction of such matrix occurs according to the algorithm provided in Table 4.4.

Table 4.4. Algorithm for the node-line incidence matrix construction (MATLAB code)

```
a_n_l=sparse(N,N*N);
for i=1:N
    a_n_l(i,(i-1)*N+1:i*N)=ones(1,N);
    a_n_l(i,(i-1)*N+i)=0;
    if i>1
        a_n_l(1:i-1,(i-1)*N+1:(i-1)*N+i-1)=-diag(ones(1,i-1));
    end
    if i<N
        a_n_l(i+1:N,(i-1)*N+i+1:i*N)=-diag(ones(1,N-i));
    end
end
```

In detail, for each value of *i*, a 1xN ones vector is added to the $a^{N,L}$ matrix, representing the lines entering node *i*. Then, transportation loops are removed by assigning value 0 to the lines connected to only one node, and diagonal matrices, with value -1, are added above and below row *i*, accounting for the lines exiting from the node, in order to obtain a null sum for each column of the matrix. The output obtained from the application of such algorithm is reported in Table 4.5, with N=4.

Table 4.5. Result of the application of the algorithm described in Table 4.4 for the construction of a node-line incidence matrix with N=4. The first row and column represent, respectively, the row and column numbers.

| | 1 | 2 | 3 | 4 | 5 | 6 | 7 | 8 | 9 | 10 | 11 | 12 | 13 | 14 | 15 | 16 |
|---|---|---|---|---|---|---|---|---|---|---|---|---|---|---|---|---|
| 1 | 0 | 1 | 1 | 1 | -1 | 0 | 0 | 0 | -1 | 0 | 0 | 0 | -1 | 0 | 0 | 0 |
| 2 | 0 | -1 | 0 | 0 | 1 | 0 | 1 | 1 | 0 | -1 | 0 | 0 | 0 | -1 | 0 | 0 |
| 3 | 0 | 0 | -1 | 0 | 0 | 0 | -1 | 0 | 1 | 1 | 0 | 1 | 0 | 0 | -1 | 0 |
| 4 | 0 | 0 | 0 | -1 | 0 | 0 | 0 | -1 | 0 | 0 | 0 | -1 | 1 | 1 | 1 | 0 |

Since the proposed infrastructure includes 45 nodes, the huge dimension of the incidence matrix is reduced by removing the column corresponding to transportation loops and imposing a limit distance of 100 km, above which direct nodes connections are not allowed. The columns of the $a^{N,L}$ matrix lines corresponding to the lines exceeding such constraint are then removed, reducing the number of columns from 2'025 to 484. The limit distance introduced guarantees to not isolate any nodes from the grid, except for some $CO_2$ storage sites located far from the studied region. However, among such nodes, the ones sited in Italy can be manually connected to the infrastructure by restoring the lines connecting node CS02 with CS03 (entering node CS02), CS04 with CS05 (entering node CS04), TN01 with CS14 (entering node TN01) and CS15 with TN01 (entering node CS15). The only node still isolated from the infrastructure is the North Sea storage site. Since this node is connected to the port of Taranto via ship, this line differs from the ones occurring via pipe, in terms of transportation cost, therefore it remains excluded from the $a^{N,L}$ matrix, but still contributes to the total cost function and $CO_2$ balance, as discussed in the following sections.

## 4.2 Objective function

The objective of the optimisation algorithm is the minimisation of the annual total cost required for the installation and operation of the different elements composing the infrastructure. In detail, the total cost function ($TC$, [M€/y]) (4.2) is determined from the contributes of the CCS network ($TC^{CCS}$,), the HSC ($TC^{HSC}$,), the additional RES capacity installed in the area ($TC^{\mathrm{RES}}$), the cost related to the electricity imported from the other Italian regions ($TC^{\mathrm{ELC,IMP}}$) and the fuel consumed by the infrastructure ($TC^{FUEL}$).

$$TC = TC^{CCS} + TC^{HSC} + TC^{RES} + TC^{ELC,IMP} + TC^{FUEL} \tag{4.2}$$

### 4.2.1 Cost of the CCS network

The cost function of the CCS network (4.3) comprehends the contributions of the $CO_2$ capture ($TCC^{CCS}$), transportation ($TTC^{CCS}$) and storage ($TSC^{CCS}$) sections.

$$TC^{CCS} = TCC^{CCS} + TTC^{CCS} + TSC^{CCS} \quad (4.3)$$

The CCS network is modelled according to the work conducted by d'Amore et al. [31], which provides an economic and performance analysis of all the three steps included in the network design, i.e. capture, transport and storage of the $CO_2$.

The optimisation algorithm can install a $CO_2$ capture section on the industrial and thermoelectric power plants nodes. The performance and economic parameters of such technology (Table 4.6) depends on the industrial process occurring in the node from which $CO_2$ is removed.

Table 4.6. Performance and economic parameters of the different $CO_2$ capture modalities [31].

| Node type | $\eta_n^{CAPT}$ | $\rho_n^{CCS}$ | $CCA_n^{FIX,REF}$ | $CCA_n^{VAR}$ | $M_n^{CO2,CAPT,REF}$ |
|---|---|---|---|---|---|
| | - | - | [€/t] | [€/t] | [$Mt_{CO2}$/y] |
| Cement industry | 0.90 | 1.00 | 36.9 | 7.5 | 0.654 |
| Steel industry | 0.76 | 1.20 | 12.2 | 40.7 | 7.68 |
| Fuel refinery | 0.80 | 1.20 | 44.8 | 44.7 | 2.83 |
| NGCC | 0.90 | 1.00 | 49.8 | 20.3 | 1.51 |
| Coal power plant | 0.90 | 1.00 | 42.7 | 13.5 | 2.97 |

The capture section performance is quantified by two parameters, being the $CO_2$ capture efficiency ($\eta_n^{CAPT}$), defined as the ratio between the captured $CO_2$ and the one produced by the plant, and another parameter ($\rho_n^{CCS}$), accounting for the additional $CO_2$ production, with respect to the plant without CCS, due to the energy required for the $CO_2$ sequestration process. Among the industries included in the infrastructure, the only missing node typology in Table 4.6 is the chemical industry, for which in this work are adopted the same parameters of the fuel refinery. This choice is justified by the work conducted by Kuramochi et al. [98], in which the petrochemical industry is included in the same category of the fuel refinery. Moreover, among the multitude of processes that can occur in a chemical facility, the cited work refers to the ethylene production from naphtha and LPG, pointed as the main $CO_2$-emitting activity of the sector, which also represents the main production process, together with the polyethylene synthesis from the same raw fuels, of the chemical industry included in the infrastructure [77]. This performance similarity

among the application of CCS in the chemical industry and fuel refinery can be explained by the similar partial pressure of $CO_2$ in the exhaust gases of the production processes [99].

The economic parameters defined in Table 4.6 refer to the total capture cost structure expressed in Eq.(4.4), defined as a linear function in the continuous variable $M_{t,n}^{CO2,CAPT}$[$t_{CO2}$/h], expressing the $CO_2$ captured in node *n* at each time step *t*. The annual cumulated value of this variable is multiplied for the cost of $CO_2$ avoided, composed of a fixed ($CCA_n^{FIX}$, [€/$t_{CO2}$]) and a variable ($CCA_n^{VAR}$) term. The fixed component of the unitary cost is characterised by scale economies, therefore its value decreases for large-sized plants. Due to the heterogeneity of the industries considered, the scale is accounted as the ratio between the $CO_2$ that can be captured from the plant *n*, computed from the annual $CO_2$ emitted by the plant in 2018 ($M_n^{CO2,EM,BASE}$, [$t_{CO2}$/y]), and the $CO_2$ produced by the reference plant ($M_n^{CO2,CAPT,REF}$) (4.5).

$$TCC^{CCS} = \sum_n \left( (CCA_n^{FIX} + CCA_n^{VAR}) \cdot \sum_t Q_{t,n}^{CO2,CAPT} \right) \tag{4.4}$$

$$CCA_n^{FIX} = CCA_n^{FIX,REF} \cdot \left( \frac{M_n^{CO2,EM,BASE} \cdot \eta_n^{CAPT} \cdot \rho_n^{CCS}}{M_n^{CO2,CAPT,REF}} \right)^{-0.4} \tag{4.5}$$

After the capture section, the $CO_2$ is transported towards the storage sites, with a total transportation cost characterised by the contributes of the pipeline ($TTC^{CCS,PIPE}$) and the ship ($TTC^{CCS,SHIP}$) connections (4.6).

$$\mathrm{TTC}^{\mathrm{CCS}} = TTC^{CCS,PIPE} + TTC^{CCS,SHIP} \tag{4.6}$$

Analogously to the capture cost, pipeline transportation is characterised by scale economies. The cost function of this component (4.7) includes a unitary transportation cost ($UTC_{q,n,n'}^{PIPE}$, [€/km/$t_{CO2}$]) specific to the annual $CO_2$ exchanged between two nodes *n* and *n'* and to the distance covered by the pipe. The transport capacity is modelled with four ranges *q* (Table 4.7), to which different values of $UTC_{q,n,n'}^{PIPE}$ are assigned, depending on the maximum and minimum flow rate delivered by the pipe *q*.

$$TTC^{CCS,PIPE} = \sum_{n,n'} \left( LD_{n,n'} \cdot \Omega_{n,n'}^{OFFSHORE} \cdot \sum_q \left( UTC_{q,n,n'}^{PIPE} \cdot M_{q,n,n'}^{CO2,PIPE,NOM} \right) \right) \tag{4.7}$$

Table 4.7. Flow rate-based classification of the unitary cost required for $CO_2$ transportation via pipeline [31]

| Size | $M_{q,y}^{CO2,MIN}$ [$Mt_{CO2}/y$] | $M_{q,y}^{CO2,MAX}$ [$Mt_{CO2}/y$] | $UTC_{n,n'}^{PIPE}$ [€/km/$t_{CO2}$] | $\Omega_{n,n'}^{OFFSHORE}$ - |
|---|---|---|---|---|
| $q_1$ | 0.10 | 0.50 | 0.1218 | 2.0942 |
| $q_2$ | 0.50 | 1.00 | 0.0541 | 1.8481 |
| $q_3$ | 1.00 | 5.00 | 0.0292 | 1.6407 |
| $q_4$ | 5.00 | 50.00 | 0.0097 | 1.3385 |
| average | - | - | 0.0537 | 1.7304 |

Due to the high computational burden resulting for the model, the $CO_2$ flow rate discretisation is not considered in this study. The total pipeline cost is estimated assuming a unique value of $UTC_{n,n'}^{PIPE}$ and $\Omega_{n,n'}^{OFFSHORE}$, equal to the average values reported in Table 4.7.

The cost structure is then completed by multiplying the unitary cost for the variable $M_{q,n,n'}^{CO2,PIPE,NOM}$ [$t_{CO2}$/h], representing the maximum $CO_2$ exchanged between nodes *n* and *n'* with a pipeline *q*, for the linear distance between the nodes ($LD_{n,n'}$, [km]) and for a parameter $\Omega_{n,n'}^{OFFSHORE}$, equal to 1 if the pipeline is onshore or higher than 1 if the connection is offshore.

The evaluation of the parameter $\Omega_{n,n'}^{OFFSHORE}$ requires an additional analysis for establishing whether the pipeline considered is installed onshore or offshore. Due to the distance limit imposed for direct nodal connections, the only offshore lines are the ones crossing the Gulf of Taranto, in the Ionian Sea, discretised with an offshore node (latitude = 0.6944 rad; longitude = 0.3018 rad). Among the lines for which the distance limit constraint is satisfied, the ones connected to the offshore node are characterised by a higher transportation cost, since the parameter $\Omega_{n,n'}^{OFFSHORE}$ assumes value 1.7304, while for all the other connections $\Omega_{n,n'}^{OFFSHORE}$ is equal to 1.

For what concerns the ship transportation, the cost structure shown in Eq.(4.8) depends on the nautical distance between the nodes analysed ($ND_{n,n'}$, [km]) and on the economic parameters presented in Table 4.8 [39].

$$TTC^{CCS,SHIP} = \sum_{n,n'} \left( \left( ND_{n,n'} \cdot UTC^{PIPE,SLP} + UTC_{n,n'}^{PIPE,INT} \right) \cdot \sum_{t} M_{t,n,n'}^{CO2,EXC,SHIP} \right) \quad (4.8)$$

Table 4.8. Flow rate-based classification of the unitary cost required for $CO_2$ transportation via ship [39]

| Size | $M_{q,y}^{CO2,MIN}$ [$Mt_{CO2}/y$] | $M_{q,y}^{CO2,MAX}$ [$Mt_{CO2}/y$] | $UTC_{n,n'}^{SHIP,SLP}$ [€/km/$t_{CO2}$] | $UTC_{n,n'}^{SHIP,INT}$ [€/$t_{CO2}$] |
|---|---|---|---|---|
| $q_1$ | 0.25 | 1.50 | 0.00609 | 12.911 |
| $q_2$ | 1.50 | 2.50 | 0.00609 | 11.911 |
| $q_3$ | 2.50 | 7.50 | 0.00609 | 7.911 |
| $q_4$ | 7.50 | 30.00 | 0.00609 | 7.911 |
| average | - | - | 0.00609 | 10.161 |

The cost related to the tonnes of $CO_2$ delivered, linearly depends on the nautical distance, through a slope ($UTC^{PIPE,SLP}$, [€/km/$t_{CO2}$]) and an intercept ($UTC^{PIPE,INT}$, [€/$t_{CO2}$]), from which the total transportation cost is obtained by multiplying the unitary cost for the continuous variable $M_{t,n,n'}^{CO2,EXC,SHIP}$[tCO2/h], accounting for the overall $CO_2$ moved via ship from the port of Taranto and the North Sea site. Analogously to the pipeline case, the economic parameters are provided for four flow rate ranges; however, for the route considered in this study, covering 5'471 km, the cost specific to the $CO_2$ delivered can be approximated with the average value, obtaining a maximum error of 6%, therefore the flow rate discretisation for ship transportation is not introduced in the model.

The last component of the CCS network cost structure consists in the total storage cost of Eq.(4.9), defined by a unitary sequestration cost ($USC^{CCS}$), equal to 7.2 €/$t_{CO2}$ and an additional cost required for storing $CO_2$ into an offshore site ($\Theta_n^{OFF}$), equal to 2.5 if the site is offshore, or 1 for onshore nodes [31].

$$TSC^{CCS} = USC^{CCS} \cdot \sum_n \left( \Theta_n^{OFF} \cdot \sum_t Q_{t,n}^{CO2,STORED} \right) \tag{4.9}$$

### 4.2.2 Cost of the HSC

Analogously to the CCS network, the HSC cost structure is divided into three contributions, accounting for the $H_2$ production ($TPC^{HSC}$), transportation ($TTC^{HSC}$) and storage ($TSC^{HSC}$) (4.10).

$$TC^{HSC} = TPC^{HSC} + TTC^{HSC} + TSC^{HSC} \tag{4.10}$$

In the proposed infrastructure, hydrogen production occurs via electrolysis or via steam methane reforming. According to the total cost minimisation algorithm, the infrastructure can install the $H_2$ production plants selecting among a set of suitable nodes. For what concerns green hydrogen, the production plant can be installed in correspondence to the

production nodes, where the RES generation occurs. Instead, only the NGCC nodes are suitable for installing a SMR for blue hydrogen production. The economic analysis of the $H_2$ production plants is based on the estimation of the plant capital (i.e., CAPEX) and operative (i.e., OPEX) expenditures . Since for the CCS network the economic analysis has been conducted in terms of annual cost, also the CAPEX related to the $H_2$ generation must be converted into an annual value. For this purpose, this thesis considers a simplified method [100], based on the capital recovery factor (CRF), defined in Eq.(4.11) as a function of the interest rate ($i$, [%]), assumed equal to 10% [101], and the plant lifetime ($LT$, [y]). The simplified method turns the investment cost into an annual value by simply multiplying the CRF for the CAPEX.

$$CRF = \frac{i \cdot (1+i)^{LT}}{(1+i)^{LT} - 1} \tag{4.11}$$

Table 4.9 reports the main results of the performance and economic analysis applied to the PEM Electrolyser [100][101] and the SMR [14]. The electrolyser determines an electricity consumption specific to the hydrogen produced ($e^{CNS,SP}$, [$MWh_{EL}/t_{H2}$]), while for the SMR this parameter is negative, since electricity is generated by the steam turbine integrated in the plant. The other performance parameters, specific to the tonnes of $H_2$ produced, are defined for the SMR and represent the natural gas consumption ($m^{NG,SMR,SP}$, [$t_{NG}/t_{H2}$]), the $CO_2$ emitted in the atmosphere ($m^{CO2,EM}$, [$t_{CO2}/t_{H2}$]) and the $CO_2$ captured ($m^{CO2,CAPT}$, [$t_{CO2}/t_{H2}$]).

Table 4.9. Performance and economic parameters of the hydrogen production via electrolysis [16] [19] or SMR [14]

| Parameter | | PEM Electrolyser | SMR (1a) | SMR (3) |
|---|---|---|---|---|
| $m^{NG,SMR,SP}$ | [$t_{NG}/t_{H2}$] | - | 3.548 | 3.774 |
| $m^{CO2,EM}$ | [$t_{CO2}/t_{H2}$] | - | 4.151 | 0.995 |
| $m^{CO2,CAPT}$ | [$t_{CO2}/t_{H2}$] | - | 5.222 | 8.970 |
| $e^{CNS,SP}$ | [$MWh_{EL}/t_{H2}$] | 50.074 | - 0.167 | -0.048 |
| CAPEX | [M€/($t_{H2}$/h)] | 35.553 | 22.614 | 34.216 |
| Lifetime | [Years] | 10 | 25 | 25 |
| CRF | [%] | 16 | 11 | 11 |
| $UPC^{CAPEX}$ | [M€/($t_{H2}$/h)/y] | 5.786 | 2.491 | 3.770 |
| $UPC^{OPEX}$ | [M€/($t_{H2}$/h)/y] | - | 0.982 | 1.293 |

The values related to the green hydrogen production are provided by Quarton et al. [16] and Reuß et al. [19], providing similar values for the specific electricity consumption, respectively 52.55 and 47.60 $MWh_{EL}/t_{H2}$, but differing in terms of CAPEX, respectively estimated as 920 and 500 €/$kW_{EL}$. The parameters provided in Table 4.9 result from an algebraic average among the two models analysed. For what concerns the SMR parameters, the reference considered in this thesis is a technical report published by the IEA [14], assessing the performance and economic parameters of such plant. That report considers a reference SMR plant producing 100'000 $Nm^3/h$ of $H_2$, from which five case studies are developed. The simplest one, to which the values in the column SMR (1a) of Table 4.9 refer, considers a pre-combustion capture from shifted syngas using MDEA, resulting the most economic implant choice, although it determines a higher $CO_2$ emission in the atmosphere. The other case study considered in this thesis is the one determining the lowest CO2 emission (case 3), consisting in a SMR plant with capture of $CO_2$ from flue gas using MEA. The infrastructure cannot choose the type of SMR to install, since this choice is provided a priori to the algorithm in order to limit the computational burden. In addition to the fixed OPEX, including labour, taxes and maintenance, the natural gas consumption of the SMR determines an additional annual cost, obtained by multiplying the annual demand of natural gas for a specific cost of the fuel ($UC^{NG}$), assumed as equal to 386.7 €/$t_{NG}$ [102]. The total production cost of the HSC (4.12) provides a linear dependence on the variable $M_n^{H2,PRD,NOM}$ [$t_{H2}$/h], representing the nominal capacity of the plant, multiplied for the unitary production cost, comprehensive of CAPEX ($UPC_n^{CAPEX}$) and OPEX ($UPC_n^{OPEX}$), to which is then added, for the SMR, the additional cost related to the natural gas consumed, depending on the cumulated annual value of the variable $M_{t,n}^{H2,PROD,TOT}$, representing the $H_2$ produced in node *n* at the timestep *t*.

$$TPC^{HSC} = \sum_n \left( (UPC_n^{CAPEX} + UPC_n^{OPEX}) \cdot M_n^{H2,PRD,NOM} + UC^{NG} \cdot m_n^{NG,SMR,SP} \cdot \sum_t M_{t,n}^{H2,PROD,TOT} \right) \tag{4.12}$$

The total cost associated to hydrogen transportation is proportional to the dimension of the pipeline installed. Reuß et al. [19] provide a parabolic correlation between the transportation cost, specific to the distance covered, and the pipe diameter. The dependence on the diameter is then turned into a function of the $H_2$ flow rate delivered between the nodes, assuming to transport $H_2$ with a speed of 4 m/s and density of 8 $kg/m^3$, obtained assuming a pressure of 100 bar, temperature 24°C and compressibility factor of 1.013 [103]. The investment cost is then converted into an annual value considering a lifetime of 40 years [19], from which results a CRF of 10.02% (Figure 4.1). The transportation cost function is finally obtained (4.13), as a linear function of the variable

$M_{n,n'}^{H2,EXC,NOM}$[$t_{H2}$/h], representing the maximum flow rate delivered between nodes *n* and *n'*. To the installation cost is then added an operating cost ($c^{H2,OP}$, [€/$t_{H2}$]) of 50€ for each tonne of $H_2$ moved by the pipe ($M_{t,n,n'}^{H2,EXC}$, [$t_{H2}$/h]). A high uncertainty affects $c^{H2,OP}$, being estimated considering the operating cost of the $H_2$ pipeline as one third of the total transportation cost, provided in literature as equal to 1.5 € for each kg of transported $H_2$.

$$\mathrm{TTC}^{\mathrm{HSC}} = \sum_{n,n'} \left( (\alpha^{H2,PPL} \cdot M_{n,n'}^{H2,EXC,NOM} + \beta^{H2,PPL} \cdot \lambda_{n,n'}^{H2,PPL}) \cdot LD_{n,n'} + c^{H2,OP} \cdot \sum_{t} M_{t,n,n'}^{H2,EXC} \right) \tag{4.13}$$

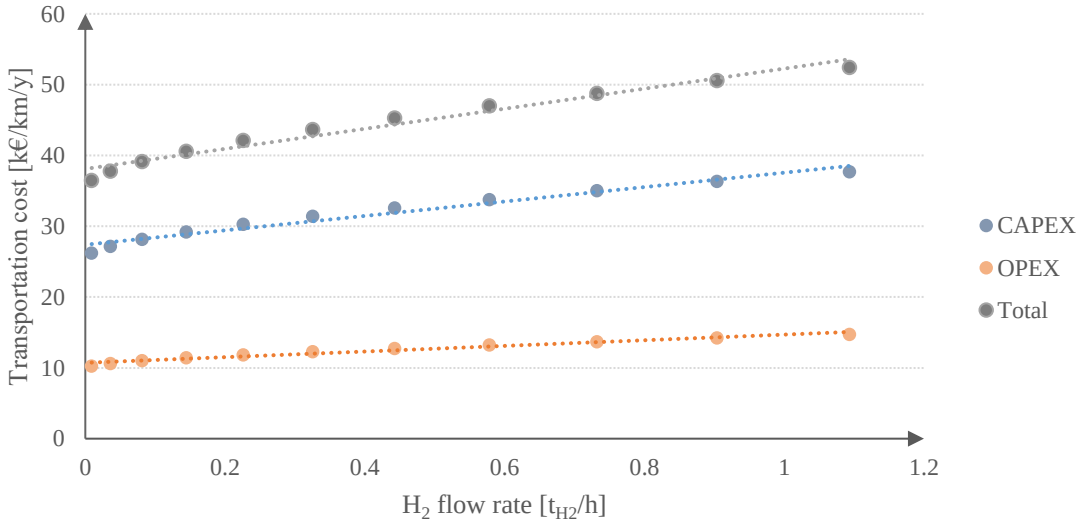


Figure 4.1. Hydrogen transportation cost (grey line) and its breakdown into capital (blue line) and operational (orange line) components, as a function of the transported amount [19].

The other terms appearing in the cost function are the unitary transportation cost, defined with a linear function with slope $\alpha^{H2,PPL}$ [€/km/($t_{H2}$/h)/y] and intercept $\beta^{H2,PPL}$ [€/km/y], both obtained from the sum between the CAPEX and OPEX contributions, with the OPEX equal to 4% of the total investment cost, and a binary variable $\lambda_{n,n'}^{H2,PPL}$, equal to 1 if a $H_2$ pipeline is installed between nodes *n* and *n'*, and 0 otherwise.

A final contribution to the HSC total cost is provided by the $H_2$ storage into pressurised tanks, allowing to decouple the hydrogen production and consumption, particularly useful with high penetration of renewable electrolysers in the hydrogen production chain. The mathematical model provides the possibility for the infrastructure to install hydrogen storage tanks in correspondence with the production sites, therefore NGCC and PN nodes. The total storage cost (4.14) is provided as a function of the variable $M_n^{H2,STR,MAX}$[$t_{H2}$], representing the maximum cumulated $H_2$ stored in node *n*. The unitary storage CAPEX

($USC_n^{CAP}$, [€/$t_{H2}$/y]) is obtained from a total investment cost of 500 €/$kg_{H2}$ [19], multiplied for a CRF equal to 11.45%, resulting from an expected lifetime of 20 years, while the operative costs ($USC_n^{OP}$) are assumed as 2% of the total investment cost [19].

$$TSC^{HSC} = \sum_n ((USC_n^{CAP} + USC_n^{OP}) \cdot M_n^{H2,STR,NOM}) \quad (4.14)$$

### 4.2.3 Other costs

Another cost term is related to the additional RES capacity installed (4.15), defined as the product between the pre-existent capacity of solar PV ($C_n^{PV,2018}$, [$MW_{EL}$]) and wind power ($C_n^{WIND,2018}$), and the variables $\varepsilon^{PV}$ and $\varepsilon^{WIND}$, representing the increase in the available capacity of the two RES sources with respect to the 2018 value. To each $MW_{EL}$ of installed capacity is associated a unitary cost ($UC^{PV}$ and $UC^{WIND}$, [M€/$MW_{EL}$/y]) provided in Table 4.10.

$$TC^{RES} = \sum_n (C_n^{PV,2018} \cdot \varepsilon^{PV} \cdot UC^{PV} + C_n^{WIND,2018} \cdot \varepsilon^{WIND} \cdot UC^{WIND}) \quad (4.15)$$

Table 4.10. Investment cost required for installing additional capacity of solar PV and wind turbines

| Parameter | | Solar PV | Wind turbine |
|---|---|---|---|
| $CAPEX$ [104] [105] | [M€/MW] | 0.88 | 1.50 |
| Lifetime [106] [107] | [years] | 25 | 20 |
| CRF | [%] | 11.02 | 11.75 |
| UC | [M€/MW/y] | 0.097 | 0.176 |

Another contribution to Eq.(4.2) consists in a virtual cost, representing the electricity imported from the other Italian regions, allowing the optimisation algorithm to always close the energy balance, satisfying the energy requirement of the region at each timestep *t*. A continuous variable $E_{t,n}^{IMP}$[$MWh_{EL}$/h]) is introduced, accounting for the electricity imported from an import node *n*, to which is associated a high unitary cost ($UC^{ELC,IMP}$) of 1'000 €/$MWh_{EL}$, in order to give priority to the electricity sources internal to the region (4.16).

$$TC^{ELC,IMP} = \sum_{t,n} E_{t,n}^{IMP} * UC^{ELC,IMP} \quad (4.16)$$

The total cost structure of the infrastructure is then completed with the contribution of the fuel consumption (4.17), consisting in coal ($TC^{FUEL,COAL}$, [M€/y]) and natural gas ($TC^{FUEL,NG}$).

$$TC^{FUEL} = TC^{FUEL,COAL} + TC^{FUEL,NG} \tag{4.17}$$

The cost associated to the coal consumption (4.18) depends on the variable $prod_{t,n}$ [%], representing the ratio between the production of the site *n* at the timestep *t* and nominal capacity ($C_n^{NOM}$, [$t_{PROD}$/h]). The other factors appearing in the cost function consist in the coal unitary cost ($UC^{COAL}$, =150 €/$t_{COAL}$ [108]) and the coal consumed in each node *n* per unit of product ($m_n^{COAL,SP}$, [$t_{COAL}$/prod_unit]), also including the petcoke specific consumption.

$$TC^{FUEL,COAL} = UC^{COAL} \cdot \sum_n \left( C_n^{NOM} \cdot m_n^{COAL,SP} \cdot \sum_t prod_{t,n} \right) \tag{4.18}$$

For what concerns natural gas consumption, Eq.(4.19) provides the total cost associated to the quantity of such fuel demanded by the infrastructure.

$$TC^{FUEL,NG} = UC^{NG} \cdot \sum_{t,n} M_{t,n}^{NG,CONS} \tag{4.19}$$

The term $M_{t,n}^{NG,CONS}$[$t_{NG}$/h] represents the natural gas consumed in each node *n* at each timestep *t*. For NGCC and CN, $M_{t,n}^{NG,CONS}$ represents a variables set of the problem, subjected to the constraints provided in the following section, without considering the consumption related to the $H_2$ production in the SMR, already accounted in Eq.(4.12). For industries and coal power plants, instead, the natural gas demand (4.20) is determined analogously with the coal consumption as a function of the value specific to one product unit ($m_n^{NG,SP}$, [$t_{NG}$/prod_unit]).

$$M_{t,n}^{NG,CONS} = C_n^{NOM} \cdot m_n^{NG,SP} \cdot prod_{t,n} \tag{4.20}$$

## 4.3 Constraints

The cost minimisation problem is constrained with a set of additional equations and inequalities, necessary for guaranteeing the energy and mass conservation in each node of the infrastructure. In detail, a set of constraints regulates the production, consumption and distribution of electricity, $CO_2$ and hydrogen, accounting both for the physical limits and design choices of the infrastructure. An additional constraint is finally introduced, imposing the $CO_2$ emission reduction target.

### 4.3.4 Electricity balance

The electricity balance (4.21) is applied to the whole infrastructure at each hour *t* and includes the power generation ($E_{t,n}^{GEN}$, [$MWh_{EL}$/h]) and the demand requested by the consumers ($E_{t,n}^{CONS}$, [$MWh_{EL}$/h]), divided by a term $\xi^{ELC}$ (=0.98) accounting for the electricity losses in the transmission grid.

$$\sum_{n}\left(E_{t,n}^{GEN}-\frac{E_{t,n}^{CONS}}{\xi^{ELC}}\right)=0 \tag{4.21}$$

Although the electricity exchange has a central role in the definition of the electricity grid, being subjected to transport capacity limit and energy losses proportional to the distance covered by a line, electricity transportation is not considered in this study, due to the high computational burden required for adding such model to the infrastructure.

The electricity generated is determined by four contributions, being the thermoelectric power plants included in the steel and chemical industries and in the fuel refinery ($E_{t,n}^{GEN,IND}$), the remaining stand-alone thermoelectric power plants ($E_{t,n}^{GEN,PP}$), the renewable energy sources ($E_{t,n}^{GEN,RES}$), and the electricity imported from the other Italian regions (4.22).

$$E_{t,n}^{GEN}=E_{t,n}^{GEN,IND}+E_{t,n}^{GEN,PP}+E_{t,n}^{GEN,RES}+E_{t,n}^{IMP} \tag{4.22}$$

The mathematical expression of the term $E_{t,n}^{GEN,IND}$ (4.23) is linearly dependent on the electricity generated for each ton of product ($e_n^{SP,GEN}$, [$MWh_{EL}/t_{PROD}$]).

$$E_{t,n}^{GEN,IND}=C_n^{NOM,IND}\cdot e_n^{SP,GEN}\cdot prod_{t,n} \tag{4.23}$$

The variable $prod_{t,n}$ can assume any value in the range 0-1, although it is limited by the monthly demand for the industrial product ($C_{m,n}^{DEM}$, [$t_{PROD}$/month]) (4.24).

$$\sum_{t\in m}C_{t,n}^{MAX}\cdot prod_{t,n}=C_{m,n}^{DEM} \tag{4.24}$$

Another contribution to the electricity generation is provided by thermoelectric power plants, exploiting coal or natural gas as fuel. For what concerns the first energy source, the expression of the electricity generated keeps a structure similar to the industrial contribution, with a dependency on the nominal power installed ($C_n^{NOM,PP}$, $MW_{EL}$) and on the production rate. Instead, the energy provided by the NGCC nodes derives from two separate contributions, since in these points can be sited a thermoelectric power plant or a SMR for hydrogen production. The electricity generation from NGCCs is described analogously to the coal-fed power plant, while the SMR contribution depends on the

hydrogen produced and the related specific electricity generated as a co-product (4.25), already mentioned in Table 4.9.

$$E_{t,n}^{GEN,PP} = C_n^{NOM,PP} \cdot prod_{t,n} + M_{t,n}^{H2,PRD} \cdot e^{SMR,GEN,SP} \quad (4.25)$$

For what concerns solar PV and wind turbines, the energy generated is proportional to the nominal capacity available in 2018, majored of the capacity installed by the optimisation algorithm, and to the source availability among the year ($distr_{t,n}$, [$MW/MW_{NOM}$]) (4.26).

$$E_{t,n}^{GEN,RES} = C_n^{PV,2018} \cdot (1 + \xi^{PV}) \cdot distr_{t,n}^{PV} + C_n^{WIND,2018} \cdot (1 + \xi^{WIND}) \cdot distr_{t,n}^{WIND} \quad (4.26)$$

The installation of solar PV and wind power capacity is constrained by geographical and social limits, since the majority of the studied region territory is not suitable for RES capacity installation, due to a low availability of the sources in some areas and to the limits in the land exploitation [66]. For this reason, an upper bound of 0.2 is imposed to the variables $\varepsilon^{PV}$ and $\varepsilon^{WIND}$. Since this value is chosen arbitrarily, it represents an uncertain parameters, whose effect on the final results can be assessed with a sensitivity analysis.

Another role in the energy balance (4.48) is played by the electricity consumers, among which can be distinguished the terms related to industries ($E_{t,n}^{CONS,IND}$), and consumption and export nodes ($E_{t,n}^{CONS,CN,EN}$) (4.27).

$$E_{t,n}^{CONS} = E_{t,n}^{CONS,IND} + E_{t,n}^{CONS,CN,EN} \quad (4.27)$$

The industrial contribution (4.28) differs from the electricity generated only because of the parameter $e_n^{SP,CONS,IND}$ ($MWh_{EL}/t_{PROD}$), defined as the electricity consumption specific to one ton of product.

$$E_{t,n}^{CONS,IND} = C_n^{NOM} \cdot e_n^{SP,CONS} \cdot prod_{t,n} \quad (4.28)$$

The remaining electricity demand within the region is requested by the province nodes through two separated terms (4.29). The first one consists in the electric energy requirement of the consumption nodes, defined as the product between the overall annual consumption ($E_n^{CONS,CN,EL}$, [$MWh_{EL}/y$]) and its hourly distribution ($distr_{t,n}^{CN,EL}$, [$MW_{EL}/MWh_{EL}/y$]), while the second demand is for the green hydrogen produced via electrolysis, proportional to the amount of $H_2$ produced and to the related specific electricity consumption. The same equation can also be applied to the electricity export node, whose contribution is analogous to the consumption nodes one.

$$E_{t,n}^{CONS,CN,EN} = E_n^{CONS,CN,EN} \cdot distr_{t,n}^{EL,CN,EN} + M_{t,n}^{H2,PROD} \cdot e^{ELC,CONS,SP} \quad (4.29)$$

### 4.3.5 $CO_2$ nodal balance

The presence of a carbon capture, transportation and storage infrastructure requires the introduction of a nodal $CO_2$ mass balance at each timestep *t* (4.30), in which the total $CO_2$ captured ($M_{t,n}^{CO2,CAPT}$, [$t_{CO2}$/h]) has to be in equilibrium with the net $CO_2$ flow delivered to the other nodes, defined as the matrix product between the node-line incidence matrix and the $CO_2$ exchanged between nodes *n* and *n'* ($M_{t,n,n'}^{CO2,EXC}$), the $CO_2$ exchanged via ship ($M_{t,n}^{CO2,CAPT}$), positive if exiting the node, and the amount stored in the dedicated sites ($M_{t,n}^{CO2,STOR}$).

$$M_{t,n}^{CO2,CAPT} + a^{N,L} * M_{t,n',n}^{CO2,EXC,PPL} + M_{t,n}^{CO2,EXC,SHP} = M_{t,n}^{CO2,STOR} \quad (4.30)$$

The captured $CO_2$ is provided as the sum of two contributions, determined by the CCS section installed on the $CO_2$-intensive plants ($M_{t,n}^{CO2,CAPT,CCS}$), and $CO_2$ sequestered in the SMR ($M_{t,n}^{CO2,CAPT,SMR}$).

$$M_{t,n}^{CO2,CAPT,CCS} = \lambda_n^{CCS} \cdot C_n^{MAX} \cdot m_n^{CO2,SP} \cdot prod_{t,n} \cdot \rho_n^{CCS} \cdot \eta_n^{CAPT} \quad (4.31)$$

$$M_{t,n}^{CO2,CAPT,SMR} = M_{t,n}^{H2,PROD} \cdot m^{CO2,CAPT,SP} \quad (4.32)$$

The first term depends on the $CO_2$ emission specific to one production unit ($m_n^{CO2,SP}$, [$t_{CO2}$/prod_unit]), the performance parameters of the capture section and a binary variable $\lambda_n^{CCS}$, equal to 1 if CCS is installed in node *n*, or 0 otherwise (4.31). The contribution provided by the pre-combustion capture in the SMR is proportional to the hydrogen produced and to the related specific $CO_2$ emission (4.32).

The presence in Eq.(4.31) of a product between $prod_{t,n}$ and $\lambda_n^{CCS}$ makes this constraint non-linear, therefore the equation is replaced with a system of linear inequality constraints. The link between $M_{t,n}^{CO2,PROD}$ and $\lambda_n^{CCS}$ is expressed through a Big-M constraint, in which a large scalar M multiplies the binary variable, forcing the continuous one to assume value 0 if $\lambda_n^{CCS}$=0 (4.33). If $\lambda_n^{CCS}$ assumes value 1, instead, the variable $M_{t,n}^{CO2,CAPT}$ is constrained by an upper (4.34) and lower (4.48) bound, both equal to the $CO_2$ captured in plant *n*, allowing the variable to only be equal to this value.

$$M_{t,n}^{CO2,CAPT} \leq M * \lambda_n^{CCS} \quad (4.33)$$

$$M_{t,n}^{CO2,CAPT} - M_{t,n}^{CO2,PROD} \cdot \rho_n^{CCS} \cdot \eta_n^{CCS} \leq M \cdot (1 - \lambda_n^{CCS}) \quad (4.34)$$

$$M_{t,n}^{CO2,PROD} \cdot \rho_n^{CCS} \cdot \eta_n^{CCS} - M_{t,n}^{CO2,CAPT} \leq M \cdot (1 - \lambda_n^{CCS}) \quad (4.35)$$

Despite the modification, this constraint still remains non-linear for NGCC nodes since the $CO_2$ emission specific to the electricity produced depends on the hydrogen fraction in the thermal input. The linearity of the constraint is restored by referring the $CO_2$ produced to the amount of natural gas consumed ($M_{t,n}^{NG,CONS,NGCC}$, [$t_{NG}$/h]) and the related specific $CO_2$ production ($m^{CO2,NG,SP}$, [$t_{CO2}/t_{NG}$]) (4.36). The natural gas consumption can be computed

for NGCCs (4.37) from the thermal input required at each timestep, determined assuming, for simplicity, an electrical efficiency ($\eta_n^{EL,NGCC}$, [$MJ_{EL}/MJ_{LHV}$]) independent from the hydrogen fraction in the thermal input (4.48).

$$M_{t,n}^{CO2,PROD} = M_{t,n}^{NG,CONS,NGCC} \cdot m^{CO2,NG,SP} \tag{4.36}$$

$$M_{t,n}^{H2,CONS,NGCC} \cdot LHV^{H2} + M_{t,n}^{NG,CONS} \cdot LHV^{NG} = Q_{t,n}^{NG,LHV,IN} \tag{4.37}$$

$$Q_{t,n}^{H2,LHV,IN} = \frac{C_n^{NOM} \cdot prod_{t,n}}{\eta_n^{EL}} \tag{4.38}$$

After the capture section, the $CO_2$ flow is transported towards the storage sites via pipeline or ship. The amount of $CO_2$ moved via pipeline is represented by the set of positive continuous variables $M_{t,n,n'}^{CO2,EXC,PPL}$, defined with a LxT matrix, where T is length of the time set and L represents the lines satisfying the constraints introduced for the node-line incidence matrix definition. In this formulation, from the matrix product between $a^{N,L}$ and $M_{t,n,n'}^{CO2,EXC,PPL}$, occurring in Eq.(4.30), results a NxT matrix, representing the net $CO_2$ flow delivered to the other nodes from each node *n* at each timestep *t*. The other transport modality considered in this thesis occurs via ship, connecting the port of Taranto with the North Sea storage site. The $CO_2$ flow exchanged in this line is quantified with a positive continuous variable $M_t^{CO2,EXC,SHP}$: for PO01, this quantity appears in the $CO_2$ nodal balance defined in Eq.(4.30) with a minus sign, being exiting from such node, while for CS01 this variable is applied with a positive sign.

The $CO_2$ pipeline network is subjected to a series of constraints, assessing the size and type of connection occurring between two generic nodes *n* and *n'*. As reported in Table 4.7, the investment cost required for a pipeline is related to the maximum flow rate exchanged between the nodes. Since the "max" function available in MATLAB is not linear, an additional constraint is required for assessing the nominal capacity (4.39). In detail, this value is imposed higher or equal to the $CO_2$ exchanged at each timestep *t*: since this quantity is proportional to the total cost, and the goal of the infrastructure is an economic optimisation, the nominal capacity selected by the algorithm coincides with the maximum amount of $CO_2$ exchanged between nodes *n* and *n'*.

$$M_{t,n,n'}^{CO2,EXC,PIPE} \leq M_{n,n'}^{CO2,EXC,NOM} \tag{4.39}$$

Once the pipeline nominal size is set, the unitary transportation cost is determined by comparing this value with the flow rate ranges provided in Table 4.7. The definition of this constraint (4.40) requires the introduction of four sets of integer decision variables $\lambda_{n,n',q}^{CO2,PIPE}$, assuming value 1 if a pipeline of size *q* is installed between nodes *n* and *n'*, or 0 otherwise.

$$\sum_{q} \lambda_{n,n\prime,q}^{CO2,PIPE} \cdot M_{q,y}^{CO2,MIN} \leq M_{n,n'}^{CO2,EXC,NOM} \leq \sum_{q} \lambda_{n,n\prime,q}^{CO2,PIPE} \cdot M_{q,y}^{CO2,MAX} \quad (4.40)$$

An additional constraint (4.41) to the $CO_2$ pipeline transportation is finally introduced, preventing the optimisation algorithm from installing two or more different connections between two nodes *n* and *n'*.

$$\sum_{\mathrm{q}} \lambda_{\mathrm{n,n\prime,q}}^{\mathrm{CO2,PIPE}} + \lambda_{\mathrm{n,n\prime}}^{\mathrm{CO2,SHIP}} \leq 1 \quad (4.41)$$

The $CO_2$ balance (4.30) is closed with the introduction of the storage sites. A continuous positive variable $M_{t,n}^{CO2,STORE}$[$t_{CO2}$/h], is introduced, accounting for the amount of $CO_2$ stored in each node *n* at each timestep *t*. The cumulated $CO_2$ stored in each site must not exceed its maximum capacity ($M_{n}^{CO2,STORE,MAX}$, [$t_{CO2}$]) (4.42).

$$\sum_{t} M_{t,n}^{CO2,STORE} \leq M_{n}^{CO2,STORE,MAX} \quad (4.42)$$

### 4.3.6 Hydrogen nodal balance

The infrastructure includes an HSC, in which the hydrogen produced, the net $H_2$ exiting node *n*, resulting from a matrix product between $a^{N,L}$ and the hydrogen exchanged between two nodes *n* and *n'* ($M_{t,n,n'}^{H2,EXC}$, [$t_{H2}$/h]), the demand ($M_{t,n}^{H2,CONS}$), and the quantity exchanged with the storage tanks ($M_{t,n}^{H2,STR}$) have to be in equilibrium for each node *n* at each timestep *t* (4.43).

$$M_{t,n}^{H2,PROD} + a^{N,L} \cdot M_{t,n,n\prime}^{H2,EXC} = M_{t,n}^{H2,CONS} + M_{t,n}^{H2,STR} \quad (4.43)$$

The hydrogen production echelons considered in this study are steam methane reforming from natural gas, integrated with a pre-combustion CCS technology, and water electrolysis from renewable electricity, in detail solar PV and wind turbines. The green hydrogen production is constrained by the availability of the renewable sources (4.44). Although the electrolysis process could exploit non-renewable electricity, this option is not modelled in the infrastructure, due to the CO2 emitted in the electricity generation process.

$$M_{t,n}^{H2,PROD,ELC} \cdot e^{ELC,CONS,SP} \leq E_{t,n}^{GEN,RES} \quad (4.44)$$

A more complex set of constraints is necessary for describing the interaction between the NGCCs and the SMRs. In detail, this work considers integrated SMR-NGCC systems, in which the SMR generates hydrogen from natural gas, for then providing $H_2$ to the NGCC or to the HSC. The definition of such constraints requires the introduction of a set of variables, describing the operation of the node. In detail, continuous positive variables

quantify the hydrogen exported to the HSC ($M_{t,n}^{H2,PROD}$, [$t_{H2}$/h]), the $H_2$ delivered from the SMR to the NGCC ($M_{t,n}^{H2,CONS,SMR}$) and the quantity demanded by the NGCC to the HSC ($M_{t,n}^{H2,CONS}$), along with a set of binary variables, being $\lambda_n^{SMR}$, defining whether a SMR is installed in node *n*, and $\lambda_{t,n}^{EXP,SMR}$, assuming value 1 if node *n* exports $H_2$ to the grid at the timestep *t*. The definition of the variable $\lambda_{t,n}^{EXP,SMR}$ implies that this quantity can assume value 1 only if $\lambda_n^{SMR}$ is different from zero (4.45). The combination of the continuous and binary variables allows to define four different pathways for mitigating the $CO_2$ emitted by the NGCC nodes (Figure 4.2).

$$\lambda_{t,n}^{EXP,SMR} \leq \lambda_n^{SMR} \tag{4.45}$$

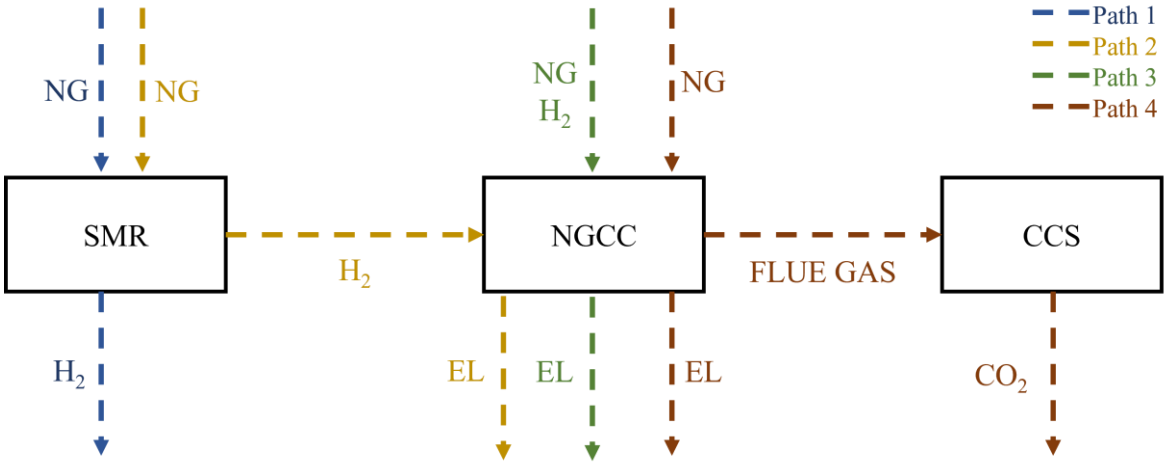


Figure 4.2. Schematic representation of the four $CO_2$ emission mitigation pathways for NGCC nodes.

- The first pathway occurs when both $\lambda_n^{SMR}$ and $\lambda_{t,n}^{EXP,SMR}$ assume value 1, therefore the SMR is installed exporting $H_2$ to the grid. In this case, due to the low flexibility of integrated SMR-NGCC plants, this model denies the possibility to simultaneously produce $H_2$ and electricity, therefore if this path is selected, the gas turbine is turned off (4.46), and the variables $M_{t,n}^{H2,CONS,SMR}$ and $M_{t,n}^{H2,CONS}$ assume value 0, since the total $H_2$ consumed by the combined cycle depends on the production rate (4.37).

$$prod_{t,n} \leq M \cdot (1 - \lambda_{n,t}^{EXC,SMR}) \tag{4.46}$$

- The second pathway differs from the first one because of the variable $\lambda_{t,n}^{EXP,SMR}$, assuming value 0, implying a null $H_2$ flow rate exported to the HSC (4.47) and the combined cycle can generate electricity by consuming natural gas and $H_2$ received only from the SMR (4.48). Since the $CO_2$ concentration in the exhaust gases emitted by the NGCC is strongly dependent on the fraction of $H_2$ in the thermal input, the economic and performance parameters of an additional post-combustion $CO_2$ capture section are

different from the pure natural gas-fed cycle case, therefore this thesis excludes the possibility to install a SMR and a CCS technology in the same node (4.49).

$$M_{t,n}^{H2,PROD} \leq M \cdot \lambda_{n,t}^{EXC,SMR} \tag{4.47}$$

$$M_{t,n}^{H2,\mathrm{CONS}} \leq M \cdot (1 - \lambda_{n,t}^{EXC,SMR}) \tag{4.48}$$

$$\lambda_n^{SMR} + \lambda_n^{CCS} \leq 1 \tag{4.49}$$

- The third and fourth pathways occur if the SMR is not installed in the node (4.50), and the mitigation strategies introduced are, respectively, $H_2$ consumption from the HSC and a post-combustion $CO_2$ capture section.

$$M_{t,n}^{H2,PROD} + M_{t,n}^{H2,CONS,SMR} \leq M \cdot \lambda_n^{SMR} \tag{4.50}$$

Another constraint regarding the hydrogen production is related to the nominal capacity of the plant, characterising the cost functions of such elements. The definition of this positive continuous variable ($M_n^{H2,PROD,NOM}$, [$t_{H2}$/h]) is analogous to the nominal capacity of the $CO_2$ pipeline, therefore it can be expressed, for each timestep *t* and node *n*, as shown in Eq.(4.51). For what concerns $H_2$ production via SMR, the performance parameters are referred to the sum of the variables $M_{t,n}^{H2,PROD}$ and $M_{t,n}^{H2,CONS,SMR}$ (4.52).

$$M_{t,n}^{H2,PROD,\mathrm{TOT}} \leq M_n^{H2,PROD,NOM} \tag{4.51}$$

$$M_{t,n}^{H2,PROD,TOT} = M_{t,n}^{H2,CONS,SMR} + M_{t,n}^{H2,PROD} \tag{4.52}$$

A similar condition is imposed for the hydrogen transportation via pipeline, economically defined with a continuous positive variable $M_{n,n'}^{H2,EXC,NOM}$[$t_{H2}$/h], quantifying the nominal flow rate delivered by the pipe (4.53). The cost structure of the $H_2$ pipeline also depends on the binary variable $\lambda_{n,n'}^{H2,PPL}$, forcing the $H_2$ transported between nodes *n* and *n'* to assume value 0 if $\lambda_{n,n'}^{H2,PPL}$ is equal to 0 (4.54).

$$M_{t,n,n'}^{H2,EXC} \leq M_{n,n'}^{H2,EXC,NOM} \tag{4.53}$$

$$M_{t,n,n'}^{H2,EXC} \leq M \cdot \lambda_{n,n'}^{H2,PPL} \tag{4.54}$$

Analogously to the electricity and $CO_2$ exchange among the nodes, the positive continuous variables set $M_{t,n,n'}^{H2,EXC}$ is defined with a LxT matrix, in order to obtain, from the matrix product with the node-line incidence matrix appearing in the $H_2$ nodal balance (4.43), the net $H_2$ flow exiting node *n* at each timestep *t*.

The goal of the $H_2$ pipeline system is to deliver hydrogen to the final users, consisting in NGCCs and consumption nodes, exploiting $H_2$ for substituting a portion of the natural gas-based thermal input. For residential utilities, this application is limited by the lower flammability point and the higher flame speed of hydrogen with respect to natural gas,

determining the necessity to modify the combustor to efficiently operate with a different fuel. These adjustments, however, can be avoided by limiting the volumetric fraction of blended hydrogen to a certain threshold, assumed as equal to 15% (corresponding to 20.17 $kg_{H2}/t_{NG}$), under which the change in the fuel properties should not be too detrimental for the natural gas-based devices (4.55) [109]. The natural gas used in the consumption nodes is determined by maintaining a constant thermal requirement at each timestep *t*, computed from the total natural gas demanded by each province in 2018 ($M_n^{NG,CN}$, $[t_{NG}/y]$) and its hourly distribution along the year ($distr_{t,n}^{NG,CN}$) (4.56).

$$M_{t,n}^{H2,CONS} \leq \alpha^{BLEND} \cdot M_{t,n}^{NG,CONS} \tag{4.55}$$

$$M_{t,n}^{H2,CONS} \cdot LHV^{H2} + M_{t,n}^{NG,CONS} \cdot LHV^{NG} = M_n^{NG,CN} \cdot distr_{t,n}^{NG,CN} \cdot LHV^{NG} \tag{4.56}$$

For what concerns the NGCCs, this limit on the hydrogen exploitation is not imposed, since these plants can be adapted to operate up to 100% $H_2$ without introducing substantial modifications to the plant scheme [13].

The $H_2$ mass balance expressed in Eq.(4.43) closes with the hydrogen exchanged with the storage tank, represented by the continuous variable $M_{t,n}^{H2,STR}[t_{H2}/h]$, assuming a positive value if $H_2$ is delivered to the storage tank, or negative values if the energy vector is injected in the $H_2$ grid. This decision variable is limited by the $H_2$ contained in the storage tank, physically forced at being higher or equal to zero (4.57). This constraint is applied at each timestep *t*, excluded the first hour of the year, in which the amount of storage $H_2$ is assumed as equal to 0. The cumulated value of the stored $H_2$ also determines the total cost of the tank. An inequality constraint is added, for each node *n* at each timestep *t*, for assessing the nominal capacity of the storage tank ($M_n^{H2,STR,NOM}$) (4.58).

$$\sum_{T=1}^{t} M_{T,n}^{H2,STR} \geq 0 \tag{4.57}$$

$$\sum_{T=1}^{t} M_{T,n}^{H2,STR} \leq M_n^{H2,STR,NOM} \tag{4.58}$$

### 4.3.7 $CO_2$ emission constraint

The constraints set is finally completed with the addition of a upper $CO_2$ emission threshold ($\alpha^{CO2}$) (4.59), relating the amount of $CO_2$ emitted in the region before ($M^{CO2,EM,BASE}$, $t_{CO2}$/year) and after ($M_n^{CO2,EM,MODEL}$) the implementation of the infrastructure, with a value chosen accordingly to the modelled scenario.

$$\sum_{n} M_n^{CO2,EM,MODEL} \leq \alpha^{CO2} \cdot M^{CO2,EM,BASE} \tag{4.59}$$

The base case can be implemented with the $CO_2$ emission values computed with the algorithm by imposing all the binary variables as equal to zero. The amount of $CO_2$ emitted when the model is applied, instead, requires a deeper analysis, since for industries and thermoelectric power plants this parameter assumes different values depending on the presence of a $CO_2$ capture section. In detail, the parameter $M_n^{CO2,EM,MODEL}$ is turned into a positive continuous variable, determined by the value of the binary variable $\lambda_n^{CCS}$. If CCS is not installed in node *n*, the variable $M_n^{CO2,EM,MODEL}$ is equal to the total annual $CO_2$ produced in node *n* without the introduction of the CCS technology, while if $\lambda_n^{CCS}$=1 the CO2 emitted in the model equals the total annual $CO_2$ produced in node *n* if the CCS technology is installed (4.61).

$$M_n^{CO2,EM,MODEL} = \sum_t M_{t,n}^{CO2,PROD} \cdot \lambda_n^{CCS} + \sum_t M_{t,n}^{CO2,PROD} \cdot \rho_n^{CCS} \cdot (1 - \eta_n^{CAPT}) \cdot (1 - \lambda_n^{CCS}) \quad (4.60)$$

Analogously to (4.31), the product between $M_{t,n}^{CO2,PROD}$ and $\lambda_n^{CCS}$ makes the equation non-linear, therefore Eq.(4.61) must be linearised with the introduction of big-M constraints. In detail, If CCS is not installed in node *n*, the variable $M_n^{CO2,EM,MODEL}$ is limited with an upper (4.61) and lower (4.62) bounds, both defined with the same threshold in order to force $M_n^{CO2,EM,MODEL}$ to be equal to the total annual $CO_2$ produced in node *n* without the introduction of the CCS technology.

$$M_n^{CO2,EM,MODEL} - \sum_t M_{t,n}^{CO2,PROD} \leq M \cdot \lambda_n^{CCS} \quad (4.61)$$

$$\sum_t M_{t,n}^{CO2,PROD} - M_n^{CO2,EM,MODEL} \leq M \cdot \lambda_n^{CCS} \quad (4.62)$$

If $\lambda_n^{CCS}$=1, upper (4.63) and lower (4.64) bounds limit the variable $M_n^{CO2,EM,MODEL}$, analogously to the previous case, this time with a threshold corresponding to the total annual $CO_2$ produced in node *n* if the CCS technology is installed.

$$M_n^{CO2,EM,MODEL} - \sum_t M_{t,n}^{CO2,PROD} \cdot \rho_n^{CCS} \cdot (1 - \eta_n^{CAPT}) \leq M \cdot \lambda_n^{CCS} \quad (4.63)$$

$$\sum_t M_{t,n}^{CO2,PROD} \cdot \rho_n^{CCS} \cdot (1 - \eta_n^{CAPT}) - M_n^{CO2,EM,MODEL} \leq M \cdot \lambda_n^{CCS} \quad (4.64)$$

# Chapter 5
# Results

Chapter 4 discussed the mathematical model developed in this thesis, which has the aim of economically optimising the installation and operation of an infrastructure for the integration of multiple $CO_2$ emission mitigation strategies within a region, including hydrogen and the related hydrogen supply chain (HSC), carbon capture and sequestration (CCS) and additional RES power generation, under a given demand for energy vectors. The model is designed to optimise the installation of technologies and the operation of the infrastructure during each hour of the year, in order to account for the year-long distribution of the energy vector generation and demand from generation and consumption nodes. The dense temporal resolution on which the proposed model is based determines a high complexity in the optimisation algorithm, which contains a very large number of variables and constraints necessary for modelling the 8'760 hours in a year. As a consequence, the model results with a high time-intensity in the optimisation process for the assessment of the optimal configuration of the infrastructure, despite the measures introduced in the formulation of the mathematical model aiming at limiting this issue, among which the removal of a nodal description in the electricity balance and the introduction of a distance limit for node-to-node connection.

The first simulations are run with the complete model formulation, showing that the solver time, at growing time horizon, becomes unfeasible with a commercial computer or workstation in a reasonable time limit (i.e., does not complete within 7 days of running code). In order to provide results capable to show the model behaviour, to assess the code validity, and verify the physical correctness, the model is applied on the simulation of a reduced time period. The time intensity of the optimisation phase results strongly dependent on the modelled temporal horizon: for a three days-period, convergence is reached in around 800 s, while simulating one operating week requires more than 10 hours to be modelled. The results discussed in this chapter are therefore referred to the application of the proposed model on one week. The objective function is adjusted accordingly, to weight the investment cost on the fraction of year taken into account, so as the demand for the industrial nodes, determined by scaling the monthly production on the studied time period. Although the results may not be taken as the actual optimal configuration, these analyses prove useful for assessing the correctness and completeness

of the model. Moreover, simulating a winter and a summer week appears useful to assess extreme weather conditions and their impact on the model results. The main element that cannot be properly assessed is the seasonal energy storage need, which is expected to be relevant for hydrogen technologies.

The proposed model is applied in five case studies, the first one being a base case, in which to all the decision variables associated to the application of the $CO_2$ emission mitigation strategies is assigned value 0. As discussed in Chapter 4, the total $CO_2$ produced in this scenario is applied in the mathematical model to compute the $CO_2$ emission threshold, according to the imposed reduction target. The complete model is then applied on a June and January week, representative of summer and winter time periods, constituting Cases 1A and 1B. The $CO_2$ emission reduction target is imposed as 65% with respect to the base case level, resulting the maximum value achievable for Case 1B. The same target is applied for two additional scenarios, in which the model is forced to install an HSC alongside the CCS network, considering again the first week of June (Case 2A) and January (Case 2B) as modelled time periods. In detail, two constraints are added to the mathematical model on an annual basis, being a minimum total hydrogen thermal input in the NGCC sector ($\alpha^{TH,MIN,NGCC}$ = 20%) (5.1) and a minimum blending limit for the residential sector ($\alpha^{BLD,MIN,CN}$) (4.48), imposed as 10% volumetric of the $H_2$-NG mixture.

$$\alpha^{TH,MIN,NGCC} \leq \sum_{t,n} \frac{M_{t,n}^{H2,NGCC} * LHV^{H2}}{M_{t,n}^{H2,NGCC} * LHV^{H2} + M_{t,n}^{NG,NGCC} * LHV^{NG}} \tag{5.1}$$

$$\alpha^{BLD,MIN,CN} \leq \sum_{t,n} \frac{M_{t,n}^{H2,CN}}{M_{t,n}^{NG,CN}} \tag{5.2}$$

For what concerns the SMR, Cases 2A and 2B consider the plant to be equipped with the post-combustion capture technology, being the more efficient solution in terms of $CO_2$ emission mitigation.

The following sections present and discuss the results for Cases 1A and 2A. The same values are reported for Cases 1B and 2B in the Appendix.

## 5.1 Base case

The relatively small number of variables and constraints of the base case with respect to the complete mathematical model provided in Chapter 4 determines a low time-consuming execution, providing the optimal solution for one operative year in less than a minute. Such solution provides a value of total $CO_2$ emission of 22.5 $Mt_{CO2}$/y, along a total operation cost of 2'446 M€/y. The $CO_2$ emission value, representing the reference for the other scenarios, implies a reduction of the 10.5% with respect to the 2018 value estimated in

Chapter 3. Such difference is related to the introduction of some approximation, among which having neglected minor thermal sources for NGCCs, like diesel and fuel gases, but also to a strongly different operation of thermoelectric power plants between the base case and the 2018 (Figure 5.1).

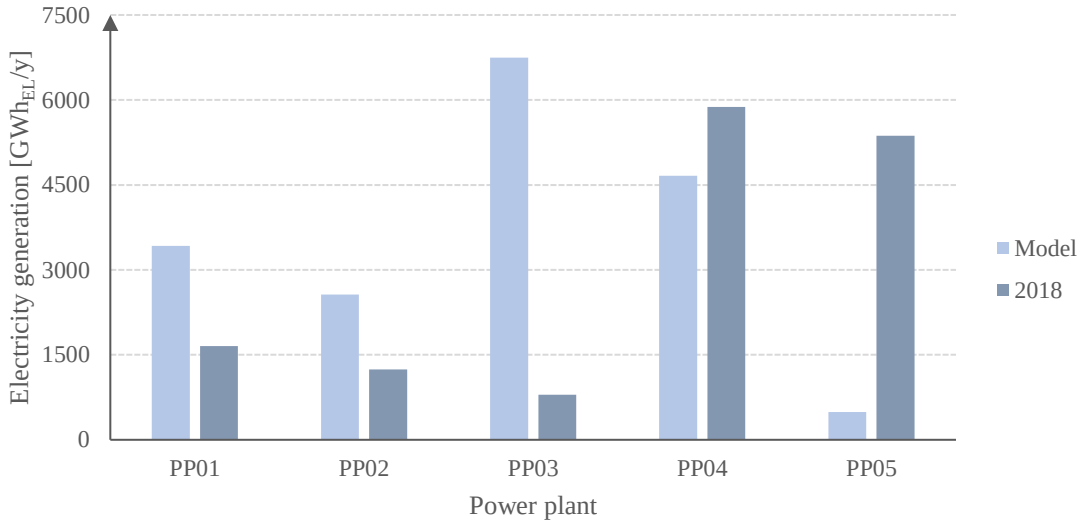


Figure 5.1. Electricity generated by the thermoelectric power plants in the base case and in 2018.

Despite the lower cost of coal with respect to natural gas, being respectively 5.78 €/GJ$_{TH}$ and 8.33 €/GJ$_{TH}$, the only coal-fed thermoelectric power plant undergoes an almost completely fade out from the electricity generation mix with respect to the 2018 level. This phenomenon is related to the lower electrical efficiency of such plant with respect to the NGCCs (Table 5.1), determining a higher cost specific to the electricity generated, making PP05 economically disadvantageous for the optimisation algorithm, only exploiting this source in case the capacity of the other power plants is not enough to satisfy the electricity requirement of the studied region. Since the electricity balance is only applied to the whole infrastructure without any transportation limit, the exploitation of the available power plants is only related to the electrical efficiency. In detail, plants PP01 and PP03 are exploited at the nominal capacity for almost the entire year, while PP04, responsible for the major contribution to the electricity generation from this sector in 2018, in less exploited in the base case.

Table 5.1. Electrical efficiency and average production rate in the base case and 2018 for the thermoelectric power plants considered in this study

| Plant | Fuel consumed | Fuel-to-electricity efficiency [%] | Average generation rate [$MW/MW_{NOM}$] | |
|---|---|---|---|---|
| | | | Model | 2018 |
| PP01 | Natural gas | 58.0 | 0.97 | 0.47 |
| PP02 | Natural gas | 51.2 | 0.82 | 0.40 |
| PP03 | Natural gas | 56.4 | 0.97 | 0.11 |
| PP04 | Natural gas | 49.3 | 0.40 | 0.51 |
| PP05 | Coal | 29.9 | 0.02 | 0.23 |

The value of the imported electricity results equal to zero, meaning that the generation capacity included in the infrastructure is enough for satisfying the electricity demand at each timestep.

The strongly different operation of thermoelectric power plants with respect to 2018 is allowed by the simplified model introduced for the electricity grid, described in Chapter 4, since congestions and transportation limits are neglected and transmission losses are accounted only with an overall efficiency value. With a more detailed model, these limits could significantly influence the electricity generation mix, favouring power plants sited close to the electricity consumers.

## 5.2 Case 1 – unconstrained $H_2$

The Case 1 scenario is generated optimising the infrastructure for operating in the first weeks of June (Case 1A) and January (Case 1B), with a $CO_2$ emission reduction target of 65% with respect to the base case. The optimal configuration satisfying such constraint is characterised by a total annual cost of 3’235 M€/y for June and 3’445 M€/y for January (Figure 5.2). In both cases, fuel consumption represents the main contribution to the total infrastructure cost, contributing for more than 60% of the total cost, followed by the CCS network, accounting for around 30% of the total value, while a minor fraction is determined by the additional RES capacity installed.

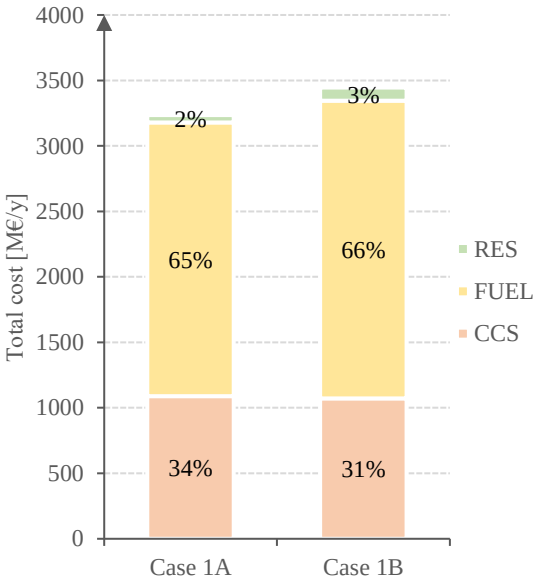


Figure 5.2. Total infrastructure cost in cases 1A and 1B, divided for the different components of the infrastructure

The optimal configuration of the CCS network captures $CO_2$ from nodes CE01, CE02, CE03, ST01, PP01, PP02 and PP04, then delivered via pipeline to the $CO_2$ storage sites CS12 and CS13, being the closest to the studied region border. The total cost of the CCS supply chain is provided for more than 80% by the capture section, followed by geological storage at 10% and the pipeline network, accounting for 6% of the total CCS cost (Figure 5.3).

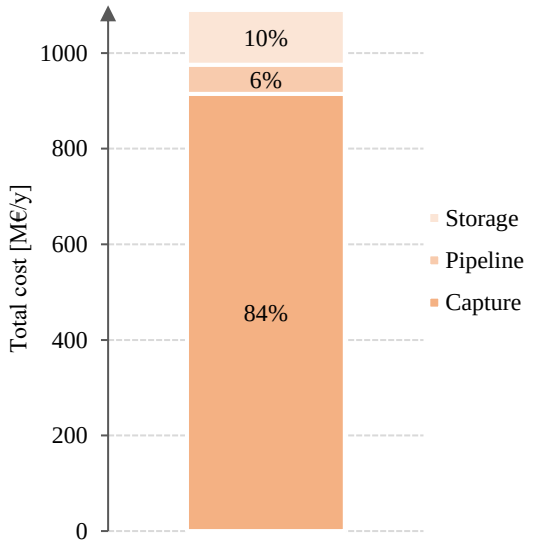


Figure 5.3. Total cost of the CCS network resulting from Case 1A, divided among capture, transportation storage.

Before discussing each component of the CCS network, it is crucial to verify whether this configuration is coherent with the mass balance constraint. The correctness in the mass balance definition is tested for a sample of timesteps and nodes (Table 5.2), for which the CO2 mass balance constraint results satisfied.

Table 5.2. $CO_2$ mass balance verification for a sample of nodes and timesteps, for which are reported the $CO_2$ captured, exchanged and stored, along with the deviation on the nodal mass balance.

| Timestep | Node | $CO_2$ captured [$t_{CO2}$/h] | $CO_2$ outlet [$t_{CO2}$/h] | $CO_2$ inlet [$t_{CO2}$/h] | $CO_2$ stored [$t_{CO2}$/h] | Difference [$t_{CO2}$/h] |
|---|---|---|---|---|---|---|
| 10 | ST01 | 1’092 | 1’383 | 291 | 0 | 0 |
| 10 | CS12 | 0 | 0 | 176 | 176 | 0 |
| 45 | CN06 | 0 | 92 | 92 | 0 | 0 |
| 100 | PP01 | 122 | 122 | | 0 | 0 |
| 130 | PN05 | 0 | 92 | 92 | 0 | 0 |
| 160 | CS13 | 0 | 0 | 1’323 | 1’323 | 0 |

The $CO_2$ emission target imposed by the optimisation algorithm forces the infrastructure to capture 303.9 $kt_{CO2}$ in one operating week, with a global CCA equal to 57 €/$t_{CO2}$. The cost required for the installation and operation of the carbon capture technologies depends on two main factors, being the partial pressure of $CO_2$ in flue gases and the size of the plant (Table 5.3). As a consequence, the nodes characterised by a high CCA consist in FR01, CH01 and PP03; being regulated with a cost-minimisation algorithm, to such nodes the CCS technology is not applied. The other node excluded from the CCS network is the coal power plant. Despite the low CCA, node PP05 contributes to a minor part of the total $CO_2$ emitted in the studied region, due to the low exploitation in the energy generation mix, therefore the infrastructure can achieve the $CO_2$ emission reduction target without mitigating this source. Among the nodes to which the $CO_2$ capture technology is applied, instead, nodes ST01 and PP04 contribute to the 84% of the total sequestered $CO_2$. Although capturing $CO_2$ from ST01 is necessary for reaching the $CO_2$ emission reduction target, PP04 results the cheapest option among the NGCC nodes, since the large size allows to exploit the scale economies, resulting a low value of CCA.

Table 5.3. $CO_2$ captured within the operating week and CCA of the industrial and thermoelectric power plant nodes in Case 1A

| Nodes | $CO_2$ captured [$kt_{CO2}$/w] | CCA [€/$t_{CO2}$] |
|---|---|---|
| CE01 | 10.52 | 59.64 |
| CE02 | 7.11 | 49.68 |
| CE03 | 8.01 | 53.44 |
| ST01 | 188.28 | 51.76 |
| FR01 | 0 | 110.80 |
| CH01 | 0 | 138.56 |
| PP01 | 20.45 | 93.57 |
| PP02 | 2.25 | 99.69 |
| PP03 | 0 | 116.77 |
| PP04 | 67.27 | 63.17 |
| PP05 | 0 | 48.38 |

The optimisation algorithm selected pipeline as the cheapest $CO_2$ transport modality, connecting capture and storage nodes exploiting onshore lines, determining a total installation cost of 61 M€. The cost required from moving one tonne of $CO_2$ results equal to 2.92 €/t, significantly higher than the value of 2 €/t reported in literature [110]. This cost difference is related to the removal of the $CO_2$ flow rate discretisation discussed in Chapter 4, preventing from exploiting the scale economy. Instead of installing large-sized pipelines, the majority of the lines are connected with a q1 pipeline, with the lowest $CO_2$ transportation capacity. Despite the high cost, pipeline transportation results economically advantageous with respect to ship transportation, that is not exploited in the optimal configuration.

The pipeline system delivers $CO_2$ to two geological storage sites, corresponding to nodes CS12, in Molise region, and CS13, sited in Basilicata. Being all the onshore sites homogenous in terms of storage cost, equal to 7.2 €/$t_{CO2}$, the infrastructure relies on the ones sited closer to the region border. Among the 303.9 $kt_{CO2}$ captured from stationary sources, 272.8 $kt_{CO2}$ are delivered to CS13, while the remaining quantity is stored in 31.1 $kt_{CO2}$. Assuming a constant operation of the infrastructure for the whole year, the $CO_2$ stored in each site is estimated being respectively 14.2 and 1.6 $Mt_{CO2}$/y: considering the minimum storage capacity estimated for the two sites by Donda et al. [37], being 344 and 16 $Mt_{CO2}$, such nodes provide enough capacity for allowing the infrastructure to operate for

10 and 24 years. The availability of $CO_2$ storage capacity, then, does not represent an operational limit for the infrastructure.

The major contribution to the total infrastructure cost is related to fuel consumption, in detail natural gas and coal. The total cost associated to this energy consumption is slightly different from the base case, respectively 2.09 M€/y and 1.97 M€/y, due to the variation in the fuel consumed by the steel industry and the natural gas-fed power plants. In detail, node ST01 is the only element with a $\rho^{CCS}$ parameter higher than 1 since the installation of the carbon capture plant determines a 20% increase in the total coal consumption. For what concerns NGCCs, a lower natural gas demand occurs due to the installation of additional RES capacity. In detail, the algorithm saturates the maximum threshold imposed for the installation of solar PV capacity, increasing the pre-existent generation capacity of 20% by installing 572 $MW_{EL}$ of solar PV panels, with a total cost of 55.4 M€/y. The choice not to install any wind turbine is determined by the low availability of the energy source in June with respect to solar energy; the opposite trend characterises the first week of January, for which the algorithm saturates the maximum capacity of wind power without increasing the solar PV capacity. For what concerns the total fuel cost, the contribution of ST01 dominates the one related to NGCCs, determining an increase of 118 M€/y with respect to the base case (Table 5.4). The total infrastructure cost increase with respect to the base case results equal to 1'263 M€/y, corresponding to a total CCA of 91.35 €/$t_{CO2}$.

Table 5.4. Total annual cost associated to the coal and natural gas consumption from industries, power plants and consumption nodes, reported for Case 1A and the base case.

| | Coal [M€/y] | | Natural gas [M€/y] | | Total cost [M€/y] | |
|---|---|---|---|---|---|---|
| Nodes | Case 1A | Base case | Case 1 A | Base case | Case 1A | Base case |
| IND | 848 | 703.6 | 125 | 125.0 | 972 | 828.6 |
| PP | 6 | 33.0 | 976 | 967.0 | 982 | 1'000.0 |
| CN | 0 | 0 | 135 | 617.4 | 135 | 617.4 |
| Total | 853 | 736.6 | 1'236 | 1'709.4 | 2'090 | 2'446.0 |

The additional RES capacity and the introduction of the CCS network strongly influence the electricity generation sector. Although the former only impacts on the total electricity output from NGCCs, the introduction of carbon capture technologies determines a redistribution of the electricity demand among the power plants (Figure 5.4). The low CCA characterising PP04 determines a net increase in the activity of the plant, with a production rate shifting from 0.41 in the base case to 0.85 in Case 1A. An inverse trend occurs for PP02 and PP03, decreasing the activity of respectively 87% and 53% with respect to the

base case. The marked reduction in the PP02 generation occurs despite the installation of the carbon capture technology, due to the lower efficiency. From an economical point of view, the solution suggests the installation of a CCS plant in PP02 instead of PP03 basing on the CCA value, for then generating more electricity from PP03, with a higher efficiency and consequently a lower fuel cost. The last NGCC, being PP01, is characterised by a low CCA and a high efficiency, therefore the infrastructure exploits its full capacity, with an average production rate of 99.7%.

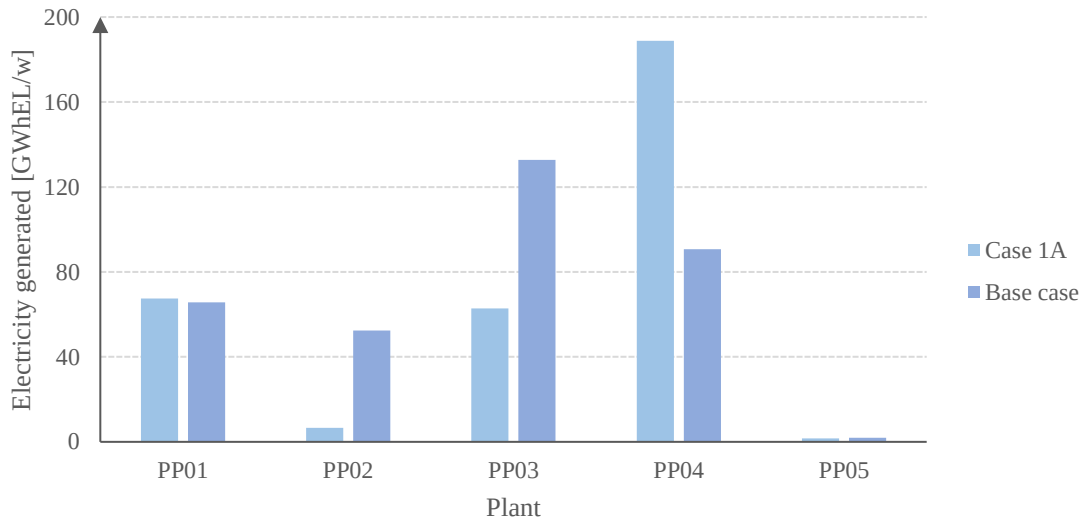


Figure 5.4. Electricity generated from each thermoelectric power plant in Case 1A and in the base case.

As stated in the previous paragraph, the solar PV availability has a strong influence on the electricity generation mix. The electricity generation profile in the studied period (Figure 5.5) highlights the difference in the energy consumption during day and night hour, with the former characterised by a high fraction of RES in the generation mix, that is strongly reduced in the night hours, in which the electricity demand is almost entirely satisfied by thermoelectric power plants. Although the generation profile is strongly non-constant for NGCCs, the contribution of coal and other fossil fuels, being own fuel consumptions in ST01, FR01 and CH01, is almost independent on the modelled timestep. The only coal power plant is exploited only in peak hours, when the NGCCs capacity is saturated, being economically convenient with respect to imported electricity.

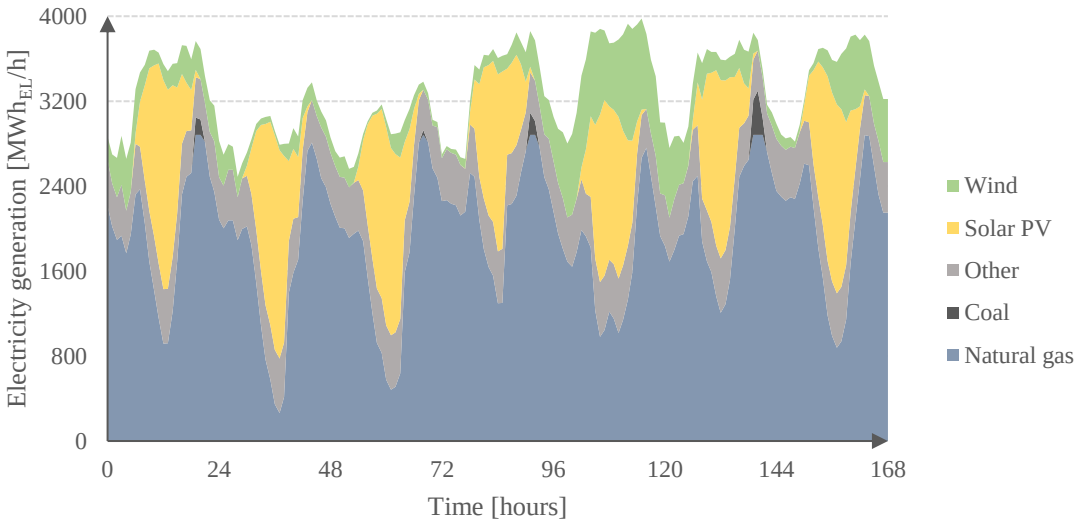


Figure 5.5. Electricity generated at each timestep in Case 1A, divided by energy source. The voice 'other' includes the contribution of the industrial nodes ST01,FR01 and CH01, exploiting own fossil fuels, like steel gases, virgin naphtha, LGP and fuel gas, as energy source.

The $CO_2$ produced in the region is characterised by a quite homogeneous distribution among the timesteps analysed (Figure 5.6). The $CO_2$ capture profile is determined by the NGCCs operation, as results from a comparison between the $CO_2$ capture fluctuations and the electricity generated in such nodes, although the variability of the profile is dampened by the almost constant activity of ST01 node, the major contributor to the $CO_2$ sequestered in the region, being characterised by an average production rate of 0.94.

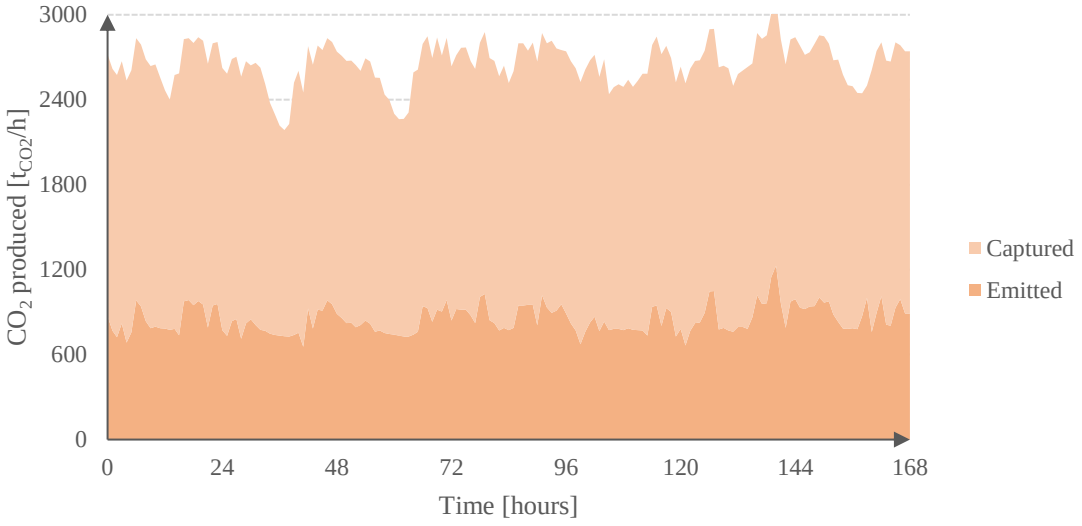


Figure 5.6. $CO_2$ captured and emitted by the infrastructure at each timestep in Case 1A

## 5.3 Case 2 – constrained $H_2$

The absence of an HSC in the optimal configuration resulting for Case 1 determined the need for developing an alternative scenario, in which the diffusion of hydrogen-based systems in the infrastructure is forced by means of the introduction of a minimum $H_2$ consumption constraint, previously defined in Eq. (5.1) and Eq. (4.48). The optimal configuration resulting from Case 2 is similar, in terms of total cost (Figure 5.7), to Case 1, with a total installation and operating cost equal to 3296 M€/y in the first week of June (Case 2A) and 3515 M€/y for January (Case 2B), slightly higher than Cases 1A and 1B (around 2%). In both cases, the main contribution to the total cost is related to the fuel consumption, providing more than half of the total value, followed by the CCS network, to which is associated a 30% share. The majority of the remaining fraction is introduced for the installation and operation of the HSC (12% for Case 2A and 8% for Case 2B), while a minor contribution is determined by the RES installation.

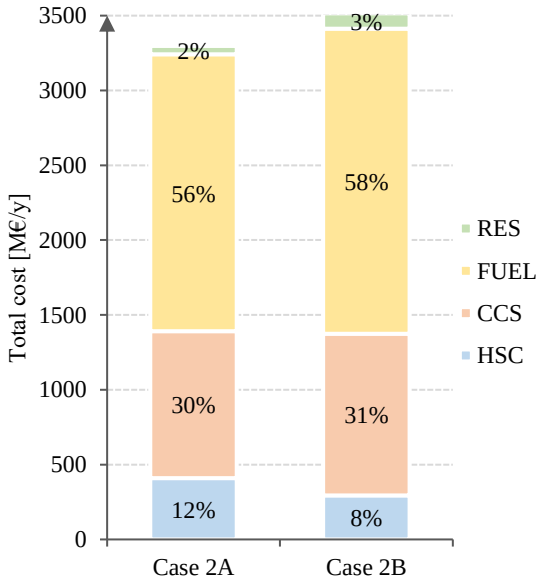


Figure 5.7. Infrastructure cost breakdown in cases 2A and 2B.

The optimal design of the HSC provides the installation of two SMRs, feeding the NGCCs corresponding to nodes PN01 and PN03. At each timestep, the $H_2$ plants only deliver hydrogen to the thermoelectric power plants, therefore no connection occurs with the consumption nodes. The hydrogen demand from small-scale industries and power plants and from residential utilities is satisfied with the installation of six electrolysers in all the production nodes, except for PN01, that in nodes PN02, PN04, PN05 and PN06 is coupled with a small-scale storage tank. The HSC is then completed with a $H_2$ pipeline network, connecting the production nodes in which green hydrogen production occurs with the correspondent consumption nodes.

The total cost required for the operation and installation of the HSC is characterised by two distinct contributions, determined by the net difference, in terms of production capacity, between SMR and electrolysers. In the optimal infrastructure configuration, the size of each plant is determined basing on the demand of the consumers, therefore the size of the electrolysers installed is two order of magnitude lower than the SMR, due to the imposition of a maximum blending limit constraint for residential utilities. As a consequence, almost the entire cost associated to the HSC is provided by the SMR, contributing to 99% of the total value, while all the other systems, being electrolysers, storage tanks and pipeline, provide a cumulated cost equal to 1% of the total HSC value.

Before deepening each component of the HSC, the mass balance conservation is verified for a sample of nodes and timesteps (Table 5.5), analogously to the $CO_2$ balance assessment conducted for Case 1A.

Table 5.5. Hydrogen mass balance verification for a sample of nodes and time steps, for which the $H_2$ produced, exchanged, consumed, and stored are reported, along with the deviation on the nodal mass balance.

| Timestep | Node | $H_2$ produced [$t_{H2}$/h] | $H_2$ exiting [$t_{H2}$/h] | $H_2$ entering [$t_{H2}$/h] | $H_2$ consumed [$t_{H2}$/h] | $H_2$ stored [$t_{H2}$/h] | Difference [$t_{H2}$/h] |
|---|---|---|---|---|---|---|---|
| 10 | PP03 | 1.04 | 0 | 0 | 1.04 | 0 | 0 |
| 10 | CN02 | 0 | 0 | 0.06 | 0.06 | 0 | 0 |
| 45 | PN07 | 0.11 | 0.11 | 0 | 0 | 0 | 0 |
| 100 | PP01 | 20.85 | 0 | 0 | 20.85 | 0 | 0 |
| 130 | PN05 | 0.06 | 0.08 | 0 | 0 | -0.02 | 0 |
| 160 | CN05 | 0 | 0 | 0.05 | 0.05 | 0 | 0 |

Blue hydrogen production occurs with the installation of two SMRs in nodes PP01 and PP03, with a nominal production capacity of, respectively, 20.85 $t_{H2}$/h and 1.04 $t_{H2}$/h. The economic optimisation algorithm led to an almost constant production from such plants, with capacity factors of respectively 99.3% and 95.7%, generating a total amount of 3.65 $kt_{H2}$/w, that extending the infrastructure operation to the whole year corresponds to an annual production of 190 $kt_{H2}$/y. Although the mathematical model provides the possibility to export $H_2$ to the HSC, both the SMRs only feed the corresponding thermoelectric power plant, since in order to deliver $H_2$ to other consumers the node should generate a null electricity output. As discussed in Chapter 4, the total cost of a SMR is determined by three contributions, being CAPEX, fixed OPEX and natural gas. Such elements determine respectively 21%, 7% and 72% of the cost associated to the SMRs installed in the infrastructure, resulting a total cost of 401 M€/y, and a cost specific to the amount of hydrogen produced equal to 2.1 €/$kg_{H2}$. Both the cost shares and the specific values result

coherent with the values reported by IEA for blue hydrogen production from natural gas [13], provided as equal to 2 €/$kg_{H2}$ for Europe.

The hydrogen demand from the consumption nodes is satisfied with a more complex system with respect to the NGCCs, with the installation of electrolysers, $H_2$ pipelines and storage tanks. As previously stated, the nominal capacity of the installed electrolysers is lower than the SMRs, with an average nominal hourly production of around 0.1 $t_{H2}$/h (Table 5.6). The total amount of green hydrogen produced by the infrastructure is equal to 63 $t_{H2}$/w, corresponding to 3.3 $kt_{H2}$/y, although this estimation has a low reliability due to the non-dispatchability of the renewable sources exploited. The high capacity factors of the electrolysers installed, higher than 70%, occurs due to the high availability of solar energy and to the small size of the hydrogen production plants. The cost specific to the hydrogen produced results equal to 0.93 €/$kg_{H2}$, strongly lower than the values reported by the International Renewable Energy Agency (IRENA), ranging from 2 to 10 €/$kg_{H2}$ [111]. The low value resulting in the proposed infrastructure is determined by the high capacity factors of the electrolysers installed and by the lack of the electricity price contribution. Taking into account these two aspects, the specific cost for green hydrogen production results coherent with the IRENA value.

Table 5.6. Nominal capacity, total cost, total production and capacity factor of the electrolysers installed in the infrastructure

| Nodes | Nominal capacity [$t_{H2}$/h] | Total cost [k€/y] | Total production [$t_{H2}$/w] | Capacity factor [%] |
|---|---|---|---|---|
| PN02 | 0.058 | 334 | 7.223 | 74.5 |
| PN03 | 0.145 | 839 | 17.291 | 71.0 |
| PN04 | 0.064 | 368 | 7.885 | 73.9 |
| PN05 | 0.095 | 552 | 11.665 | 72.7 |
| PN06 | 0.040 | 232 | 4.978 | 73.9 |
| PN07 | 0.114 | 660 | 14.161 | 73.9 |

The high capacity factor value is obtained with the installation of storage tanks with a total nominal capacity of 290 $kg_{H2}$, contributing to a minimal part of the total HSC cost (80 k€/y, equal to the 0.02% of the total value). The last component of the HSC network consists in the $H_2$ pipelines, characterised by a total cost of 5.5 M€/y and corresponding to a specific value of 1.33 €/$kg_{H2}$ for unit of $H_2$ transported. Such value, then, results coherent with the one reported by IEA, equal to 1.5 €/$kg_{H2}$ [112].

The optimal configuration of the CCS network designed in Case 2A is similar to the one described for Case 1A, with the $CO_2$ captured from nodes CE01, CE02, CE03, ST01, PP04 and PP05, then delivered via pipeline to the $CO_2$ storage sites CS12 and CS13. Consequently, the total cost of the CCS network is similar to the case previously analysed, equal to 982 M€/y, so as for the contribution of the three CCS phase to the total cost, being 82% for carbon capture from concentrated sources, 6% for transportation and 12% for the geological storage (Figure 5.8). The main difference with respect to the optimal configuration consists in the contribution of SMRs to the $CO_2$ capture from NGCC nodes, representing the connection points between CCS network and HSC.

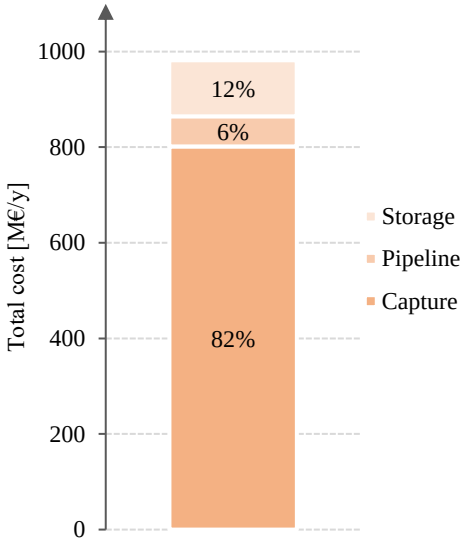


Figure 5.8 total cost of the CCS network resulting from Case 2A, divided among capture, transportation and storage.

The operation of the infrastructure during the first week of June determines the capture of 280.9 $kt_{CO2}$, lower than Case 1A, due to the hydrogen exploitation, although such value increases to 312.3 $kt_{CO2}$ per week by including the $CO_2$ captured from SMRs. Since the CCA value is not provided for hydrogen production plants, being included in the CAPEX and fixed OPEX values, the average CCA value of the CCS network is computed as the ratio between the $CO_2$ captured from industries, PP04 and PP05 and the total capture cost, resulting equal to 54.7 €/$t_{CO2}$. The reduction with respect to Case 1A is due to the lack of a capture plant installed in PP01 and PP03 node, characterised by a higher cost required for sequestering $CO_2$. The computed value, however, is not relevant for the estimation of the economic performance of the CCS network since it does not include the contribution of SMRs. With respect to Case 1A, the thermoelectric power plants are characterised by an additional degree of freedom since the $CO_2$ emission mitigation can occur with CCS or $H_2$, without the possibility to install both the technologies in a single node. The optimisation

algorithm installs a capture section on node PP04, being characterised by a lower CCA value (Table 5.7), while SMR is installed on the two power plants having the higher electrical efficiency, being PP01 and PP03 (Figure 5.9).

Table 5.7. $CO_2$ captured within the operating week and CCA of the industrial and thermoelectric power plants (excluding the SMRs contribution) in Case 2A

| Nodes | $CO_2$ captured [$kt_{CO2}/w$] | CCA [€/$t_{CO2}$] | SMR installed |
|---|---|---|---|
| CE01 | 10.52 | 59.64 | No |
| CE02 | 7.11 | 49.68 | No |
| CE03 | 8.01 | 53.44 | No |
| ST01 | 188.28 | 51.76 | No |
| FR01 | 0 | 110.80 | No |
| CH01 | 0 | 138.56 | No |
| PP01 | 0 | 93.57 | Yes |
| PP02 | 0 | 99.69 | No |
| PP03 | 0 | 116.77 | Yes |
| PP04 | 65.98 | 63.17 | No |
| PP05 | 0.97 | 48.38 | No |

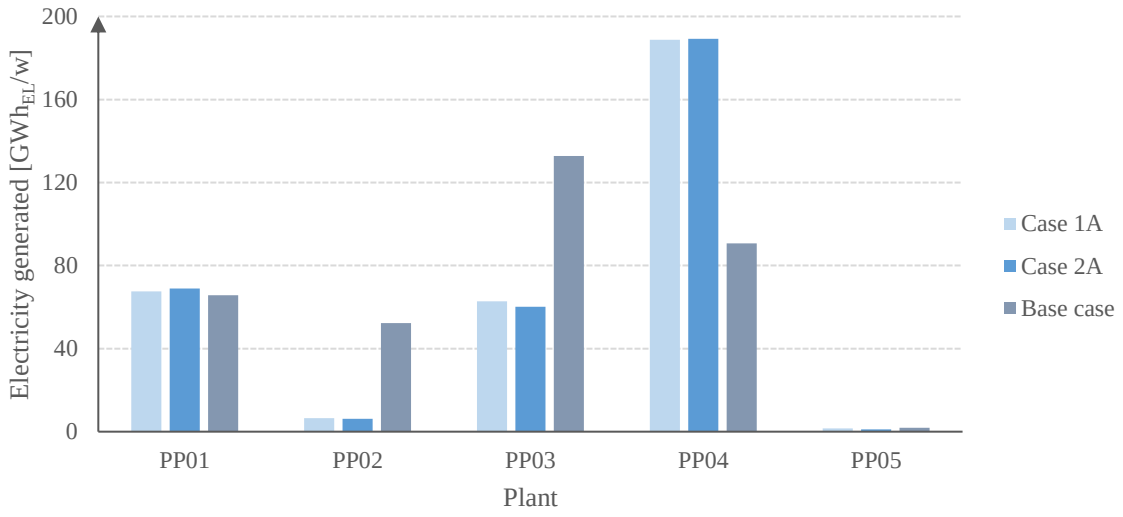


Figure 5.9. Electricity generated from each thermoelectric power plant in Case 1A and in the base case.

For what concerns the other components of the CCS network, an onshore pipeline system occurs with a total cost of 63 M€/y, corresponding to 2.73 €/$t_{CO2}$, through which $CO_2$ is transported towards the geological storage sites. $CO_2$ storage occurs in the same hubs exploited in Case 1A, with 31.2 $kt_{CO2}$/w delivered to CS12 and 282.4 $kt_{CO2}$/w to CS13. Extending the operation of the infrastructure on the whole year, the minimum capacity of such sites results enough for storing the $CO_2$ captured from stationary sources for, respectively, 10 and 23 years.

Fuel consumption provides the main contribution to the total infrastructure cost, determining an operating cost of 2.1 M€/y (Table 5.8). Differently from Case 1A, the increase in the fuel cost with respect to the base case is related both to the higher coal demand from ST01 and to the higher natural gas consumed in NGCC nodes, related to the operation of the SMR. The increase in the fuel consumption is also reflected in the total CCA computed for the whole infrastructure, resulting equal to 95.81 €/$t_{CO2}$.

Table 5.8. Total annual cost associated to the coal and natural gas consumption from industries, power plants, SMRs and consumption nodes, reported for Case 2A and the base case.

| | Coal [M€/y] | | Natural gas [M€/y] | | Total cost [M€/y] | |
|---|---|---|---|---|---|---|
| Nodes | Case 1A | Base case | Case 1 A | Base case | Case 1A | Base case |
| IND | 848 | 703.6 | 125 | 125.0 | 973 | 828.6 |
| PP | 4 | 33.0 | 747 | 967.0 | 751 | 1’000.0 |
| SMR | 0 | 0 | 291 | 0 | 291 | 617.4 |
| CN | 0 | 736.6 | 125 | 617.4 | 125 | 2’446.0 |
| Total | 851 | 703.6 | 1289 | 1’709.4 | 2140 | 828.6 |

For what concerns the electricity generation mix, the only relevant difference with respect to Case 1A consists in the hydrogen partially feeding the NGCC nodes (Figure 5.10). The hydrogen fraction in the thermal input required by the power plants varies among the nodes: for PP03, hydrogen represents the 5% of the thermal input, while PP01 operates entirely with hydrogen. Analogously to the electricity generation profile, no relevant difference occurs between the $CO_2$ production profiles in Cases 1A and 2A, since the two major contributions to the $CO_2$ captured and emitted, being ST01 and PP04, maintain an analogous behaviour in the two scenarios (Figure 5.11).

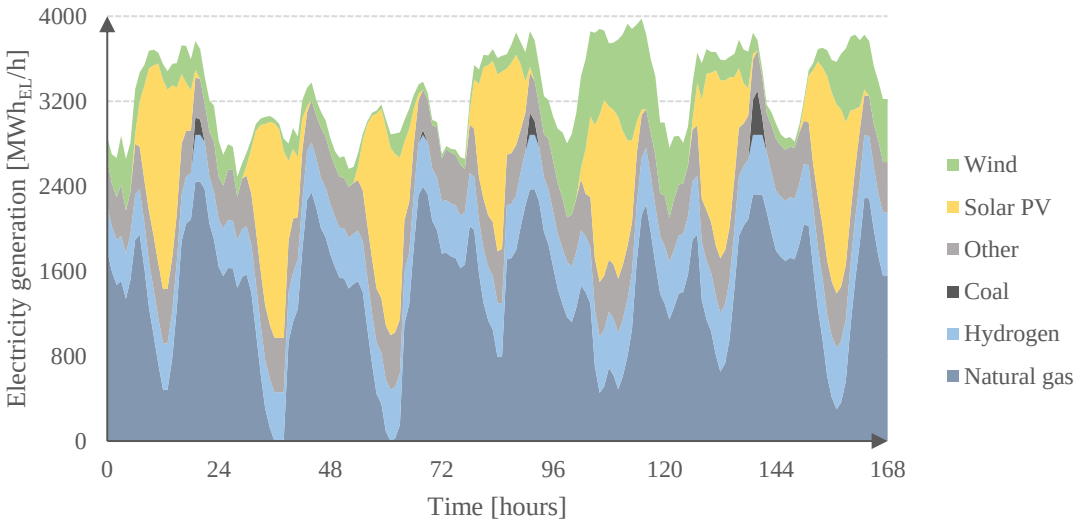


Figure 5.10. Electricity generated at each timestep in Case 2A, divided by energy source.

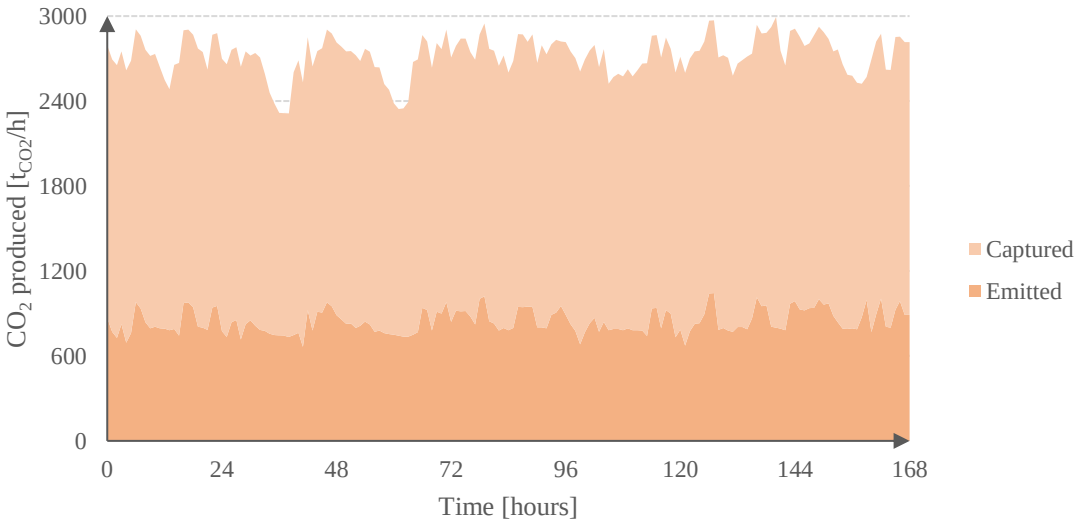


Figure 5.11. $CO_2$ captured and emitted by the infrastructure at each timestep in Case 1A

# Chapter 6
# Conclusions

This thesis discussed the design and economic optimisation of an infrastructure for integrating the installation and operation of different $CO_2$ emission mitigation strategies, being RES, HSC and CCS network. From the application of the infrastructure on a reduce one week period, results that the mathematical model is complete and coherent with the design choices introduced. Moreover, the four case studies analysed, in which two different configurations are applied to a summer and a winter operating week, allow to draw some considerations regarding the optimal design of the infrastructure. Imposing a $CO_2$ emission reduction target of 65% with respect to the base case, the infrastructure requires a total investment higher than 3.23 B€/y, most of it determined by the fuel consumption (65%), followed by the CCS network (33%) and the RES installation (2%). The optimal configuration does not include an HSC, due to the relevant investment and operating costs. The optimal design of the CCS chain captures $CO_2$ from industrial sources basing on the size and the node type, for then delivering the captured $CO_2$ to the storage sites sited close to the studied region border. $CO_2$ transportation occurs via pipeline, being it favoured with respect to ship transportation, although the removal of the flow rate discretisation prevents the model from determining the optimal size of the pipelines.

When the infrastructure is forced to include hydrogen, the optimal structure results in a total cost of 3.3 B€/y, corresponding to a 2% increase with respect to Case 1, determined by fuel consumption (56%), CCS network (30%), HSC (12%) and RES (2%). The integration of the HSC with the CCS chains occurs with the installation of SMRs integrated in the NGCC nodes, in which hydrogen is directly consumed in the combined cycle without being exported to the HSC. The hydrogen demand imposed to the consumption nodes is satisfied with the installation of a more complex system, in which small-sized electrolysers are installed in six production nodes, coupled with storage tanks with a total nominal capacity of 290 $kg_{H2}$, delivering $H_2$ to the final consumers through a $H_2$ pipeline network.

In all the modelled scenarios, coal is exploited only during peak hours, when the generation capacity from NGCCs is saturated, contributing to less than 1% of the electricity generation of the region. The fade out of coal in the electricity generation mix occurs due to the low efficiency of the thermodynamic cycle, making the only coal-based

plant economically disadvantageous with respect to the natural gas-fed power plants, despite the low CCA of the capture plant, due to the large size of the facility, and the lower price of coal with respect to natural gas.

The design of the infrastructure results similar for the two time period analysed, with the first week of January characterised by a slightly higher costs due to the higher $CO_2$ emission, mostly determined by the higher natural gas demand from residential utilities. The main difference between the infrastructure designed in the summer and winter weeks regards the RES installation. In the first week of June, the infrastructure saturates the maximum capacity constraint for solar PV installation, without increasing the pre-existent wind power generation capacity. The opposite occurs in the winter week, in which all the available capacity is installed for wind turbines, without installing any solar PV plant.

Although the model is designed for simulating the application of the infrastructure on an operating year, the high computational burden of the algorithm prevents the model from being applied on the designed time horizon. Future refinements on the proposed work must be focused on the mitigation of the high time-intensity of the convergence process. A significant reduction in the computational time may be achieved different methods, including data clustering, integer variables relaxation and the application of a two-steps algorithm. Once the convergence time is improved, the model can be enriched with additional details, for instance providing a more detailed resolution of the electricity grid and the natural gas distribution network.

# Appendix A – Results for Case 1B

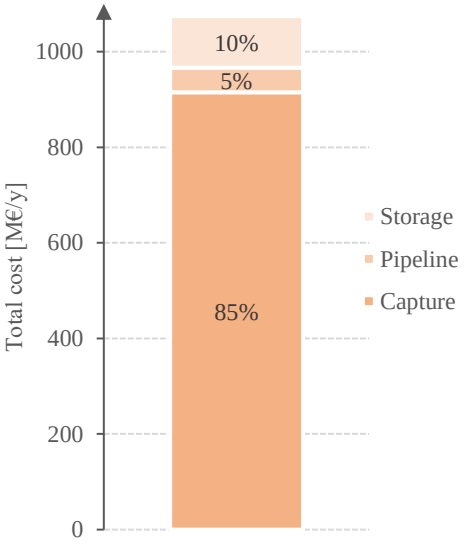


Figure A.1. Total cost of the CCS network resulting from Case 1B, divided among capture, transportation storage

Table A.1. $CO_2$ captured within the operating week and CCA of the industrial and thermoelectric power plant nodes in Case 1B

| Nodes | $CO_2$ captured [$kt_{CO2}$/w] | CCA [€/$t_{CO2}$] |
|---|---|---|
| CE01 | 2.97 | 59.64 |
| CE02 | 0.18 | 49.68 |
| CE03 | 0 | 53.44 |
| ST01 | 188.28 | 51.76 |
| FR01 | 20.53 | 110.80 |
| CH01 | 0 | 138.56 |
| PP01 | 20.32 | 93.57 |
| PP02 | 0 | 99.69 |
| PP03 | 0 | 116.77 |
| PP04 | 53.85 | 63.17 |
| PP05 | 0 | 48.38 |

Table A.2. Total annual cost associated to the coal and natural gas consumption from industries, power plants and consumption nodes, reported for Case 1B and the base case.

| | Coal [M€/y] | | Natural gas [M€/y] | | Total cost [M€/y] | |
|---|---|---|---|---|---|---|
| Nodes | Case 1A | Base case | Case 1 A | Base case | Case 1A | Base case |
| IND | 826 | 689 | 125 | 125 | 951 | 814 |
| PP | 0 | 0 | 729 | 621 | 729 | 621 |
| CN | 0 | 0 | 593 | 603 | 593 | 603 |
| Total | 826 | 689 | 1’447 | 1’349 | 2’273 | 2’038 |

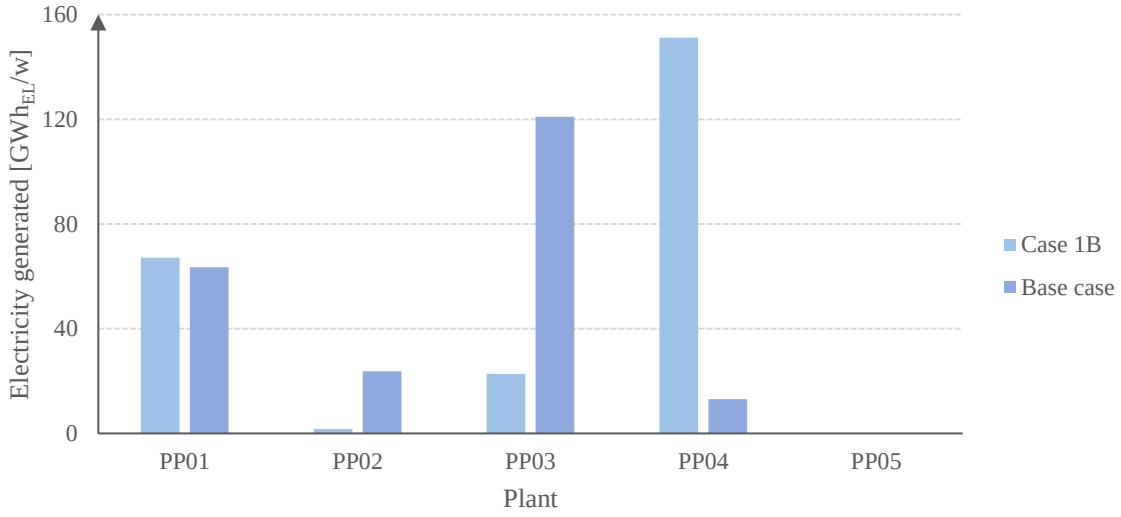


Figure A.2. Electricity generated from each thermoelectric power plant in Case 1B and in the base case.

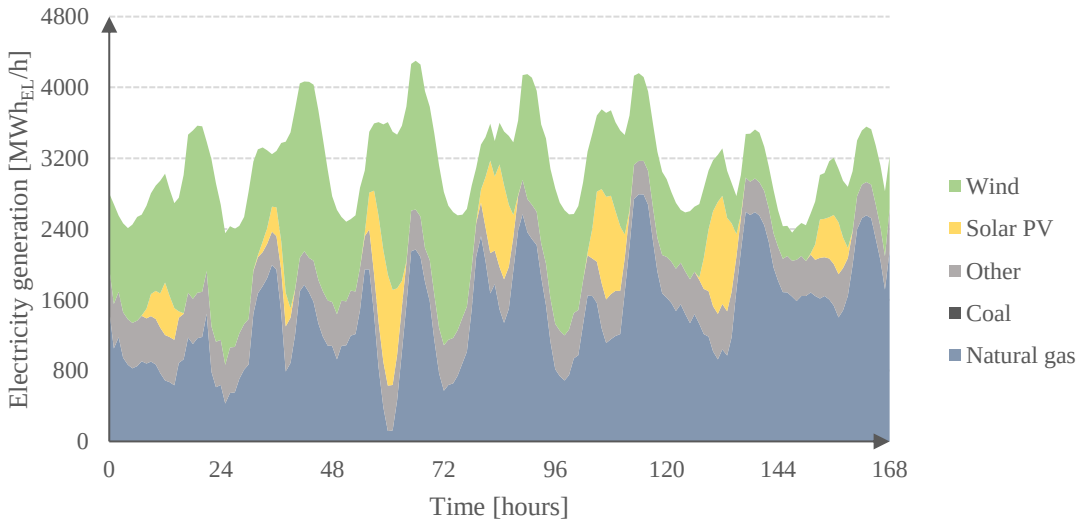


Figure A.3. Electricity generated at each timestep in Case 1B, divided by energy source.

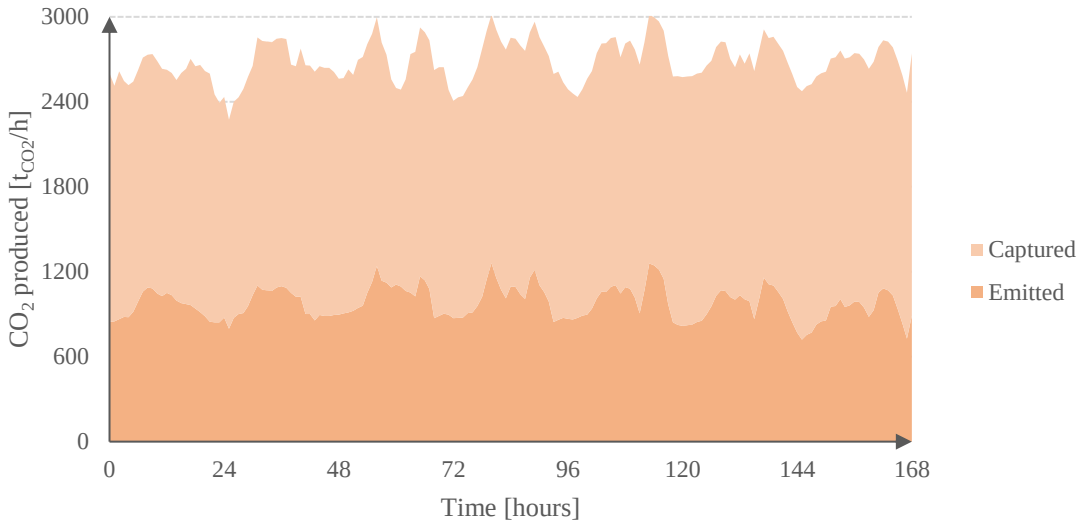


Figure A.4. $CO_2$ captured and emitted by the infrastructure at each timestep in Case 1B

# Appendix B – Results for Case 2B

Table B.1. Nominal capacity, total cost, total production and capacity factor of the electrolysers installed in the infrastructure

| Nodes | Nominal capacity [$t_{H2}$/h] | Total cost [M€/y] | Total production [$t_{H2}$/w] | Capacity factor [%] |
|---|---|---|---|---|
| PN02 | 1.02 | 5.88 | 140 | 82.0% |
| PN04 | 0.40 | 2.30 | 54 | 81.3% |
| PN05 | 0.57 | 3.28 | 76 | 80.0% |
| PN06 | 0.25 | 1.45 | 34 | 81.3% |
| PN07 | 0.57 | 3.31 | 78 | 81.3% |

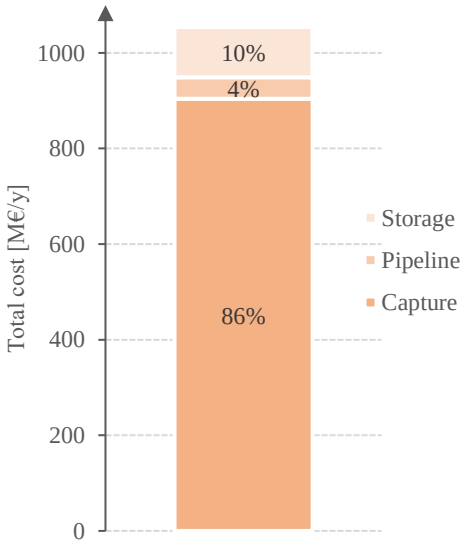


Figure B.1. total cost of the CCS network resulting from Case 2B, divided among capture, transportation and storage.

Table B.2. $CO_2$ captured within the operating week and CCA of the industrial and thermoelectric power plants (excluding the SMRs contribution) in Case 2B

| Nodes | $CO_2$ captured [$kt_{CO2}$/w] | CCA [€/$t_{CO2}$] | SMR installed |
|---|---|---|---|
| CE01 | 2.97 | 59.64 | No |
| CE02 | 0.18 | 49.68 | No |
| CE03 | 0.00 | 53.44 | No |
| ST01 | 188.28 | 51.76 | No |
| FR01 | 20.53 | 110.80 | No |
| CH01 | 0.00 | 138.56 | No |
| PP01 | 20.51 | 93.57 | No |
| PP02 | 0.00 | 99.69 | Yes |
| PP03 | 27.50 | 116.77 | No |
| PP04 | 0.00 | 63.17 | No |
| PP05 | 0.00 | 48.38 | No |

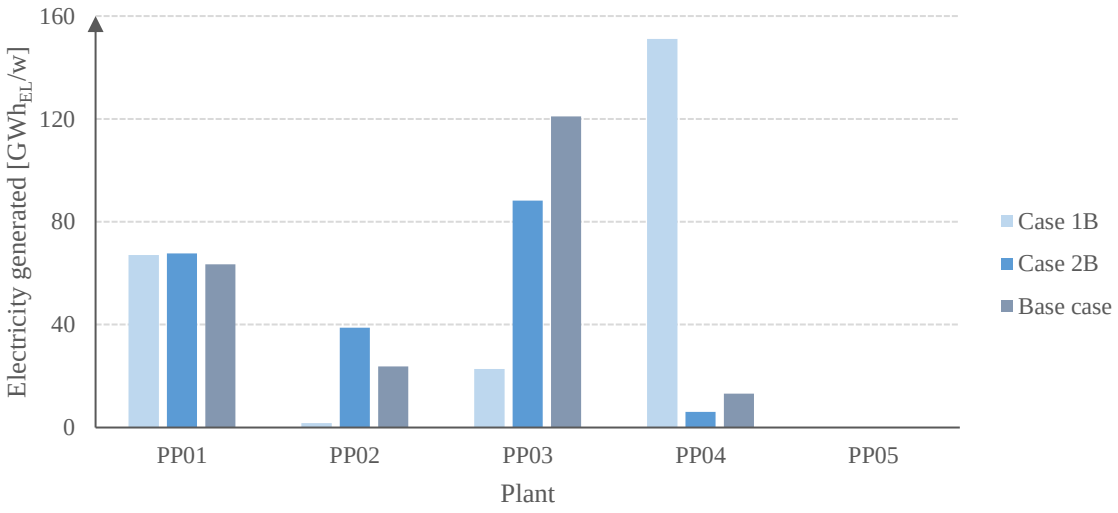


Figure B.2. Electricity generated from each thermoelectric power plant in Cases 1B and 2B and in the base case.

Table B.3. Total annual cost associated to the coal and natural gas consumption from industries, power plants, SMRs and consumption nodes, reported for Case 2B and the base case.

| | Coal [M€/y] | | Natural gas [M€/y] | | Total cost [M€/y] | |
|---|---|---|---|---|---|---|
| Nodes | Case 2B | Base case | Case 2B | Base case | Case 2B | Base case |
| IND | 826 | 689 | 147 | 125 | 973 | 814 |
| PP | 0 | 0 | 452 | 621 | 452 | 621 |
| SMR | 0 | 0 | 165 | 0 | 165 | 0 |
| CN | 0 | 0 | 583 | 603 | 583 | 603 |
| Total | 826 | 689 | 1’348 | 1’349 | 2’174 | 2’038 |

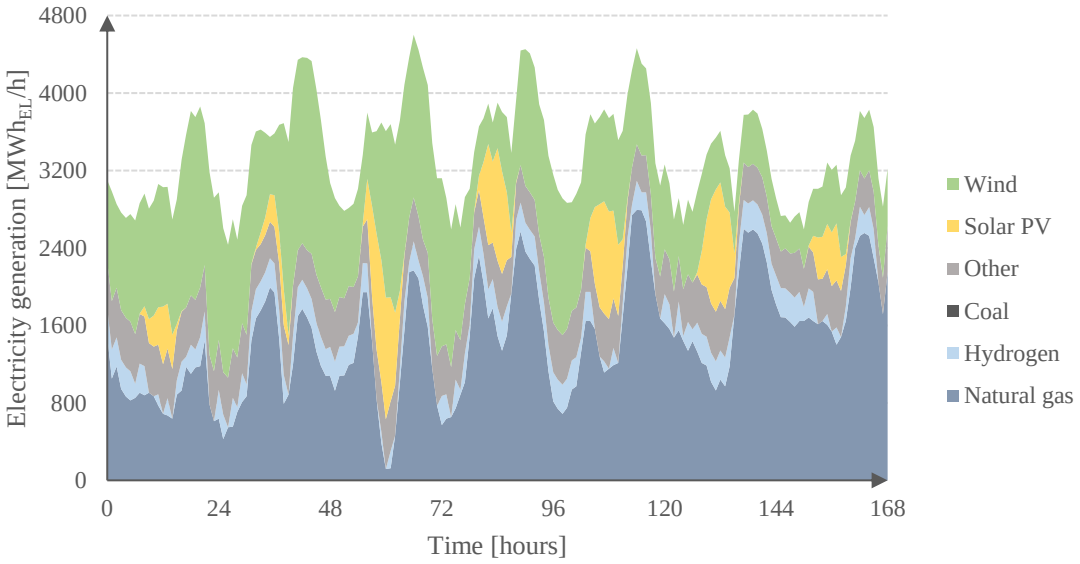


Figure B.3. Electricity generated at each timestep in Case 2B, divided by energy source.

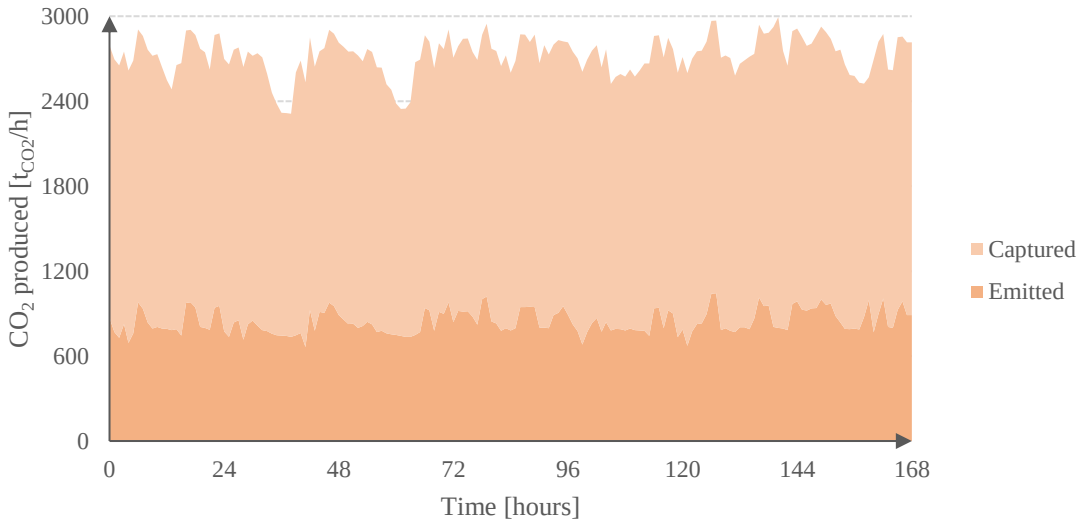


Figure B.4. $CO_2$ captured and emitted by the infrastructure at each timestep in Case 2B.

# Bibliography


[1] Intergovernmental Panel on Climate Change, “Global Warming of 1.5 ºC.” https://www.ipcc.ch/sr15/ (accessed Sep. 20, 2021).

[2] Intergovernmental Panel on Climate Change, “Sixth Assessment Report.” https://www.ipcc.ch/report/ar6/wg1/#FAQ (accessed Oct. 08, 2021).

[3] Intergovernmental Panel on Climate Change, “AR4 WGI Chapter 1: Historical Overview of Climate Change Science.” https://archive.ipcc.ch/publications_and_data/ar4/wg1/en/faq-1-3.html (accessed Oct. 08, 2021).

[4] United Nations, “The Paris Agreement,” Accessed: Sep. 20, 2021. [Online]. Available: https://www.un.org/en/climatechange/paris-agreement.

[5] European Union, “Glossary - Statistics Explained.” https://ec.europa.eu/eurostat/statistics-explained/index.php?title=Glossary (accessed Oct. 08, 2021).

[6] Intergovernmental Panel on Climate Change, “Introductory Chapter - AR5 WG3,” 2014.

[7] H. Ritchie and M. Roser, “$CO_2$ and Greenhouse Gas Emissions,” *Our World Data*, May 2020, Accessed: Oct. 08, 2021. [Online]. Available: https://ourworldindata.org/co2-and-other-greenhouse-gas-emissions.

[8] International Energy Agency, “Data overview.” https://www.iea.org/data-and-statistics (accessed Oct. 08, 2021).

[9] International Energy Agency, “Europe – Countries & Regions.” https://www.iea.org/regions/europe (accessed Sep. 28, 2021).

[10] International Energy Agency, “Italy - Countries & Regions.” https://www.iea.org/countries/italy (accessed Sep. 28, 2021).

[11] European Environment Agency, “Industrial Reporting Database v4 - March 2021.”

[12] Gestore dei Servizi Energetici, “Rapporto statistico - Fonti rinnovabili 2018,” 2019.

[13] International Energy Agency, “The Future of Hydrogen.”

[14] International Energy Agency, “Techno-Economic Evaluation of SMR Based Standalone (Merchant) Hydrogen Plant with CCS,” 2017, Accessed: Sep. 25, 2021. [Online]. Available: www.ieaghg.org.

[15] European Commission, “In focus: Hydrogen – driving the green revolution.” https://ec.europa.eu/info/news/focus-hydrogen-driving-green-revolution-2021-abr-14_en (accessed Sep. 30, 2021).

[16] C. J. Quarton and S. Samsatli, “Power-to-gas for injection into the gas grid: What can we learn from real-life projects, economic assessments and systems modelling?,” *Renew. Sustain. Energy Rev.*, vol. 98, pp. 302–316, Dec. 2018, doi:

10.1016/J.RSER.2018.09.007.

[17] Q. I. Roode-Gutzmer, D. Kaiser, and M. Bertau, “Renewable Methanol Synthesis,” *ChemBioEng Rev.*, vol. 6, no. 6, pp. 209–236, Dec. 2019, doi: 10.1002/CBEN.201900012.

[18] R. Pinsky, P. Sabharwall, J. Hartvigsen, and J. O’Brien, “Comparative review of hydrogen production technologies for nuclear hybrid energy systems,” *Prog. Nucl. Energy*, vol. 123, p. 103317, May 2020, doi: 10.1016/J.PNUCENE.2020.103317.

[19] M. Reuß, T. Grube, M. Robinius, P. Preuster, P. Wasserscheid, and D. Stolten, “Seasonal storage and alternative carriers: A flexible hydrogen supply chain model,” *Appl. Energy*, vol. 200, pp. 290–302, 2017, doi: 10.1016/j.apenergy.2017.05.050.

[20] D. Proctor, “MHPS Will Convert Dutch CCGT to Run on Hydrogen,” *Powermag*, Accessed: Sep. 30, 2021. [Online]. Available: https://www.powermag.com/mhps-will-convert-dutch-ccgt-to-run-on-hydrogen/.

[21] S. Patel, “World’s First Integrated Hydrogen Power-to-Power Demonstration Launched,” *Powermag*, Accessed: Sep. 30, 2021. [Online]. Available: https://www.powermag.com/worlds-first-integrated-hydrogen-power-to-power-demonstration-launched/.

[22] P. Agnolucci, O. Akgul, W. McDowall, and L. G. Papageorgiou, “The importance of economies of scale, transport costs and demand patterns in optimising hydrogen fuelling infrastructure: An exploration with SHIPMod (Spatial hydrogen infrastructure planning model),” *Int. J. Hydrogen Energy*, vol. 38, no. 26, pp. 11189–11201, 2013, doi: 10.1016/j.ijhydene.2013.06.071.

[23] M. Moreno-Benito, P. Agnolucci, and L. G. Papageorgiou, “Towards a sustainable hydrogen economy: Optimisation-based framework for hydrogen infrastructure development,” *Comput. Chem. Eng.*, vol. 102, pp. 110–127, 2017, doi: 10.1016/j.compchemeng.2016.08.005.

[24] N. Sunny, N. Mac Dowell, and N. Shah, “What is needed to deliver carbon-neutral heat using hydrogen and CCS?,” *Energy Environ. Sci.*, vol. 13, no. 11, pp. 4204–4224, Nov. 2020, doi: 10.1039/D0EE02016H.

[25] P. Colbertaldo, G. Guandalini, S. Campanari, and E. Crespi, “Balancing a high-renewables electric grid with hydrogen-fuelled combined cycles: A country scale analysis,” *Proc. ASME Turbo Expo*, vol. 6, pp. 1–11, 2020, doi: 10.1115/GT2020-15570.

[26] Z. Li, D. Gao, L. Chang, P. Liu, and E. N. Pistikopoulos, “Hydrogen infrastructure design and optimization: A case study of China,” *Int. J. Hydrogen Energy*, vol. 33, no. 20, pp. 5275–5286, 2008, doi: 10.1016/j.ijhydene.2008.06.076.

[27] A. Ochoa Bique, L. K. K. Maia, F. La Mantia, D. Manca, and E. Zondervan, “Balancing costs, safety and CO2 emissions in the design of hydrogen supply chains,” *Comput. Chem. Eng.*, vol. 129, 2019, doi: 10.1016/j.compchemeng.2019.06.018.

[28] P. Agnolucci and W. Mcdowall, “Designing future hydrogen infrastructure: Insights from analysis at different spatial scales,” *Int. J. Hydrogen Energy*, vol. 38, no. 13, pp. 5181–5191, 2013, doi: 10.1016/j.ijhydene.2013.02.042.

[29] L. Li, H. Manier, and M. A. Manier, “Hydrogen supply chain network design: An

optimization-oriented review," *Renew. Sustain. Energy Rev.*, vol. 103, no. June 2018, pp. 342–360, 2019, doi: 10.1016/j.rser.2018.12.060.

[30] Intergovernmental Panel on Climate Change, "CARBON DIOXIDE CAPTURE AND STORAGE."

[31] F. d'Amore, M. C. Romano, and F. Bezzo, "Carbon capture and storage from energy and industrial emission sources: A Europe-wide supply chain optimisation," *J. Clean. Prod.*, vol. 290, p. 125202, Mar. 2021, doi: 10.1016/J.JCLEPRO.2020.125202.

[32] International Energy Agency, "About CCUS – Analysis." https://www.iea.org/reports/about-ccus (accessed Oct. 03, 2021).

[33] United kingdom Business Energy & Industrial Strategy Department, "CO2 Shipping Study Final Report for BEIS Disclaimer Acknowledgements."

[34] Global CCS Institute, "Induced seismicity and CO2 geological storage." https://www.globalccsinstitute.com/news-media/insights/induced-seismicity-and-co2-geological-storage/ (accessed Oct. 03, 2021).

[35] International Energy Agency, "Energy Technology Perspectives: Special Report on Carbon Capture Utilisation and Storage CCUS in clean energy transitions," Accessed: Oct. 03, 2021. [Online]. Available: www.iea.org/t&c/.

[36] International Energy Agency, "Regional opportunities – CCUS in Clean Energy Transitions – Analysis - IEA." https://www.iea.org/reports/ccus-in-clean-energy-transitions/regional-opportunities#abstract (accessed Apr. 19, 2021).

[37] F. Donda, V. Volpi, S. Persoglia, and D. Parushev, "CO2 storage potential of deep saline aquifers: The case of Italy," *Int. J. Greenh. Gas Control*, vol. 5, no. 2, pp. 327–335, Mar. 2011, doi: 10.1016/j.ijggc.2010.08.009.

[38] International Energy Agency, "CCUS around the world – Analysis." https://www.iea.org/reports/ccus-around-the-world (accessed Oct. 03, 2021).

[39] F. d'Amore, M. C. Romano, and F. Bezzo, "Optimal design of European supply chains for carbon capture and storage from industrial emission sources including pipe and ship transport," *Int. J. Greenh. Gas Control*, vol. 109, 2021, doi: 10.1016/j.ijggc.2021.103372.

[40] Z. Nie, A. Korre, N. Elahi, and S. Durucan, "Real Options Analysis of CO2 Transport and Storage in the UK Continental Shelf under Geological and Market Uncertainties and the Viability of Subsidies for Market Development," *Energy Procedia*, vol. 114, pp. 6612–6622, Jul. 2017, doi: 10.1016/J.EGYPRO.2017.03.1815.

[41] Klokk, P. F. Schreiner, A. Pagès-Bernaus, and A. Tomasgard, "Optimizing a CO2 value chain for the Norwegian Continental Shelf," *Energy Policy*, vol. 38, no. 11, pp. 6604–6614, Nov. 2010, doi: 10.1016/J.ENPOL.2010.06.031.

[42] N. Kalyanarengan Ravi, M. Van Sint Annaland, J. C. Fransoo, J. Grievink, and E. Zondervan, "Development and implementation of supply chain optimization framework for CO2 capture and storage in the Netherlands," *Comput. Chem. Eng.*, vol. 102, pp. 40–51, Jul. 2017, doi: 10.1016/J.COMPCHEMENG.2016.08.011.

[43] W. Chen *et al.*, "CCS scenarios optimization by spatial multi-criteria analysis: Application to multiple source sink matching in Hebei province," *Int. J. Greenh.*

*Gas Control*, vol. 4, no. 2, pp. 341–350, 2010, doi: 10.1016/j.ijggc.2009.09.001.

[44] M. D. Jensen *et al.*, "Methodology for phased development of a hypothetical pipeline network for CO2 transport during carbon capture, utilization, and storage," *Energy and Fuels*, vol. 27, no. 8, pp. 4175–4182, 2013, doi: 10.1021/ef302042p.

[45] J. Morbee, J. Serpa, and E. Tzimas, "Optimised deployment of a European CO 2 transport network," *Int. J. Greenh. Gas Control*, vol. 7, no. 2012, pp. 48–61, 2012, doi: 10.1016/j.ijggc.2011.11.011.

[46] Q. Wu, Q. G. Lin, X. Z. Wang, and M. Y. Zhai, "An inexact optimization model for planning regional carbon capture, transportation and storage systems under uncertainty," *Int. J. Greenh. Gas Control*, vol. 42, pp. 615–628, 2015, doi: 10.1016/j.ijggc.2015.09.017.

[47] M. M. F. Hasan, E. L. First, F. Boukouvala, and C. A. Floudas, "A multi-scale framework for CO2 capture, utilization, and sequestration: CCUS and CCU," *Comput. Chem. Eng.*, vol. 81, pp. 2–21, Oct. 2015, doi: 10.1016/J.COMPCHEMENG.2015.04.034.

[48] Ministero dello Sviluppo Economico, "Gas_Distribuito_Regioni_2018." .

[49] Terna, "STATISTICHE REGIONALI 2018."

[50] ENEL, "Relazione Tecnica Rendimento Elettrico Centrale Termoelettrica ' Federico II ,'" 2020.

[51] ENEL, "Autorizzata dismissione anticipata del Gruppo 2 della centrale di Brindisi - corporate.enel.it." https://corporate.enel.it/it/media/press/d/2020/05/enel-autorizzata-dismissione-anticipata-del-gruppo-2-della-centrale-di-brindisi (accessed Apr. 23, 2021).

[52] ENEL, "Inaugutato a Brindisi il primo impianto pilota in Italia per la cattura della CO2," 2011. [Online]. Available: https://www.enel.com/it/media/esplora/ricerca-comunicati-stampa/press/2011/03/enel-inaugurato-a-brindisi-il-primo-impianto-pilota-in-italia-per-la-cattura-della-co2.

[53] Edison, "Progetto Puglia Green Hydrogen Valley," 2021, Accessed: Oct. 31, 2021. [Online]. Available: www.edison.it.

[54] Snam, "Verbale di misura relative al gas naturale consegnato nel mese di febbraio 2016," 2016. [Online]. Available: http://misura.snam.it/.

[55] E. Benhelal, E. Shamsaei, and M. I. Rashid, "Challenges against CO2 abatement strategies in cement industry: A review," *Journal of Environmental Sciences (China)*, vol. 104. Chinese Academy of Sciences, pp. 84–101, Jun. 01, 2021, doi: 10.1016/j.jes.2020.11.020.

[56] AITEC, "Mappa delle cementerie 2015." .

[57] Buzzi Unicem S.p.A., "Dove siamo - Buzzi Unicem Italia ." https://www.buzziunicem.it/dove-siamo (accessed Apr. 17, 2021).

[58] Buzzi Unicem S.p.A., "Emissioni forno cottura clinker." http://wt.buzziunicem.it:8000/sme-barletta/DEFAULT.HTM (accessed Apr. 17, 2021).

[59] Buzzi Unicem S.p.A., "Dichiarazione ambientale di prodotto - Premiscelati." https://www.buzziunicem.it/documents/90625/431292/Dichiarazione+ambientale+di+prodotto+-++Premiscelati.pdf/686e2f07-ccf5-16b4-0acb-18c0697c40a0 (accessed

Apr. 17, 2021).

[60] M. Voldsund *et al.*, "Comparison of technologies for CO 2 capture from cement production—Part 1: Technical evaluation," *Energies*, vol. 12, no. 3, p. 559, Feb. 2019, doi: 10.3390/en12030559.

[61] Regione Puglia, "STATISTICHE REGIONALI 2018."

[62] Italcementi, "Brochure Matera."

[63] Italcementi, "Emissioni forno." https://emissioni.itcgr.net/ecowebmatera/DEFAULT.HTM (accessed Apr. 17, 2021).

[64] Italcementi, "Report sostenibilità 2019."

[65] Colacem, "DATI GALATINA_18_19_20." .

[66] Regione Puglia, "Impianti eolici esistenti e autorizzati."

[67] International Energy Agency, "Iron and Steel Technology Roadmap Towards more sustainable steelmaking Part of the Energy Technology Perspectives series." Accessed: Jun. 09, 2021. [Online]. Available: www.iea.org/t&c/.

[68] Arcelormittal Italy Energy S.r.l., "Dichiarazione Ambientale Centrale di Taranto 2018-2020," Accessed: Apr. 17, 2021. [Online]. Available: www.italia.arcelormittal.com.

[69] Arcelormittal Italy Energy S.r.l., "Allegato C&: Nuova Relazione Tecnica dei Processi Produttivi," 2019.

[70] AGI, "Come va la produzione di acciaio in Italia, in Europa e nel mondo." .

[71] G. M. Vagliasindi, C. Gerstetter, and European Parliament. Directorate-General for Internal Policies of the Union., "The ILVA industrial site in Taranto : in-depth analysis.," p. 19, 2015.

[72] ENI power, "EniPower Stabilimento di Taranto Autorizzazione Integrata Alembientale," 2019, [Online]. Available: https://va.minambiente.it/File/Documento/262042.

[73] ENI, "Dichiarazione Ambientale della Raffineria di Taranto 2019." https://www.eni.com/assets/documents/ita/attivita/mid-downstream/Dichiarazione-Ambientale-Taranto-2019.pdf (accessed Apr. 17, 2021).

[74] Federchimica, "Stabilimento di Brindisi." https://www.federchimica.it/docs/default-source/allegati-eventi-2017/6-workshop-radar-la-collaborazione-pubblico-privata-per-la-prevenzione-e-la-gestione-delle-emergenze-nel-trasporto-chimico-in-puglia-/4-atzei.pdf?sfvrsn=847a7493_4 (accessed May 12, 2021).

[75] ENI, "Brindisi: investimenti nel settore chimico con una nuova torcia a terra." https://www.eni.com/it-IT/attivita/italia-brindisi-chimica-investimento-per-nuova-torcia-a-terra.html (accessed May 12, 2021).

[76] ENI power, "Dichiarazione ambientale."

[77] ENI Versalis, *ISTANZA DI RIESAME AIA SCHEDA " A ."* 2019.

[78] Alpiq, "Dichiarazione Ambientale 2019." https://www.alpiq.it/fileadmin/user_upload/documents/assets/san_severo/alpiq_san_severo_environmental_statement_2019_it.pdf (accessed Apr. 17, 2021).

[79] Edison, “Dichiarazione Ambientale Candela.”

[80] Sorgenia, “Dichiarazione Ambientale 2020 Centrale di Modugno.” Accessed: Apr. 17, 2021. [Online]. Available: www.sorgenia.it.

[81] ENEL, “Autorizzazione Integrata Ambientale Centrale termoelettrica ENEL di Brindisi anno 2019,” vol. 2017, 2020.

[82] Terna, “Italian National Grid | Terna Driving Energy.” https://www.terna.it/en/about-us/business/italian-national-grid (accessed Oct. 26, 2021).

[83] Terna, “L’ELETTRICITA’ NELLE REGIONI,” 2019. Accessed: Jun. 12, 2021. [Online]. Available: https://download.terna.it/terna/9-REGIONI_8d75860ff1f4b98.pdf.

[84] Gestore Mercati Energetici, “Dati di sintesi MPE-MGP.” https://www.mercatoelettrico.org/It/Statistiche/ME/DatiSintesi.aspx (accessed Aug. 07, 2021).

[85] ISTAT, “Popolazione residente al 1° gennaio.” http://dati.istat.it/Index.aspx?DataSetCode=DCIS_POPRES1 (accessed Jun. 12, 2021).

[86] Snam, “Network operational balancing data post Resolution 312/2016/R/gas.” https://www.snam.it/en/transportation/operational-data-business/8_network_operational_balancing_data/2018/index.html (accessed Aug. 07, 2021).

[87] E. L. M. Medina, “Analisi Combinata di Reti di Distribuzione Elettriche e Gas Caratterizzate da Alta Penetrazione di Risorse Distribuite,” Politecnico di Torino, 2018.

[88] Gestore dei Servizi Energetici, “Rapporto statistico - Solare fotovoltaico.”

[89] Gestore dei Servizi Energetici, “Rapporto statistico 2018 - fonti rinnovabili,” 2019.

[90] ENTSO-E, “Data view.” https://transparency.entsoe.eu (accessed Jul. 04, 2021).

[91] Istituto Nazionale di Statistica, “Confini delle unità amministrative a fini statistici al 1° gennaio 2021,” 2021. https://www.istat.it/it/archivio/222527 (accessed Nov. 27, 2021).

[92] Eurostat, “Top 20 ports.” http://appsso.eurostat.ec.europa.eu/nui (accessed Jun. 13, 2021).

[93] Regione Puglia, “Porto di Taranto.” http://mobilita.regione.puglia.it/index.php/nodi-strategici/item/3-porto-di-taranto (accessed Jun. 13, 2021).

[94] “SEA-DISTANCES.ORG - Distances.” https://sea-distances.org/ (accessed Jun. 13, 2021).

[95] European Union, “Candidate PCI projects in cross-border carbon dioxide (CO2) transport networks in view of preparing the 5 th PCI list.”

[96] Google, “Google Maps.” https://www.google.it/maps (accessed May 12, 2021).

[97] University of Colorado Denver, “Spherical Law of Cosines,” Accessed: Aug. 07, 2021. [Online]. Available: http://www.math.ucdenver.edu/~hartkes/teaching/2011m896/SphericalLawOfCosines.pdf.

[98] T. Kuramochi, A. Ramírez, W. Turkenburg, and A. Faaij, “Comparative assessment of CO2 capture technologies for carbon-intensive industrial processes,” *Prog. Energy Combust. Sci.*, vol. 38, no. 1, pp. 87–112, Feb. 2012, doi: 10.1016/J.PECS.2011.05.001.

[99] Global CCS Institute, “TECHNOLOGY READINESS AND COSTS OF CCS TECHNOLOGY ,” 2021.

[100] G. Bristowe and A. Smallbone, “The Key Techno-Economic and Manufacturing Drivers for Reducing the Cost of Power-to-Gas and a Hydrogen-Enabled Energy System,” *Hydrogen*, vol. 2, no. 3, pp. 273–300, 2021, doi: 10.3390/hydrogen2030015.

[101] W. Liu, H. Zuo, J. Wang, Q. Xue, B. Ren, and F. Yang, “The production and application of hydrogen in steel industry,” *International Journal of Hydrogen Energy*, vol. 46, no. 17. Elsevier Ltd, pp. 10548–10569, Mar. 08, 2021, doi: 10.1016/j.ijhydene.2020.12.123.

[102] European Union, “Statistics | Eurostat.” https://ec.europa.eu/eurostat/databrowser/view/nrg_pc_203/default/table?lang=en (accessed Oct. 14, 2021).

[103] T. Włodek, M. Łaciak, K. Kurowska, and Ł. Węgrzyn, “Thermodynamic analysis of hydrogen pipeline transportation – selected aspects,” *AGH Drilling, Oil, Gas*, vol. 33, no. 2, p. 379, 2016, doi: 10.7494/DRILL.2016.33.2.379.

[104] Gestore dei Servizi Energetici, “PV market, business and price developments in Italy.”

[105] Gestore dei Servizi Energetici, “Il punto sull’eolico,” 2017.

[106] US National Renewable Energy Laboratory, “Useful Life | Energy Analysis | NREL.” https://www.nrel.gov/analysis/tech-footprint.html (accessed Oct. 14, 2021).

[107] United States Environmental Protection Agency, “Simple Search | NSCEP | US EPA.” https://nepis.epa.gov/ (accessed Oct. 14, 2021).

[108] International Energy Agency, “Prices and costs – Coal 2020 – Analysis ,” 2020. https://www.iea.org/reports/coal-2020/prices-and-costs (accessed Nov. 04, 2021).

[109] G. Guandalini, S. Campanari, and M. C. Romano, “Power-to-gas plants and gas turbines for improved wind energy dispatchability: Energy and economic assessment,” *Appl. Energy*, vol. 147, pp. 117–130, Jun. 2015, doi: 10.1016/J.APENERGY.2015.02.055.

[110] Global CCS Institute, “The Costs of CO 2 Transport.”

[111] International Renewable Energy Agency, “GREEN HYDROGEN COST REDUCTION,” 2020, Accessed: Nov. 16, 2021. [Online]. Available: www.irena.org/publications.

[112] International Energy Agency, “IEA G20 Hydrogen report: Assumptions.”